

AD-A254 002



2

FINAL REPORT

**Infiltration Kinetics and Interfacial Bond Strength of
Metal Matrix Composites**

Submitted to:

Dr. Steven Fishman
Office of Naval Research
Arlington, Virginia 22217

S DTIC ELECTE D
AUG 12 1992
A

Submitted by:

Glen R. Edwards and David L. Olson
Center for Welding and Joining Research
Colorado School of Mines
Golden, Colorado 80401

This document has been approved
for public release and sale; its
distribution is unlimited.

July, 1992

92-20904



92 7 51 193



**CENTER FOR WELDING AND
JOINING RESEARCH**

Colorado School of Mines
Golden, Colorado 80401

TABLE OF CONTENTS

	<u>Page</u>
SUMMARY OF EXPERIMENTAL ACCOMPLISHMENTS	3
GRADUATE DEGREES.	5
PAPERS PUBLISHED IN REFEREED JOURNALS	5
CONFERENCE PROCEEDINGS AND TECHNICAL REPORTS	6
INVITED PRESENTATIONS	7
PRESENTATIONS	7
APPENDIX I - PAPERS AND CONFERENCE PROCEEDINGS	9

Accession For	
NTIS CRA&I	<input checked="" type="checkbox"/>
DTIC TAB	<input type="checkbox"/>
Unannounced	<input type="checkbox"/>
Justification	
By	
Distribution /	
Availability Codes	
Dist	Avail and/or Special
A-1	

DTIC QUALITY INSPECTED 1

Statement A per telecon Steven Fishman
ONR/Code 1131
Arlington, VA 22217-5000

NWW 8/11/92

SUMMARY OF EXPERIMENTAL ACCOMPLISHMENTS

The research accomplishments for this three-year metal matrix composite research program centered upon three areas: infiltration kinetics, wettability studies and predictions of interfacial properties. The major accomplishments for each year are summarized in the following section.

Year One

A pre-conditioning reaction model was hypothesized to explain the incubation period observed to precede the liquid metal infiltration of SiC particulate, and a rate equation for pre-conditioning was experimentally established for the infiltration of SiC particulate by liquid aluminum (CR11). A threshold pressure, or the minimum pressure required for infiltration after incubation, was estimated.

Experimental wettability studies were completed for Al-Si, Al-Mg, and Al-Li alloys in contact with SiC by utilizing a capillary rise apparatus (T4). The oxide layers on the ceramic substrate and on the molten metal surface were observed to strongly influence wetting behavior.

A theoretical model to predict interfacial properties such as interfacial bond strength was developed. The model incorporated measurements of optical reflectance to determine the surface properties of a solid. Calculated interfacial bond energies of pure metals Cu-Zn alloys and Al-SiC interfaces were completed (J6).

Year Two

Differential optical reflectance was used to measure the optical transitions in aluminum and its alloys, and the previously developed semi-empirical model was used to calculate surface energies. Predicted surface energies were in close agreement with experimentally determined surface energies taken from the literature.

Interfacial bond energies were estimated using a work of decohesion model (J6). Punch shear tests then provided relative estimates of bond strengths for several aluminum alloys in contact with silicon carbide. The predicted bond energy trends correlated well with observed bond strengths.

Year Three

Concepts from surface science and thermodynamics were coupled to theoretically predict wettability. Wetting was treated as a surface phenomenon, in which a surface reaction monolayer was sufficient to cause wetting (J5). According to this model, the spontaneity of wetting is governed by ΔG_w , a thermodynamic term defined as the free energy of wetting. Theoretical predictions compared favorably with experimental wettability measurements made using a capillary rise apparatus. The model was further validated for silicon dioxide surfaces (CR14).

Compacts of silicon carbide prepared by a vibration technique were found to have reproducible gas permeabilities. The infiltration of these compacts was then studied as a function of temperature and pressure (T3). The progress of the infiltration front was monitored on line by observing the changes in the pressure drop.

A phenomenological equation relating the infiltration rate to the applied pressure, threshold pressure, height of the compact, activation energy for viscous flow of aluminum, and the absolute temperature was determined. Aluminum powder additions to the compact prior to infiltration were found to alleviate porosity and provide a method for varying the volume fraction of reinforcement.

Aluminum matrix composite processing using the liquid metal route is complicated by the oxide barrier formed on the liquid metal. A transport model was used to explain the observed interfacial reaction behavior (CR15).

GRADUATE DEGREES

A. COMPLETED

- T1. P.B. Maxwell, M.S., "The Infiltration Behavior of Aluminum into Silicon Carbide Compacts", CSM Thesis No. T-3396, 1987.
- T2. J.D. Seitz, M.S., "The Infiltration Kinetics of Silicon Carbide Reinforced Aluminum Matrix Composites", CSM Thesis No. T-3613, 1988.
- T3. P.Q. Campbell, M.S., "On the Behavior of Infiltrating Aluminum into Compacts Comprised of Silicon Carbide and Aluminum Powder Mixed with Silicon Carbide", CSM Thesis No. T-3957, 1990.
- T4. B. Lanning, Ph.D., "A Method for Predicting Wettability and Interfacial Bond Strengths at Metal/Ceramic Interfaces", CSM Thesis No. T-3875, 1990.

B. IN PROGRESS

- T5. Pr. Chidambaram, Ph.D., "Thermodynamic and Kinetic Aspects of Reactive Metal Liquids in Contact with Oxide Ceramics", 1992.

PAPERS PUBLISHED IN REFEREED JOURNALS

- J1. G.P. Martins, D.L. Olson, and G.R. Edwards, "Modeling of Infiltration Kinetics for Liquid Metal Processing of Composites", *Met. Trans. B*, vol. 29B, pp. 95-111 (1988).
- J2. P.B. Maxwell, G.P. Martins, D.L. Olson, and G.R. Edwards, "The Infiltration of Aluminum into Silicon Carbide Compacts", *Met. Trans.*, 21B, pp. 475-485 (1990).
- J3. S. Liu, D.L. Olson, G.P. Martins, and G.R. Edwards, "Modeling of Brazing Processes that Use Coatings and Interlayers", *Welding Journal*, vol. 70, no. 8, pp. 207s-215s (1991).
- J4. P.R. Chidambaram, G.R. Edwards, and D.L. Olson, "A Thermodynamic Criterion to Predict Wettability at Metal-Alumina Interfaces", *Met. Trans.*, 23B, pp. 215-222 (1992).
- J5. P.R. Chidambaram, G.R. Edwards, and D.L. Olson, "Fundamental Issues Concerning the Microdesigning of Metal-Ceramic Interfaces", *Conf. Proceedings, Fourth International Conf. on Composite Interfaces (ICCI-IV)*, and Composite Interfaces, Cleveland, OH (1992).
- J6. B.R. Lanning, T. Furtak, and G.R. Edwards, "Determination of Interfacial Bond Energies Using Modulation Reflectometry", submitted for publication in *Journal of Materials Science*.

CONFERENCE PROCEEDINGS AND TECHNICAL REPORTS

- CR1. G.P. Martins, D.L. Olson, G.R. Edwards, and P.B. Maxwell, "A Flow-in-Porous Media Model for Describing Infiltration Kinetics", Proceedings of Ninth Annual Discontinuously Reinforced Group Meeting (1987), and CSM Report MT-CWR-087-027 (July 20, 1987).
- CR2. G.R. Edwards and D.L. Olson, "Investigation into the Infiltration Kinetics and Interfacial Bond Strength of Al-SiC Composites", CSM Report MT-CWR-088-022, Annual Report, July, 1988.
- CR3. B.R. Lanning, P.Q. Campbell, J.D. Seitz, G.R. Edwards, and D.L. Olson, "Infiltration Kinetics of Al-Si Composites", Proceedings, Tenth Annual Discontinuously Reinforced MMC Working Group Meeting (1988), and CSM Report MT-CWR-088-009 (April, 1988).
- CR4. G.R. Edwards, D.L. Olson, G.P. Martins, J.D. Seitz, and P.Q. Campbell, "Infiltration Kinetics and Interfacial Bond Characteristics of Aluminum-Matrix-Silicon Carbide Composites", Proceedings of Woods Hole SDIO/IST Composites Consortium Review, Woods Hole, Mass., CSM Report MT-CWR-088-012, June, 1988.
- CR5. B.R. Lanning, T. Furtak, and G.R. Edwards, "Determination of Interfacial Bond Energies Using Modulation Reflectometry", Proceedings, Advanced Materials Conference, Denver, March 6-9, 1989, CATI-MRS.
- CR6. G.R. Edwards and D.L. Olson, "Investigations into the Infiltration Kinetics, Wettability, and Interfacial Bond Strength of Al/SiC Composites", Colorado School of Mines Report MT-CWR-089-038, Annual Report, July 1989.
- CR7. B.R. Lanning, G.R. Edwards, and D.L. Olson, "A Semi-Empirical Model for Predicting Properties of the Al/SiC Interface", Proceedings, Eleventh Annual Discontinuously Reinforced MMC Working Group Meeting, Park City, UT, MMCIAC No. 716, pp. 441-458, 1989.
- CR8. J.D. Seitz, P.Q. Campbell, G.R. Edwards, and G.P. Martins, "Infiltration Characteristics of Aluminum-Silicon Carbide Composites", Proceedings, Eleventh Annual Discontinuously Reinforced MMC Working Group Meeting, Park City, UT, MMCAC No. 716, pp. 459-488 (1989).
- CR9. B.R. Lanning, G.R. Edwards, and D.L. Olson, "Interfacial Bond Energies in Metal Matrix Composites", Proceedings of Woods Hole SDIO/IST Composites Consortium Review, Woods Hole, Mass., June, 1989.
- CR10. J.D. Seitz, P.Q. Campbell, G.R. Edwards, and G.P. Martins, "Infiltration Kinetics of SiC-Reinforced Aluminum Matrix Composites", Proceedings of Woods Hole SDIO/IST Composites Consortium Review, Woods Hole, Mass., June 1989.

- CR11. J.D. Seitz, G.R. Edwards, and G.P. Martins, "Infiltration Mechanisms and Kinetics of Liquid Aluminum Infiltration", Conference Proceedings, Interfacial Reactions in Composites Symposium, AIME, Anaheim, CA, February 1990.
- CR12. G.R. Edwards and D.L. Olson, "Fundamental Concepts of Wettability and Interfacial Bond Strength in Aluminum Matrix, SiC-Reinforced Composites", CSM Report No. MT-CWR-090-012, Annual Report, 1990.
- CR13. G.R. Edwards and D.L. Olson, "Wettability and Interfacial Kinetics in Metal Matrix Composites", CSM Report No. MT-CWR-091-015, Annual Report, 1991.
- CR14. P.R. Chidambaram, G.R. Edwards, and D.L. Olson, "Fundamental Aspects of Metal-Quartz Joining", Proc. Int. Symp. on "Joining of Materials for 2000 A.D.", pp. 331-338, December 12-14, 1991, Tiruchirapilli, India, Indian Institute of Welding (1991).
- CR15. P.R. Chidambaram, G.R. Edwards, and D.L. Olson, "Wetting of Ceramic by Molten Metals: Rate Controlling Phenomena", Proc. AIME-TMS Symp. on The Metal Science of Joining, pp. 67-71, TMS-AIME, October 20-24, Cincinnati, OH (1991), Warrendale, PA (1992).

INVITED PRESENTATIONS

- IP1. B.R. Lanning and G.R. Edwards, "Optical Reflectance Techniques and the Wettability and Bond Strength of Metal Matrix Composites", MST Materials Science Symposium, Los Alamos National Laboratory, November 30, 1989.
- IP2. P.R. Chidambaram, G.R. Edwards, and D.L. Olson, "Wetting of Ceramic by Molten Metal: Rate Controlling Phenomena", The Metal Science of Joining Symposium, TMS Fall Meeting, Cincinnati, OH, October 1991.
- IP3. P.R. Chidambaram, G.R. Edwards, and D.L. Olson, "Fundamental Issues Concerning the Microdesigning of Metal-Ceramic Interfaces, Fourth International Conference on Composite Interfaces (ICCI-IV), and Composite Interfaces, Cleveland, OH, May 26-29, 1992.

PRESENTATIONS

- P1. B.R. Lanning, P.Q. Campbell, J.D. Seitz, G.R. Edwards, and D.L. Olson, "Infiltration Kinetics of Al-SiC Composites", Part City, Tenth Annual Discontinuously Reinforced Aluminum Working Group Review Meeting (1988), January, 1988.
- P2. G.R. Edwards, D.L. Olson, G.P. Martins, B.R. Lanning, J.D. Seitz, and P.Q. Campbell, "Infiltration Kinetics and Interfacial Bond Characteristics of Aluminum Matrix-Silicon Carbide Composites", Woods Hole, SDIO/IST Conference, Woods Hole, Mass., June 1988.

- P3. B.R. Lanning, G.R. Edwards, and D.L. Olson, "A Semi-Empirical Model for Predicting Properties of the Al/SiC Interface", Park City, Eleventh Annual Discontinuously Reinforced MMC Working Group Meeting, February, 1989.
- P4. J.D. Seitz, P.Q. Campbell, G.R. Edwards, and G.P. Martins, "Infiltration Characteristics of Aluminum-Silicon-Carbide Composites", Park City, Eleventh Annual Discontinuously Reinforced MMC Working Group Meeting, February, 1989.
- P5. B.R. Lanning, G.R. Edwards, and D.L. Olson, "Interfacial Bond Energies in Metal Matrix Composites", Woods Hole, IST-SDIO/ONR Woods Hole IV Research on Advanced Materials Review, Woods Hole, Mass., June 1989.
- P6. J.D. Seitz, P.Q. Campbell, G.R. Edwards, and G.P. Martins, "Infiltration Characteristics of Aluminum-Silicon Carbide Composites", Woods Hole, IST-SDIO/ONR Woods Hole IV Research on Advanced Materials Review, Woods Hole, Mass., June 1989.
- P7. P.R. Chidambaram, B.R. Lanning, and G.R. Edwards, "Fundamental Approach to Metal-Ceramic Brazing", 71st Annual AWS Convention, Anaheim, CA, April 23, 1990.
- P8. B.R. Lanning, G.R. Edwards, and D.L. Olson, "The Use of Optical Reflectance Technique to Predict Surface Free Energy, Wettability, and Interfacial Bond Strength, Woods Hole, MA, IST-SDIO/ONR Woods Hole V Research on Advanced Materials Review, Woods Hole, MA, June 1990.
- P9. D.L. Olson, G.R. Edwards, and B.R. Lanning, "Optical Reflectance Technique to Predict Surface Free Energy, Wettability, and Interfacial Bond Strength", AFOSR/ONR Cornell Workshop, September 10-11, 1990.
- P10. G.R. Edwards and D.L. Olson, "Wettability and Infiltration Kinetics in Metal Matrix Composites", Woods Hole, MA, IST/SDIO/ONR Woods Hole Research on Advanced Materials Review, Woods Hole, MA, June 1991.
- P11. G.R. Edwards, P.R. Chidambaram, and D.L. Olson, "Wettability in Metal-Ceramic Systems", DOE Basic Energy Sciences Welding Science Workshop, Golden, Colorado, October 1991.
- P12. P.R. Chidambaram and G.R. Edwards, "A Systematic Approach to Metal-Ceramic Brazing, 72nd Annual AWS Convention, Detroit, Michigan, pp. 221, 1991.
- P13. P.R. Chidambaram and G.R. Edwards, "Kinetics Involved in Metal-Ceramic Brazing, 73rd Annual AWS Convention, Chicago, Illinois, pp. 223-225, 1992.

APPENDIX I
PAPERS AND CONFERENCE PROCEEDINGS

The Infiltration of Aluminum into Silicon Carbide Compacts

P.B. MAXWELL, G.P. MARTINS, D.L. OLSON, and G.R. EDWARDS

Although liquid-metal processing of metal matrix composites offers economic advantages, problems related to the nonwetting nature of the ceramic discontinuous reinforcement create obstacles to its ready implementation. Infiltration can occur only if a threshold pressure is applied to overcome the unfavorable interfacial forces in the system. The research reported in this paper has been devoted primarily to experiments on infiltrating silicon carbide compacts with pure aluminum, aluminum-1 wt pct magnesium, and aluminum-1 wt pct silicon. The major finding has been that an incubation time is necessary before infiltration can proceed, even though the threshold pressure is exceeded. Thus, while the model equations available for predicting the infiltration rate of compacts appear to be adequate, the incubation time can represent the rate-determining step in the process. It is suggested that the mechanism responsible for the incubation phenomenon may be related to a surface modification produced by either reaction of liquid aluminum with an oxide film on the surface of the particles or coverage of the surface by a capillarity-induced aluminum condensate.

I. INTRODUCTION

DISCONTINUOUSLY reinforced metal matrix composites have been fabricated by various techniques of which the most successful have been the solid-state processes. These include powder metallurgy processing and lamination of reinforcement and metal by diffusion bonding.^[1] Liquid-metal processes have had less success, although liquid processing of particulate-reinforced composites is potentially more economical. Moderate success has been experienced with both the addition of the ceramics to the liquid metal prior to casting and the direct infiltration of ceramic preforms.^[2] A primary obstacle to the liquid-metal techniques is the nonwetting nature of the ceramics. Flocculation of the ceramic occurs when mixed into the melt prior to casting,^[3] voids form at interfaces, and incomplete infiltration results. Degradation of the silicon carbide by reaction with aluminum is also a concern,^[4] and various techniques have been employed to overcome these problems.^[5]

Liquid-metal processes which have had limited success include compositing and infiltration.^[1] In compositing,^[6] silicon carbide powder is stirred into the melt at a temperature between that of the liquidus and the solidus. Since this partially solidified melt behaves as a slurry, the silicon carbide powder can then be mechanically entrapped, allowing the mixture to be cast into a metal matrix composite. Composites produced by this process have been characterized by voids and often by poor bonding at the ceramic/metal interfaces.

Vacuum coating and pressure (squeeze) casting^[7] have been applied to the liquid-metal infiltration of silicon carbide fibers. Liquid-metal infiltration processes offer a considerable advantage in the production of intricately

shaped parts such as tubes, where the full benefits of continuous fibers may be realized.

The advantage of producing silicon carbide/aluminum matrix composites by liquid-metal infiltration techniques cannot be fully realized without improvements in the infiltration behavior and fiber matrix bonding.^[8] Previous investigations have focused on the effects of processing parameters such as pressure, temperature, and alloying.^[9,10] This paper reports on an infiltration model which considers the physical properties of the liquid and preform. These properties include viscosity, density, surface tension, wettability, and pore size. The model has been assessed in terms of its ability to predict infiltration behavior from known physical properties of the material utilized in controlled laboratory experiments. Infiltration problems can be solved by modification of the properties of the liquid-metal and/or ceramic reinforcements.

A. Wettability

An understanding of the infiltration thermodynamics provides information on whether infiltration will occur spontaneously for a given system or whether external work must be performed upon the system. Wettability is commonly used to assess the interfacial tension driving forces and is measured in terms of the liquid-solid contact angle, θ . Values of θ less than 90 deg indicate a propensity for wetting, whereas nonwettability is defined by values of θ greater than 90 deg.

There is a lack of consistency in the experimentally determined contact angles for the silicon carbide/aluminum system.^[11,12] The measurement is complicated by the nature of the silicon carbide/aluminum interface. Since both materials generally have an oxide layer, some investigators may actually have reported equilibrium contact angles for aluminum in contact with an oxide. While it is believed that the oxide layer associated with the silicon carbide may be reduced by chemical reaction with aluminum, depending on the temperature and time of contact,^[5] this process may also be accompanied by the formation of aluminum carbide at the interface.

P.B. MAXWELL, Regional Metallurgist, is with the Carpenter Steel Division, Carpenter Technology Corporation, Los Angeles, CA 90058-0880. G.P. MARTINS, Professor, D.L. OLSON, Professor, and G.R. EDWARDS, Professor and Director, are with the Center for Welding and Joining Research, Department of Metallurgical and Materials Engineering, Colorado School of Mines, Golden, CO 80401.

Manuscript submitted October 31, 1988.

Measurements of the contact angle for this system are therefore very sensitive to material preparation, time, temperature, and atmosphere.

Kohler⁽¹³⁾ reports contact angles for several aluminum alloys in contact with silicon carbide, as shown in Figure 1. These data indicate that a transition from non-wetting to wetting of silicon carbide by aluminum alloys occurs between 900 °C (1173 K) and 1000 °C (1273 K). This transition may be the result of either the breakdown of a passive oxide film or the formation of aluminum carbide or the sequential occurrence of both. Alloying additions apparently do not affect the degree of wetting outside the transition temperature range but do alter the temperature range over which the transition occurs.

Shaler⁽¹⁴⁾ defined an infiltration indice, I_{ob} , for the tendency of liquid metal to form a mutual plane interface with the idealized porous substrate:

$$I_{ob} = \pi r^2 \gamma_{lv} [(1/\phi - 1) (\cos \theta + 1)] \quad [1]$$

where the porosity, ϕ , is the volume fraction of the material occupied by the pores and γ_{lv} is the liquid-vapor interfacial tension. The resulting index of contacting, I_{ob} , is positive for all values of ϕ , θ , r , and γ_{lv} . This tendency for the liquid metal to form a mutual interface with the substrate is illustrated in Figure 2 as a function of contact angle, θ , and pore volume fraction, ϕ . It can be concluded that the tendency for the liquid to adhere

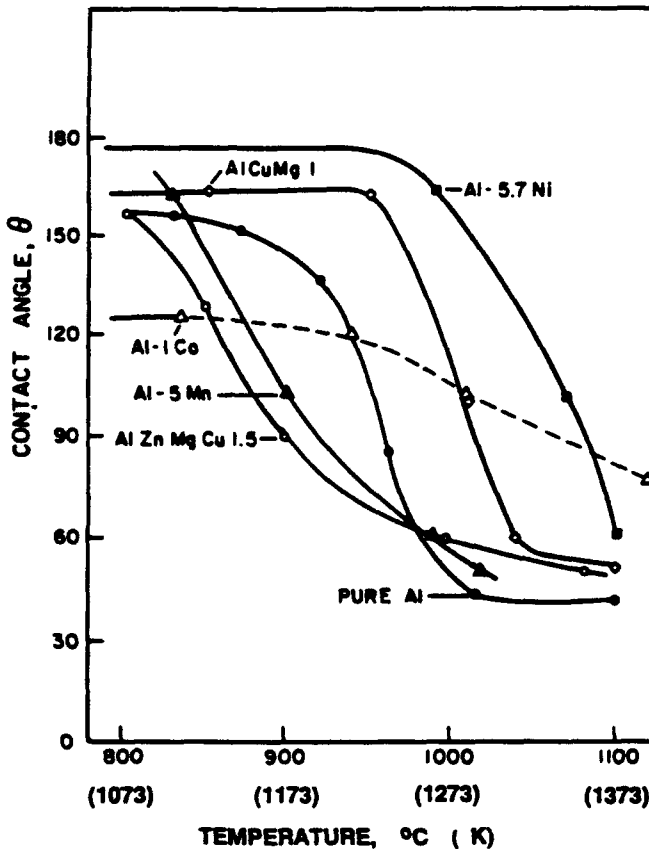


Fig. 1—Variation of the contact angle between aluminum and silicon carbide as a function of temperature and alloy composition.⁽¹³⁾ AlCuMg 1 = 3.5 to 4.5 pct Cu, 0.4 to 1 pct Mg, and 0.3 to 1 pct Mn; AlZnMgCu 1.5 = 5.1 to 6.1 pct Zn, 2.1 to 2.9 pct Mg, 1.2 to 2.0 pct Cu, 0.18 to 0.3 pct Cr, and 0 to 0.3 pct Mn.

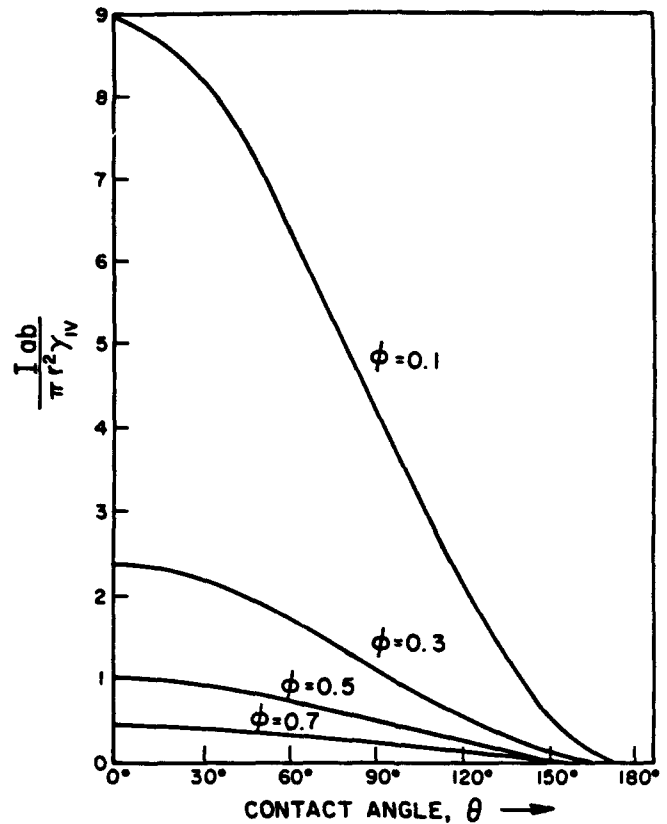


Fig. 2—Tendency for a liquid layer to adhere to a porous surface.⁽¹⁴⁾

to the surface increases with decreasing contact angle and porosity.

B. Infiltration Kinetics

The kinetics of infiltration can be described by equating the rate of change of momentum of the liquid within the capillary network to the forces which act on this liquid.^(15,16) For a wetting system, the force due to surface tension, F_{σ} , acts to move the liquid up the capillary, while this motion is resisted by the forces due to gravity, F_g , viscous drag, F_{μ} , and end drag, F_z . These forces are presented schematically in Figure 3. When these forces are equated to the rate of change of momentum of the liquid, the following equation is obtained. For a capillary tube of uniform circular cross section,

$$\pi r^2 \rho \frac{d}{dt} \left(h_c \frac{dh_c}{dt} \right) = 2\pi r \gamma_{lv} \cos \theta - \pi r^2 \rho g h_c - 8\pi \mu h_c \left(\frac{dh_c}{dt} \right) - \frac{1}{4} \pi r^2 \rho \left(\frac{dh_c}{dt} \right)^2 \quad [2]$$

where h_c is the distance infiltrated at time t , r is the capillary radius, ρ is the density of the liquid, μ is the viscosity of the liquid, and g is the acceleration due to gravity.

A similar force balance was utilized by Smlak and Rhines⁽¹⁷⁾ for describing the infiltration behavior of porous metal bodies. In their analysis, the porous body is replaced by a bundle of tubes with an "effective radius"

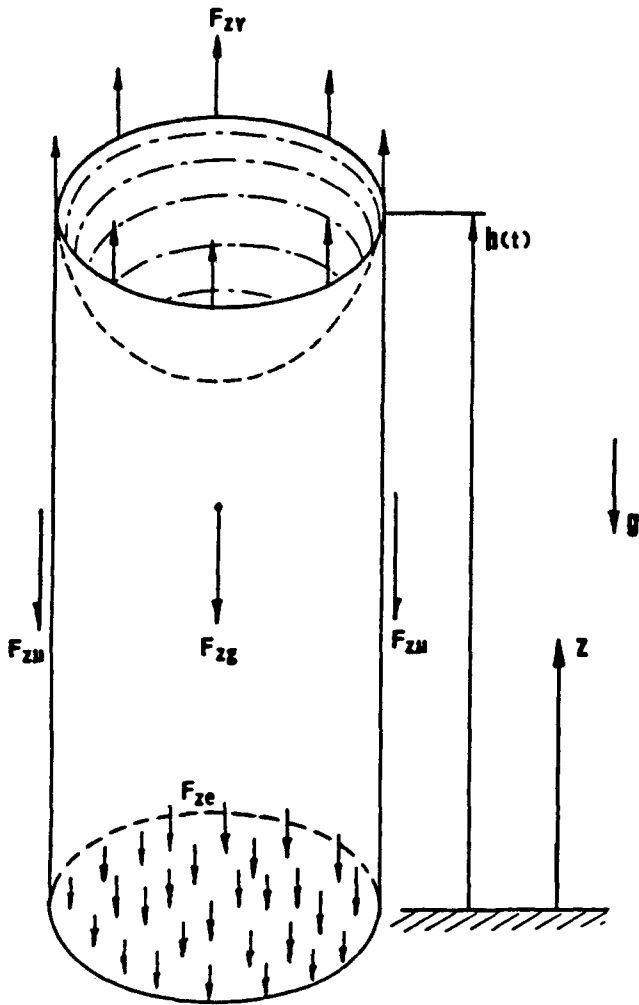


Fig. 3—Schematic showing the forces acting on a liquid column within a capillary.

which can then be determined experimentally. More recently, this model has been reexamined by Martins *et al.*^[18] and dimensionless parameters which delineate the limiting behavior have been developed and quantified.

For the work reported in this paper, the analysis of Martins *et al.*^[18] was adapted to treat the nonwetting system studied and is described in detail in the Appendix. Since pressure must be applied to induce infiltration in such a system, it was found convenient to measure the rate at which the liquid aluminum flows downward through a silicon carbide powder compact. A simpler experimental arrangement is required compared to that for inducing upward flow. A schematic describing this system is presented in Figure 4. The quantity h_{RO} is the initial height of the liquid in the reservoir, h_C is the distance the liquid has infiltrated at time t , A_C is the cross-sectional area of the compact, r_h is the effective pore radius (hydraulic mean radius), d_p is the particle diameter, and ϕ is the void fraction.

It has been shown^[18,19] that

$$\Delta P_{\text{eff}} = \Delta P^* + \frac{2\gamma_n \cos \theta}{r_h} + \rho g h_{RO} > 0 \quad [3]$$

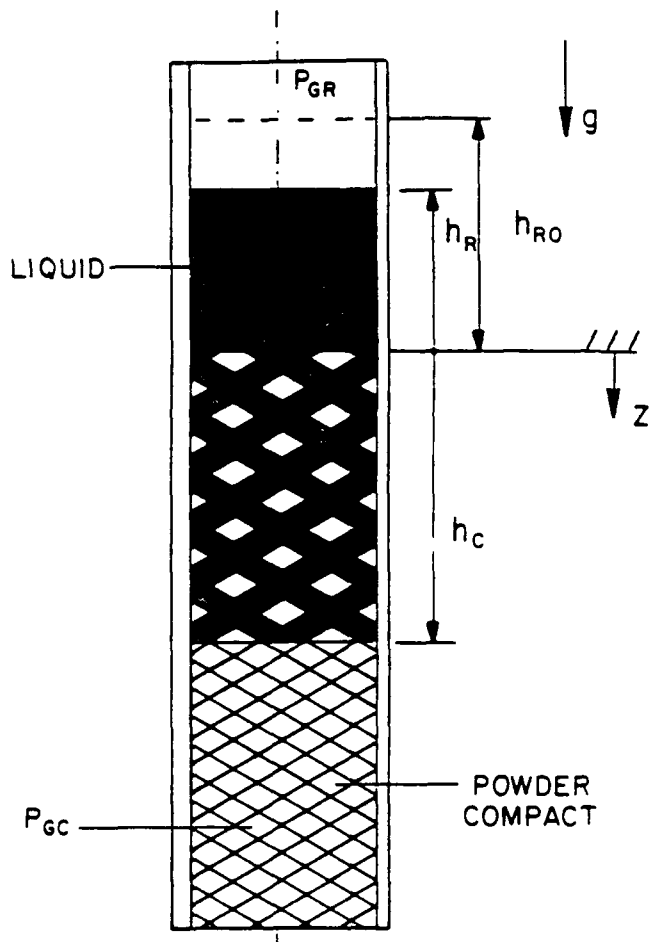


Fig. 4—Schematic illustrating the infiltration of a powder compact.

and

$$\frac{1}{2} \xi^2 = \tau / \lambda_1 \quad (\text{or } h_C \alpha t^{1/2}) \quad [4]$$

where

$$\lambda_1 = \frac{K_1 \mu \langle h \rangle}{(\rho \Delta P_{\text{eff}})^{1/2}} \quad [5]$$

and

$$K_1 = \frac{150(1 - \phi)^2}{\phi^3 d_p^2} \quad [6]$$

In the equations above, ΔP_{eff} is the effective pressure difference across the compact, and ΔP^* is the difference between the applied pressure in the reservoir and the pressure of the gas in the compact.

II. EXPERIMENTAL PROCEDURES

The model indicates that the infiltration rate is dependent on the following properties of the system: (1) pore radius of the compact, (2) viscosity of the liquid, (3) density of the liquid, (4) surface tension and/or contact angle, and (5) applied pressure. The properties selected for study were those associated with the liquid

[i.e., surface tension (γ_n) and contact angle, density, and viscosity]. The alloys selected for comparison to pure aluminum were aluminum-1 wt pct silicon and aluminum-1 wt pct magnesium.

The infiltration temperatures of interest included 1123 K, where aluminum alloys will wet silicon carbide (Figure 1), and near the fusion temperature for aluminum, where reaction with silicon carbide is less severe. The viscosity of aluminum and its alloys shows a sharp increase as the melting point or liquidus is approached. To avoid this behavior, the temperature selected for comparing the alloys was 943 K or 10 K above the melting point of the aluminum. Limited infiltration studies were also made with pure aluminum at 3 K above the melting point and aluminum-1 wt pct silicon at 6 K above the liquidus and 2 K below the liquidus to observe whether any dramatic changes in infiltration behavior occurred at temperatures in the vicinity of the solidus temperature.

The basis for selecting the applied pressure was first to determine experimentally the minimum pressure necessary for infiltration of each alloy at the temperature selected. To define this pressure, referred to as the "threshold pressure," a time limit of 30 minutes was selected within which infiltration either occurred or it was concluded that the applied pressure was below the "threshold pressure." This pressure could be discriminated to within 3 kPa. To resolve the effect of alloying on the infiltration kinetics, data were obtained for each composition using the greatest of the "threshold pressure" for the three alloy compositions investigated.

A. Materials

The silicon carbide used was 100-grit green α -silicon carbide. The chemical composition and particle size analysis of this material are presented in Table I. The average size and shape factor were determined using a JEOL JXA 840 electron probe analyzer with a particle recognition and characterization program. The shape factor is defined as $(\text{perimeter})^2/(\text{area} \times 4\pi)$. The results are presented in Table I. High-purity aluminum (99.95 wt pct) was used in the experiments and for preparing the alloys used. The compositions of the alloys were determined using an Applied Research Laboratories 34000 optical emission spectrometer. The aluminum-silicon alloys were determined to be 1.00 to 1.07 wt pct silicon, and the aluminum-magnesium alloys contained 1.03 to 1.13 wt pct magnesium.

B. Sample Preparation

The infiltration apparatus used for the experiments is shown schematically in Figure 5. A 12.5-mm ID \times 19.0-mm OD \times 92.0-mm-long alumina tube was inserted into a stainless steel tubular fixture. A sintered stainless steel porous plug with a nominal 15- μm pore size was then inserted into the tube. The tube was filled with 8.5 g of the silicon carbide powder and a 6-g aluminum (or aluminum alloy) slug. The slugs used were precast to match the inside diameter of the alumina tube and cut to achieve the desired weight. The sample was then compacted by applying a stress of 72.5 MPa (10,200 psi) to the top of the slug via a punch, using a hydraulic

Table I. Characterization of the 100-Grit Green α -Silicon Carbide

Nominal Composition (Wt Pct)					
SiC	Si	SiO ₂	C	Fe	Al
98.65	0.15	0.63	0.36	0.08	0.08
Particle Size Analysis*					
Parameter		Average	Standard Deviation		
Average diameter (μm)		47.73	24.08		
Maximum diameter (μm)		91.05	40.74		
Minimum diameter (μm)		25.97	17.57		
Shape factor		2.35	0.66		

*Based upon 524 particles evaluated.

press. This applied load assured that the powder compact was pressed uniformly and also provided an upset to the slug, securing it tightly in the tube so that the compact would not be disturbed during handling prior to the experiment.

The sealing arrangement was such that when the SWAGELOK* fitting was tightened, a copper ferrule was

*SWAGELOK is a trademark of Crawford Fitting Company, Solon, OH.

forced to seat onto the inside diameter of the alumina tube, thereby effecting a gas-tight seal. The stainless steel fixture was then connected, by means of SWAGELOK fittings, to a smaller stainless steel tube, which supplied argon to the top of the interior of this assembly.

C. Characterization of Porous Compact

In order to use the model for the prediction of infiltration rate, values for the void fraction, effective particle diameter, and the effective pore radius are required. The last two quantities are not directly measurable for a compact containing different size and shape particles. However, if the void fraction is known, these quantities can be derived experimentally by application of Ergun's equation to a system with established physical properties (Appendix).

The void fraction was determined by adding water to the silicon carbide powder compacts. The specimens were weighed before and after all the voids were filled with water. The open void fraction was then calculated using the weight of the water added.

Pressure drop vs flow rate measurements were then obtained for argon flowing through the silicon carbide compacts contained in the alumina tube. The range of flow rates selected was such that the flow behavior would be similar to that expected in the infiltration studies. This was determined by calculating the range of Reynolds numbers which would be expected in the infiltration study and then determining the argon flow rates which would cover this range.

The Reynolds number, Re , is given by

$$Re = \frac{\rho V_0}{\mu(1 - \phi)S_0} \quad [7]$$

The quantity S_0 is the specific surface area of the particles and given by

$$S_0 = \frac{6}{d_p} \quad [8]$$

and, V_0 , the superficial velocity, is given by

$$V_0 = \phi \frac{dh_c}{dt} = \frac{Q}{A_c} \quad [9]$$

In the above equations, d_p is the average (characteristic) particle diameter and Q is the volumetric flow rate of the gas through the compact. In this regime, only the viscous term in the Ergun's equation is significant, and the equation may be simplified by eliminating the inertial term. (The inertial term would only become significant if the velocities in the infiltration experiment were of the order of meters per second.) Ergun's equation must also take into account the compressibility of the argon. The applicable form becomes

$$\frac{dP}{dz} = K_1 \mu \frac{G_0 RT}{MP} \quad [10]$$

where G_0 is the superficial mass flux ($\rho Q/A_c$), R is the gas constant, T is the absolute temperature, and M is the molecular weight.

On integrating over the length of the compact, this equation becomes

$$\frac{1}{2} (P_s^2 + 2P_s P_b) = K_1 \mu L \frac{RT}{M} G_0 \quad [11]$$

where P_s is the gage pressure measured at the top of the compact, P_b is the ambient (barometric) pressure at the bottom of the compact, and L is the length of the compact. The value of K_1 can then be obtained from the slope of the plot of $1/2(P_s^2 + 2P_s P_b)$ vs G_0 , the slope being equal to $K_1 \mu L R T / M$. Knowing K_1 and ϕ , the effective particle diameter can be calculated from the definition of K_1 and can then be related to the effective pore radius by

$$r_h = \frac{d_p \phi}{6(1 - \phi)} \quad [12]$$

D. Infiltration Tests

The test fixture arrangement within the furnace is presented in Figure 5. To assure temperature uniformity within the working zone, a tube furnace was used with a large length-to-diameter ratio (9.1-m long \times 0.1-m ID). A thermocouple was located in the working zone. The furnace temperature was increased to the test temperature selected and the chamber allowed to equilibrate under a cover gas of 99.998 pct argon at a gage pressure of 3 kPa. Once the furnace reached this target temperature, the specimen was lowered into the working zone, and the gas pressure was increased. The specimen was allowed to reach thermal equilibrium (approximately 90 minutes) before the test began. To initiate the test, the argon supply to the furnace chamber was shut off and the chamber vented to the atmosphere, causing a pressure drop to be developed across the compact. Once

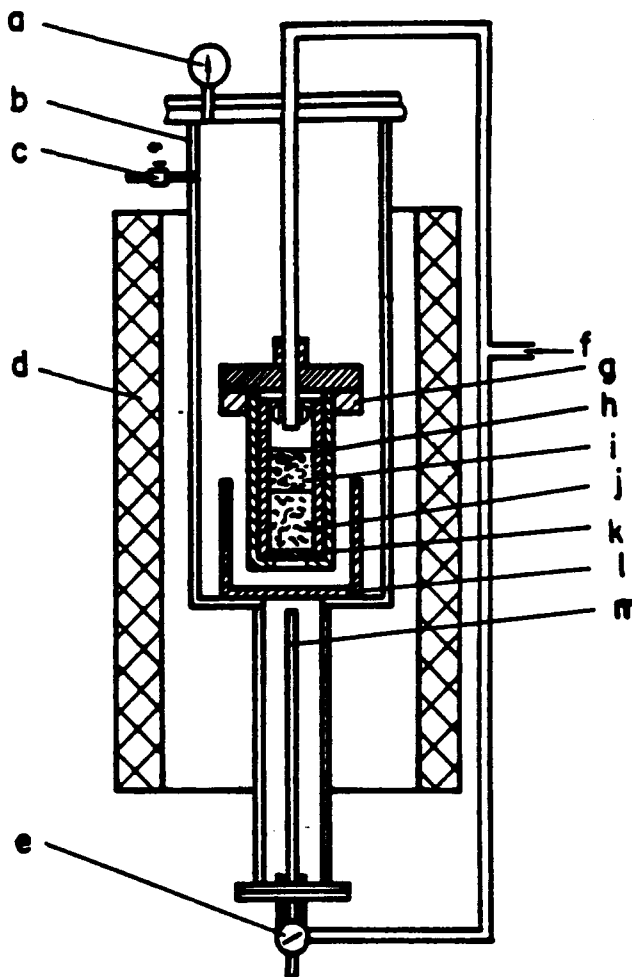


Fig. 5—Schematic of the experimental system: (a) pressure gage, (b) chamber, (c) vent, (d) furnace, (e) valve, (f) argon supply, (g) fixture for holding and sealing Al_2O_3 tube, (h) Al_2O_3 tube, (i) aluminum infiltrant, (j) compact, (k) porous plug, (l) crucible to receive aluminum, and (m) thermocouple.

the desired run time had elapsed, as indicated by a stopwatch, the vent was closed, and the argon supply valve to the chamber was reopened. The specimen was then raised into the cold zone. After the specimen had cooled, it was extracted from the alumina tube using a hydraulic press.

The specimens were examined to obtain the infiltration distance with respect to the infiltration time. They were sectioned longitudinally with a diamond saw, and the infiltration distance along the centerline was measured. Four samples at various stages of infiltration are shown in Figure 6. The data obtained from the partially infiltrated specimen were processed to obtain an average infiltration rate and initiation time by least-squares regression analysis of the model equation (Eq. [4]). Selected samples were also examined using a scanning electron microscope to determine whether there was an effect of the alloy upon the appearance of the silicon carbide/aluminum interface. Photomicrographs of representative samples are shown in Figure 7. Samples were prepared by polishing with 600-grit paper to remove any aluminum that had been smeared over the surface during



Fig. 6—Photograph of compacts at various stages of infiltration. The cross section is approximately 12.5 mm in diameter.

the cutting operation. Coarser grit sizes were not used in order to avoid pulling out the silicon carbide particles from the matrix. The coarse texture of the samples made them unsuitable for optical microscopy at magnifications above 100 times, and no benefit was realized from polishing or etching.

III. RESULTS AND DISCUSSION

The results obtained from characterization of the porous compacts and from the infiltration of the compacts with aluminum are now presented and discussed.

A. Porous Compact Characterization

The flow rates of argon through three silicon carbide compacts were measured over a range of pressure drops.

Each compact was pressed in an alumina tube with a stainless steel porous plug. The results are presented in Figure 8, along with similar data for the porous plug by itself. Linear regression analyses of the data were performed. The nonzero intercept of the regressed lines can be accounted for by a zero offset of the pressure gage used in the measurements. The coefficient of determination for the data was found to be 96.4 pct, indicating good linear correlation. The slope of the upper line is related to the resistance to flow of the argon through the overall system. This resistance is due to contributions provided by the compact and the porous plug in series. Consequently, the individual contribution provided by the compact can be obtained from the difference in the slopes of the lines obtained for the compact and for the porous plug. This quantity, in conjunction with the property values for argon at the test temperature (295 K) and the length of the compacts ($L = 40$ mm), was then used to obtain the value of $K_1 = 2.34 \times 10^{11} \text{ m}^2$.

Five compacts were evaluated for pore (void fraction). The average pore fraction was found to be 0.426 with a standard deviation of 0.007. Using this value in the equation for K_1 (Appendix, Eq. [A11]) provided a value of $51.2 \mu\text{m}$ for the effective particle diameter which agreed well with the particle measurements performed on the scanning electron microscope. The effective (hydraulic mean) pore radius was calculated, from Eq. [12], to be $6.44 \mu\text{m}$.

B. Infiltration Tests

Data obtained from the infiltration experiments are presented graphically in Figures 9 through 14. Included with these data are lines from the linear regression analyses. Table II provides a comparison between the experimental results and predictions using the infiltration model. It is seen that the measured threshold pressures

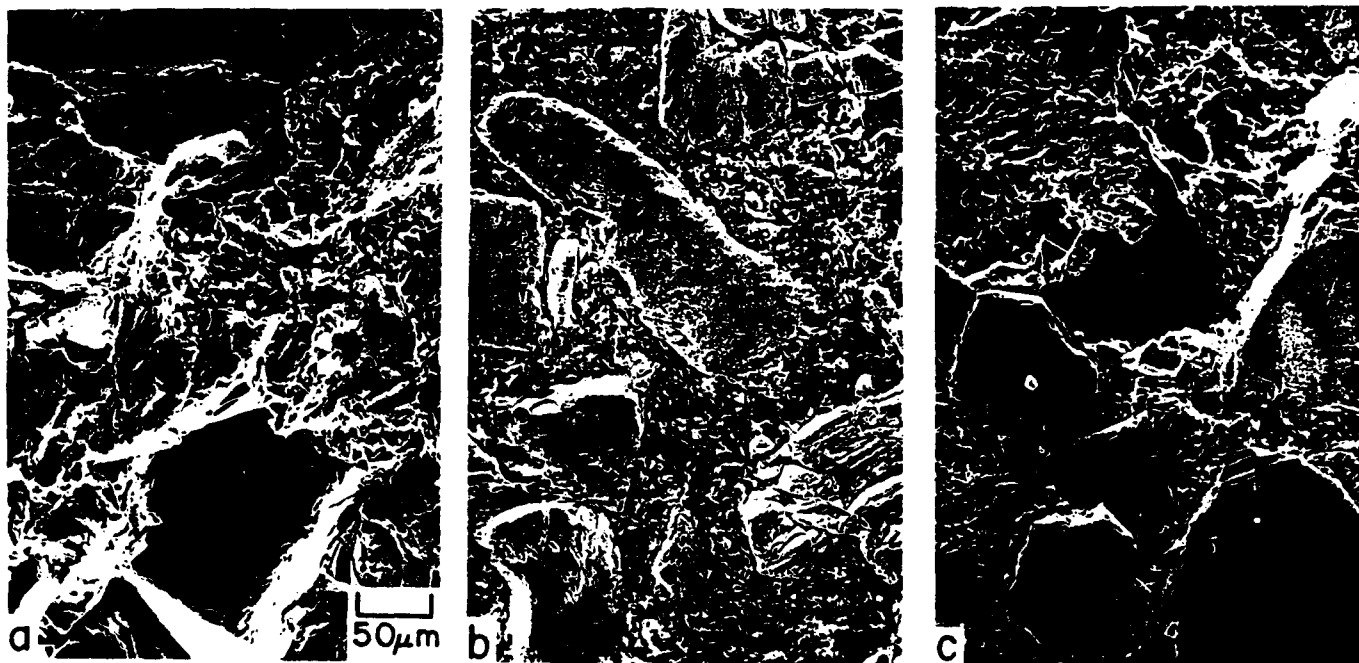


Fig. 7—Photomicrographs of silicon carbide/metal interface: (a) aluminum-1 wt pct silicon, (b) aluminum, and (c) aluminum-1 wt pct magnesium.

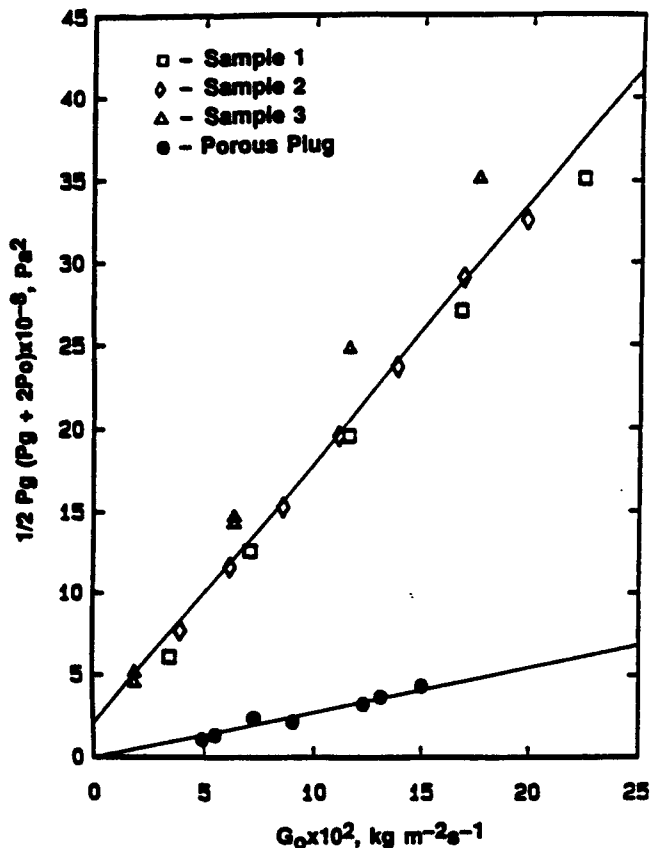


Fig. 8—Pressure drop/argon flow rate correlation used for characterization of compacts. Slope of upper line = $1.573 \times 10^{10} \text{ kg} \cdot \text{s}^{-3}$; slope of lower line = $0.284 \times 10^{10} \text{ kg} \cdot \text{s}^{-3}$.

were consistently lower than predicted, and consequently, the measured infiltration rates were higher. The only factor that could rationally account for these discrepancies was the void fraction of the compact. An increased void fraction would be expected to increase the effective pore radius and decrease the value of K_1 . The void fraction was therefore reevaluated using samples which had been infiltrated. The appearance of the sam-

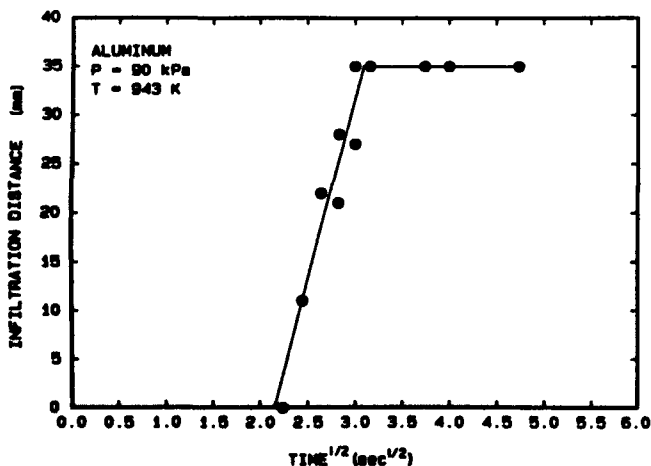


Fig. 9—Infiltration distance vs square root of time for aluminum at 943 K with an applied pressure of 90 kPa.

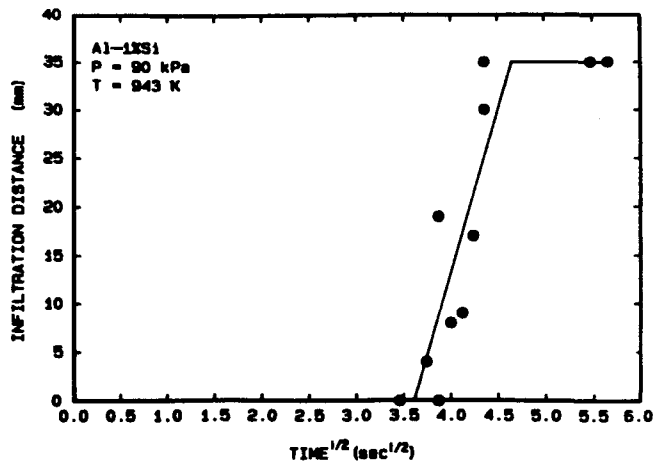


Fig. 10—Infiltration distance vs square root of time for aluminum-1 wt pct silicon at 943 K with an applied pressure of 90 kPa.

ples at low magnification indicated that the void fraction was indeed greater than 0.43, which had been measured prior to infiltration. Photomicrographs were then used to determine the silicon carbide volume fraction by the point count method. The void fraction, the complementary quantity, obtained by this method was 0.80. Based upon this value, the effective pore radius was calculated to be $34.1 \mu\text{m}$, and the extrapolated value of K_1 was $4.47 \times 10^9 \text{ m}^{-2}$. Based upon these values, there was now good correlation between the experimental results and predictions. Apparently, the flow of aluminum into the compact results in significant drag forces (in addition to the buoyancy force) on the silicon carbide particles, which lead to their redistribution and, hence, larger void fraction of the compact.

To calculate the threshold pressures, it was necessary to assign a contact angle value of 155 deg for all compositions and temperatures, due to insufficient data concerning wettability of SiC by liquid aluminum (Figure 1). Discrepancies between the calculated values and experimental results may also be due to the use of bulk thermodynamics to describe a powder compact where the

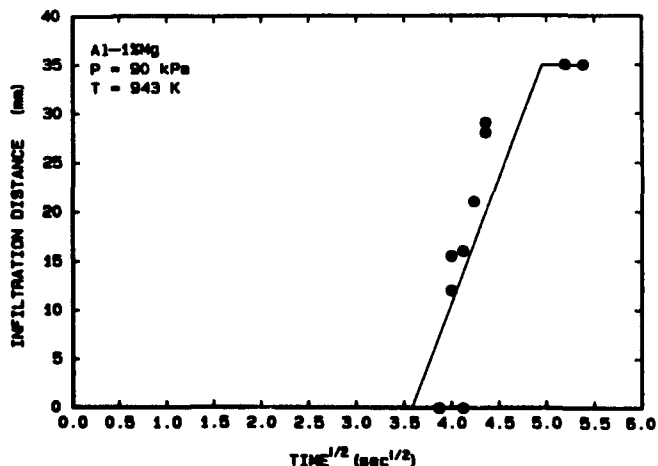


Fig. 11—Infiltration distance vs square root of time for aluminum-1 wt pct magnesium at 943 K with an applied pressure of 90 kPa.

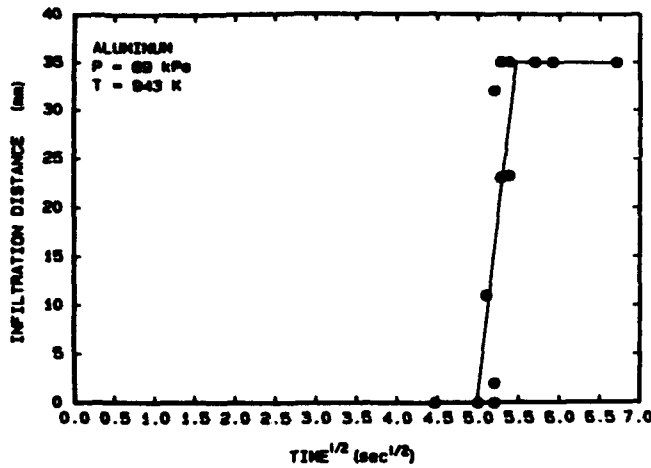


Fig. 12—Infiltration distance vs square root of time for aluminum at 943 K with an applied pressure of 69 kPa.

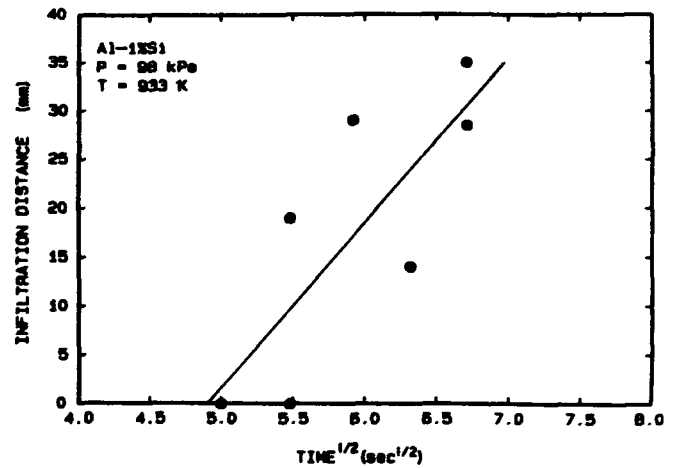


Fig. 14—Infiltration distance vs square root of time for aluminum-1 wt pct silicon at 933 K with an applied pressure of 98 kPa.

surface condition and small radii of curvature of the particles can contribute significantly to the free energy of the system.

The infiltration rates predicted for the systems tested near their threshold pressures are within the 90 pct confidence intervals of the experimental results. At larger values of the effective pressure difference, ΔP_{eff} , the derivations between the experimental results and the predictions cannot be accounted for by experimental error. This indicates that a change in the flow behavior, which may be coupled to void fraction increases, may occur when the applied pressure is increased.

The effect of increasing the applied pressure upon the infiltration behavior of aluminum at 943 K was to decrease the initiation time. Tests run near the liquidus (936 K for pure aluminum and 933 K for aluminum-1 wt pct Si) were characterized by long initiation times and significant scatter in the data, as evident from Figures 13 and 14. These observations may be consistent with the previously reported variability in viscosity near the melting point, which was attributed to short-range ordering prior to the onset of solidification. Also, slight temper-

ature gradients may be present in the preform, resulting in localized regions at temperatures less than the melting point or liquidus. When the temperature was increased to 943 K, the threshold pressure for both the aluminum and aluminum-1 wt pct silicon decreased. In Figure 15, it is seen that the effect is more pronounced for pure aluminum.

Tests performed below the liquidus for the two alloys resulted in the liquid-phase fraction infiltrating the compact, while the solid-phase fraction was trapped at the upper face of the compact. Also, tests conducted at 1323 K demonstrated that contrary to what the available contact angle data indicate, infiltration could not be accomplished without the application of a pressure difference across the compact. Tests conducted at this temperature and without applied pressure for extended periods as long as 24 hours did not result in infiltration.

The initiation time prior to the start of infiltration is obviously due to an unfavorable force balance being present at the start of the test. It is apparent that ΔP_{eff} is not only a function of the applied pressure difference and weight of the liquid (Appendix, Eq. [A15]) but of the interfacial tension term as well. It is conceivable that during the initiation period, contact of the silicon carbide by the liquid aluminum results in modification of the interface, and thus, in the $\gamma_n \cos \theta$ term, such that ΔP_{eff} is greater than zero. Either the passive oxide film on the silicon carbide particle reacts with the molten aluminum or it becomes covered by a capillarity-driven aluminum condensate, which ultimately leads to a favorable ΔP_{eff} for infiltration. The rate of either process should be dependent on both temperature and composition of the aluminum alloy. Furthermore, either an oxide-scavenging reaction or a condensation mechanism would be expected to be thermally activated; *i.e.*, higher temperature tests should be expected to yield higher rates of surface modification and, consequently, shorter initiation times. This appears to be the case when comparing the initiation times for aluminum infiltration at 943 and 936 K (Figures 9 and 13). It should also be noted that the lower temperature test was conducted at a higher applied pressure. This effect of temperature on the initiation time can

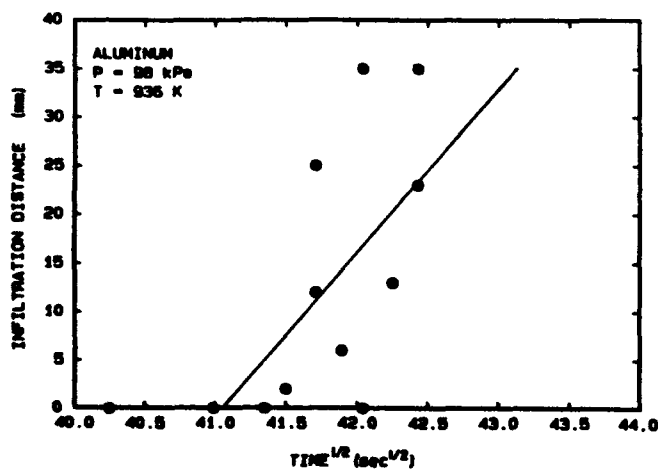


Fig. 13—Infiltration distance vs square root of time for aluminum at 936 K with an applied pressure of 98 kPa.

Table II. Comparison between Experimental Results and Predictions

Alloy	Temperature (K)	ΔP^* (kPa)	Predicted** $\frac{dh_c}{dt}$ ($\frac{\text{mm}}{\text{s}}$)	Measured $\frac{dh_c}{dt}$ ($\frac{\text{mm}}{\text{s}}$)	ΔP_{th} (kPa)
Aluminum	943	90	11	113	71
Al-1Si	943	90*	9	19	71
Al-1Mg	943	90	11	96	67
Aluminum	943	69*	25	19	71
Aluminum	936	98*	6	17	71
Al-1Si	933	98*	6	17	71

*Denotes threshold pressure (+3.5/-0), ΔP_{th} , for Al-1Mg at 943 K is 72 kPa.

**Predictions based upon $\phi = 0.8$ and $\theta = 155$ deg.

also be observed for the aluminum-1 wt pct silicon alloy (Figures 10 and 14).

For higher applied pressure, a smaller increase in the interfacial tension term is required to initiate infiltration (Appendix, Eq. [A15]). This influence of applied pressure is apparent from the initiation times for pure aluminum illustrated by Figures 9 and 12. The smaller applied pressure of 69 kPa resulted in a much longer initiation time for infiltration to commence. Again, this could be due to either the oxide dissolution reaction or to capillarity-driven condensation, since the change in state of the interface which would have to be effected would now be larger, requiring a longer time.

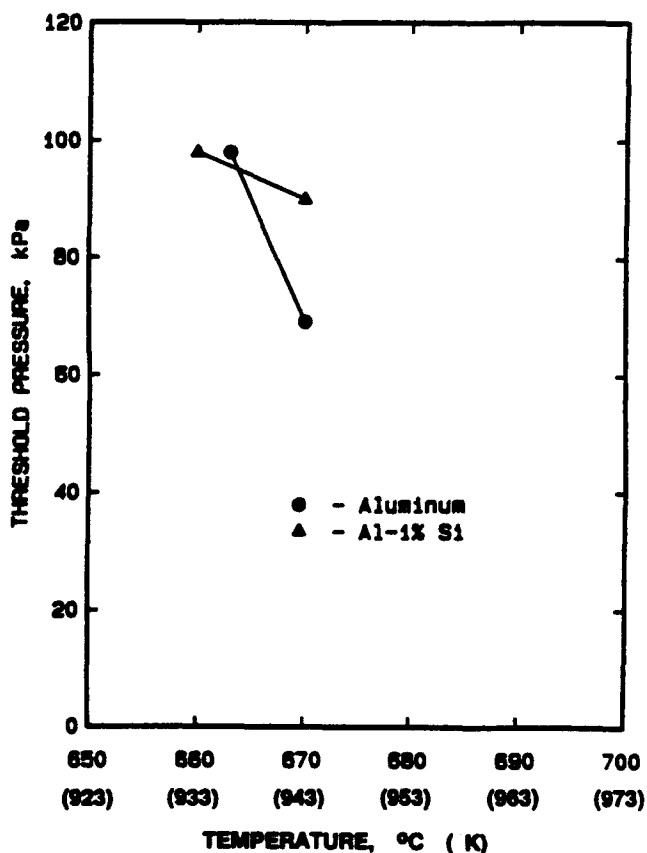


Fig. 15—Threshold pressure vs temperature for aluminum and aluminum-1 wt pct silicon.

Finally, with regard to the photomicrographs showing the interfaces between the metal matrix and silicon carbide particles, it can be seen from Figure 7 that the aluminum and aluminum-1 wt pct magnesium appear to have adhered to the silicon carbide particles. However, this is not the case for the aluminum-1 wt pct silicon alloy.

IV. CONCLUSIONS

There are three important features related to the infiltration of nonwetting porous compacts by liquid metals—the threshold pressure, the incubation time, and the rate of infiltration once it is initiated. While the threshold pressure can be predicted (notwithstanding the uncertainty in surface tension data) and the infiltration rates can be adequately predicted from the models available, the most important aspect of the overall infiltration rate process is the incubation time.

The more important conclusions regarding the experiments conducted are enumerated below:

1. Pressure is required to initiate infiltration of silicon carbide powder compacts with aluminum within the temperature range of 933 to 1123 K.
2. The pressure required for infiltration of silicon carbide compacts with aluminum is dependent on alloy composition. Alloying aluminum with either 1 wt pct silicon or 1 wt pct magnesium was found to increase this pressure, with the effect being greater for the silicon alloy.
3. The pressure required for infiltration of silicon carbide compacts with aluminum decreases with increasing temperature.
4. There is an initiation time associated with the infiltration of silicon carbide compacts with aluminum. This initiation time decreases with increasing pressure and temperature. The mechanism responsible for this phenomenon may be due to either an oxide-scavenging reaction between the liquid aluminum and the silicon carbide particles or a capillarity-driven condensate which covers the surface of the particles.
5. When a silicon carbide powder compact is infiltrated with aluminum, redistribution of particles occurs, which leads to increased void fraction and effective pore radius. It is hypothesized that the drag forces produced by the flow of the liquid metal are responsible for this phenomenon.

APPENDIX

Analysis for infiltration in a nonwetting system

Referring to Figure 4, the total cross-sectional area of the pores, A_v , can be related to the area of the compact by the void fraction

$$A_v = \phi A_C \quad [A1]$$

By continuity, at time t , the height of the liquid in the reservoir, h_R , can be related to the infiltration distance, h_C , by

$$h_R = \phi h_C - h_{RO} \quad [A2]$$

The origin of the coordinate system is located at the interface between the reservoir and the compact, with the positive direction being that in which the fluid flow is induced.

The equation of motion for this model is given by

$$\frac{d}{dt} \left[m(t) \frac{dh_C}{dt} \right] = F_{\text{sp}} + F_{\text{zg}} + F_{\text{zu}} \quad [A3]$$

The difference between this force balance and that developed by Brittin^[13] is that the end drag and surface tension appear within a pressure-related force, F_{sp} , which accounts for the applied pressure and the weight of the liquid.

This force is related to the pressure drop across the porous body by

$$F_{\text{sp}} = \Delta P \phi A_C \quad [A4]$$

where

$$\Delta P = P_{ho} - P_{hc} \quad [A5]$$

Here, P_{ho} is the pressure in the liquid at the reservoir/compact interface, and P_{hc} is the pressure at the infiltrant front. The pressure at the reservoir/compact interface is the result of the applied pressure in the reservoir, P_{GR} , the weight of the liquid above the interface, and the end drag.^[13] The relationship for this pressure can therefore be expressed by

$$P_{ho} = P_{GR} + \rho g h_R - \frac{1}{4} \rho \left(\frac{dh_C}{dt} \right)^2 \quad [A6]$$

The pressure present at the infiltrate front is the result of the pressure on the gas-phase side of the front, P_{GC} , and the pressure due to surface tension (curvature of the liquid front). The expression P_{hc} is therefore given by

$$P_{hc} = P_{GC} - \frac{2\gamma_{lv} \cos \theta}{r_h} \quad [A7]$$

The pressure drop across the compact then becomes

$$\Delta P = P_{GR} - P_{GC} + \frac{2\gamma_{lv} \cos \theta}{r_h} + \rho g h_R - \frac{1}{4} \rho \left(\frac{dh_C}{dt} \right)^2 \quad [A8]$$

The viscous resistance to a fluid flowing through a powder compact can be developed by either interpreting the equation for steady Poiseuille flow through a tube within the context of a quasi-steady process or, more in tune with the physical situation, by using the Ergun

equation (Eq. [A6]). The first approach,^[13] it may be recalled, yields

$$F_{zu} = - \frac{\phi A_C}{r_h^2} 8\mu h_C \frac{dh_C}{dt} \quad [A9]$$

whereas the Ergun equation leads to

$$F_{zu} = -\phi A_C \left[K_1 \mu h_C \frac{dh_C}{dt} + K_2 \rho h_C \left(\frac{dh_C}{dt} \right)^2 \right] \quad [A10]$$

where

$$K_1 = \frac{150(1-\phi)^2}{\phi^3 d_p^2}; \quad K_2 = \frac{1.75(1-\phi)}{\phi^3 d_p} \quad [A11]$$

The gravitational force acting upon the liquid within the compact is

$$F_{zg} = \phi A_C \rho g h_C \quad [A12]$$

The rate of change in momentum (acceleration term) can be further developed to give

$$\frac{d}{dt} \left[m(t) \frac{dh_C}{dt} \right] = \rho \phi A_C \frac{d}{dt} \left[h_C \frac{dh_C}{dt} \right] \quad [A13]$$

On introducing these terms into Eq. [A3] and dividing through by ϕA_C , the following is obtained:

$$\begin{aligned} \rho \frac{d}{dt} \left[h_C \frac{dh_C}{dt} \right] &= \Delta P^* + \frac{2\gamma_{lv} \cos \theta}{r_h} \\ &+ \rho g h_R - \frac{1}{4} \rho \left(\frac{dh_C}{dt} \right)^2 \\ &- \left[K_1 \mu h_C \frac{dh_C}{dt} + K_2 \rho h_C \left(\frac{dh_C}{dt} \right)^2 \right] \\ &+ \rho g h_C \end{aligned} \quad [A14]$$

where $\Delta P^* = P_{GR} - P_{GC}$. It is noted that infiltration will only occur if

$$\Delta P_{\text{eff}} = \Delta P^* + \frac{2\gamma_{lv} \cos \theta}{r_h} + \rho g h_{RO} > 0 \quad [A15]$$

The expression on the left side of the inequality defines the effective pressure difference, ΔP_{eff} . When ΔP_{eff} is zero, ΔP^* is then the threshold pressure difference, ΔP_{th} , which is the applied pressure difference that must be exceeded to initiate infiltration.

The solution to the equation of motion (Eq. [A14]) may be simplified, and the results interpreted on a broader basis, by recasting the equation in dimensionless form. Using τ and ξ to represent the dimensionless values of time and infiltration distance, respectively, the infiltration equation is now expressed as

$$\xi^2 \frac{d^2 \xi}{d\tau^2} + \frac{5}{4} \left(\frac{d\xi}{d\tau} \right)^2 + \lambda_1 \xi \frac{d\xi}{d\tau} = \lambda_2 \xi = 1 \quad [A16]$$

where

$$\xi = \frac{h_C}{\langle h \rangle}; \quad \tau = \left[\frac{1}{\langle h \rangle} \left(\frac{\Delta P_{\text{eff}}}{\rho} \right)^{1/2} \right] t \quad [A17; A18]$$

$$\lambda_1 = \frac{K_1 \mu \langle h \rangle}{(\rho \Delta P_{\text{eff}})^{1/2}}; \quad \lambda_2 = (1 - \phi) \frac{\rho g \langle h \rangle}{\Delta P_{\text{eff}}} \quad [\text{A19; A20}]$$

and $\langle h \rangle$ is a reference height of some arbitrary (but convenient) value. It should also be noted that the term containing K_2 has been neglected, since it is small compared to the term containing K_1 .

For the system being studied, λ_1 is large relative to the other terms on the left side of the equation, once infiltration has been initiated. Consequently, these terms may be neglected by comparison; thus, on integrating, the approximate solution obtained is

$$\frac{1}{2} \xi^2 = \frac{\tau}{\lambda_1} \quad (\text{or } h_{\text{cat}}^{1/2}) \quad [\text{A21}]$$

ACKNOWLEDGMENTS

This research was supported by the Strategic Defense Initiative Office/Innovative Science Technology, Contract No. N00014-85-K-0451. The encouragement and support of Dr. Steven Fishman are gratefully acknowledged. The authors also acknowledge the generosity of the Coors Ceramic Company, Golden, CO, for their contribution of the experimental materials.

REFERENCES

1. I.J. Toth, W.D. Brentnall, and G.D. Menke: *J. Met.*, 1972, vol. 24, pp. 19-25.

2. T.W. Clyne and M.G. Bader: *5th Int. Conf. on Comp. Mater.*, San Diego, CA, TMS, Warrendale, PA, 1985, pp. 755-71.
3. A. Banerji, P.K. Rohatgi, and W. Reif: *Metallwiss. Tech.*, 1984, vol. 38, pp. 656-61.
4. J.A. Cornie, A. Mortensen, M.N. Gunger, and M.C. Flemings: *5th Int. Conf. on Comp. Mater.*, San Diego, CA, TMS, Warrendale, PA, 1985, pp. 809-23.
5. L. Froyen and A. Deruyttere: *Proc. 4th Eur. Symp. on Mater. Sci. under Microgravity*, Madrid, Spain, European Space Agency, Paris, France, 1983, pp. 31-36.
6. R. Mehrabian, R.G. Rick, and M.C. Flemings: *Metall. Trans.*, 1974, vol. 5, pp. 1899-1905.
7. A. Sakamoto, H. Hasegawa, and Y. Minoda: *5th Int. Conf. on Comp. Mater.*, San Diego, CA, TMS, Warrendale, PA, 1985, pp. 699-707.
8. L. Ackermann, J. Charbonnier, G. Desplanches, and H. Koslowski: *5th Int. Conf. on Comp. Mater.*, San Diego, CA, TMS, Warrendale, PA, 1985, pp. 687-98.
9. T.W. Clyne, M.G. Bader, G.R. Cappleman, and P.A. Hubert: *J. Mater. Sci.*, 1985, vol. 20, pp. 85-96.
10. F.M. Hosking and A.A. Netz: *Liquid Metal Infiltration of an Aluminum Alloy into a Packed Column of B, C Particles*, Research Report No. SAND-83-2573, Sandia National Laboratory, Albuquerque, NM, 1984.
11. R. Warren and C.H. Andersson: *Composites*, 1984, vol. 15, pp. 101-11.
12. K. Shinohara and S. Umekawa: *Bull. P.M.E. (T.I.T.)*, 1984, vol. 54, pp. 17-21.
13. W. Kohler: *Aluminum*, 1975, vol. 51, pp. 443-47.
14. A.J. Shaler: *Int. J. Powder Metall.*, 1965, vol. 1, pp. 3-14.
15. W.E. Brittin: *J. Appl. Phys.*, 1946, vol. 17, pp. 37-44.
16. J.R. Ligenza and R.B. Bernstein: *J. Am. Chem. Soc.*, 1951, vol. 73, pp. 4636-38.
17. K.A. Semlak and F.N. Rhines: *AIME Trans.*, 1958, vol. 212, pp. 324-31.
18. G.P. Martins, D.L. Olson, and G.R. Edwards: *Metall. Trans. B*, 1988, vol. 19B, pp. 95-101.

**WETTING OF CERAMIC BY MOLTEN METALS:
RATE CONTROLLING PHENOMENA**

P. R. Chidambaram, G. R. Edwards, and D. L. Olson
Center for Welding and Joining Research
Colorado School of Mines
Golden, Colorado 80401

Abstract

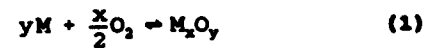
Formation of interfacial chemical bonds between the mating surfaces is treated as the critical event in the wetting of ceramics by molten metals. The oxide layer present on the molten metal acts as a barrier to interfacial reaction. Transport of material through this oxide layer is treated as the rate controlling phenomenon. The observed wetting behavior of molten metals on ceramics is explained using this approach. Experimental data available in the literature is used to estimate an activation energy for the process. Concepts from point defect chemistry are used to classify the various metals according to the nature of oxide they form and relate the nature of oxide to the observed wetting behavior. Oxides that exhibit stoichiometric compositions are protective in nature, and the corresponding metals exhibit a time dependent wetting behavior. Aluminum, magnesium and chromium do not instantly wet ceramics for this reason. Conversely, non-stoichiometric oxides of titanium, manganese and molybdenum possess sufficient lattice and electronic defects to rapidly transport the metal ions across the oxide layer. Doping the oxide lattice can alter the transport behavior of material through the oxide lattice.

Introduction

A liquid is defined to wet a ceramic when the liquid spreads to form an intimate contact on the solid surface. Wetting in metal-ceramic systems occur essentially by chemical bond formation. In an earlier study, a thermodynamic approach was used to predict the wetting behavior of liquid metal on ceramic substrates [1]. Wetting was treated as a surface phenomenon. It was established that wetting occurs when the liquid metal has sufficient thermodynamic activity to reduce the surface phase of the ceramic; surface phase is more amenable for reduction than the bulk of the material.

Reactions mentioned above are possible only when the liquid metal is available at the ceramic surface for interfacial phase formation. At experimentally attainable oxygen partial pressures, most metals form an oxide layer that is a few Å thick on the surface. In joining, the braze metal is melted in between the two ceramic components, while some metal-matrix composite materials are fabricated by infiltrating the reinforcement with the molten metal. In both cases the existing environmental gas mixture is adsorbed on the ceramic surfaces. When the liquid metal comes in contact with the ceramic, it oxidizes from this adsorbed gas mixture. This situation is described schematically in Figure 1. The liquid metal reacts with oxygen in the environmental gas mixture according to the following

equation:



The oxygen partial pressure, P_{O_2} required for this reaction to occur is given by:

$$P_{O_2} = k^{2/x} = e^{\left(\frac{\Delta G^\circ}{RTx}\right)} \quad (2)$$

where k is the reaction constant, ΔG° is the standard free energy change for reaction in Eqn. 1, R is the gas constant and T is the temperature in degree Kelvin. The oxygen partial pressures required to oxidize many reactive metals can be calculated using thermodynamic handbook data [2]. The oxygen partial pressures shown in Table I are calculated for a reaction at 1300° K.

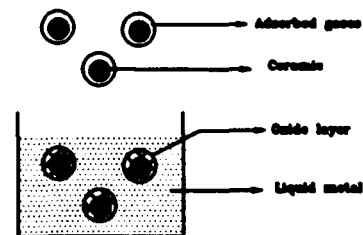
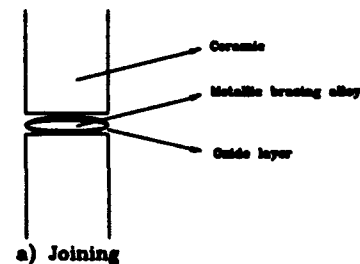


Figure 1 Schematic Representation of the Formation of an Oxide Barrier

Table I. Oxygen Partial Pressures Required to Form an Oxide Layer at 1300°C

Metal	Oxide	ΔG° kJ/mole	P_{O_2} atms
Al	$\alpha\text{-Al}_2\text{O}_3$	-1262.18	$1.8 \cdot 10^{-34}$
Mg	MgO	-458.15	$1.5 \cdot 10^{-37}$
Cr	Cr_2O_3	-799.86	$3.7 \cdot 10^{-22}$
Ti	TiO_2	-726.96	$6.1 \cdot 10^{-30}$
Mn	MnO	-289.61	$5.2 \cdot 10^{-24}$
Mo	MoO_2	-355.17	$5.3 \cdot 10^{-15}$

The adsorbed environmental gas mixture invariably contains oxygen gas at a partial pressure of above 10^{-15} atms. Therefore, a solid oxide layer forms between the metal and the ceramic when a drop of liquid metal comes in contact with the surface of the solid. Hence, a reaction between the molten metal and the ceramic is possible only when the metal overcomes the protective nature of the oxide layer.

In the following section on wetting behavior, the information available in the literature concerning the role of oxide barriers in the wetting of ceramics by molten metals and alloys is summarized. A transport model that attempts to explain the observed behavior is described. The effect of alloying and other characteristics of transport through the oxide layer are discussed in the final section.

Wetting Behavior

Liquid aluminum does not readily wet most solids because the oxide layer prevents the metal from any possible reaction. Foundrymen have effectively taken advantage of this phenomena; they use permanent moulds made of graphite to cast aluminum components. Aluminum does not wet the mould, even when a chemical reaction between aluminum and graphite is thermodynamically favorable, because of the oxide barrier.

Programs aimed at developing commercial aluminum matrix composites have demonstrated some ingenious ways to produce commercially viable components. Mechanical destabilization of the oxide layer formed on the molten metal [3] and oxidation of the metal to form an insitu ceramic reinforcement [4] are some of the examples.

Wettability studies performed using liquid aluminum on ceramic substrates have identified a time dependence in the wetting behavior [5,6]. Below 1223°K there exists an incubation time before liquid aluminum can wet the ceramic. Above 1223°C wetting is more or less instantaneous. This kind of a transition behavior has been observed in many ceramics such as silicon carbide [5], aluminum oxide, [6] carbon [7] and titanium boride. Many studies have attributed this transition behavior to the oxide layer that forms on liquid

aluminum [5,6,8].

Laurent et. al. have studied the wetting behavior of aluminum on silicon carbide as a function of time [5]. They used the sessile drop technique to measure the contact angle; a molten drop of aluminum was placed in a controlled atmosphere on the ceramic substrate, and the solid angle subtended by the liquid drop on the metal was measured by an optical microscope. They measured the contact angle as a function of time at three different temperatures. The results obtained in their study are shown in Figure 2.

Alloying liquid aluminum alters the transition temperature. Transition temperature is the temperature

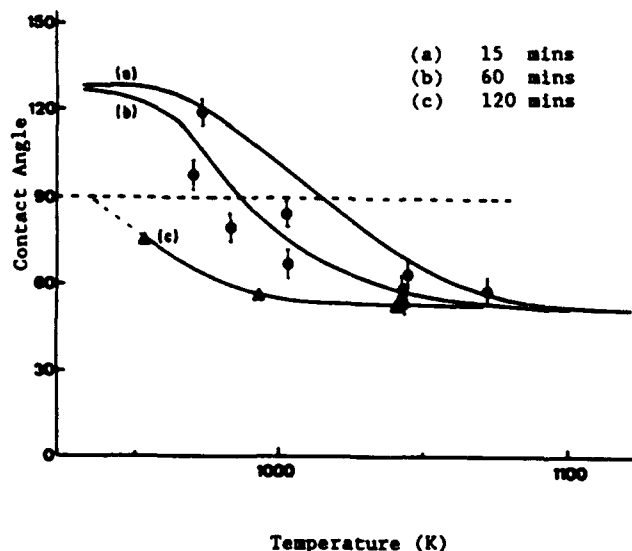


Figure 2 Contact Angle as Function of Time for Aluminum on Silicon Carbide [5]

above which wetting occurs instantaneously [8]. Table II. summarizes the effect of alloying on the transition temperature (after Warren [8]). Also, Laurent et. al., in the study mentioned earlier, found a moderate decrease in the transition temperature after alloying liquid aluminum with silicon [5].

The oxide barrier problem has been identified only in the case of liquid aluminum. However, metals such as titanium, manganese and molybdenum also form oxide layers at any experimentally attainable oxygen partial pressures (Table I). Titanium, in fact, is the essential component in the development of active braze material [9]. A few percent titanium is sufficient to wet many ceramics, such as aluminum oxide, carbon, graphite, silicon carbide [10]. The same is true for molybdenum and manganese; these two metals have been used, for a long time, in metal-ceramic sealing applications [11]. No evidence of a protective oxide layer on these metal surfaces has been reported.

Not all effects of the oxide layer are deleterious. Most metal-ceramic interfacial phases are relatively brittle, and a large interfacial zone formation results in a premature failure of the composite [8]. Using silicon carbide as an example

Table II. The Wetting Transition Temperatures of α -SiC Single Crystals With Al-Alloys [8]

Alloy (weight %)	Wetting transition temperature (°C) for $\theta = 90^\circ$
Pure Al	960
AlMgSi1	920
AlCuMg1	1010
AlCuMg2	990
AlZnMgCu1.5	900
Al-2Mn	1030
Al-5Mn	930
Al-2Ni	1035
Al-5.7Ni	1080
Al-1Co	1060
Al-2Co	1025
Al-La(2-8)	1025
Al-Ce(5-10)	1070

ceramic, according to the reaction thermodynamics, the following reaction can occur at the surface:



The ΔG_r for the above reaction is negative; hence, aluminum has sufficient thermodynamic activity to reduce the bulk of silicon carbide. Therefore, a stable interface can never be formed between liquid aluminum and silicon carbide. Aluminum carbide formation can only be limited by the kinetics. The oxide barrier that forms on the aluminum surface provides a good control on the kinetics of reduction, and prevents an explosive reaction between the ceramic and aluminum. However, the oxide layer that forms on titanium is not protective in nature titanium reacts rapidly at any interface where a thermodynamic driving force for reaction is present. This problem has been observed in studies of the SiC-Ti [8] interface. Therefore, knowledge of the origin and nature of oxide barrier protection could be an effective tool to control the kinetics of interface formation. The mechanism of this barrier protection and the reason for the time dependence of this phenomena are not fully understood. The following section describes one possible mechanism to explain the observed behavior.

Transport Model

The observed experimental anomalies can be explained using a transport model that treats the diffusion of metal ions through the oxide lattice as the rate controlling step for wetting.

The inverse of time taken for a transition from non-wetting to wetting (time when the contact angle reaches 90°) can be defined as the wetting rate. This information is available as a function of temperature for liquid aluminum in contact with silicon carbide [5] and is used here to estimate the activation energy involved in the wetting kinetics. An Arrhenius equation:

$$\frac{1}{t} = A e^{-\frac{Q}{RT}} \quad (4)$$

is used to analyze the experimental data. Using the wetting rate ($1/t$) data at different temperatures an activation energy, Q was calculated to be 301 KJ/mole. This activation energy measures the slowest of the various time dependent wetting phenomena.

Diffusional creep studies have been used to measure the intrinsic and extrinsic diffusion coefficients in ceramic materials. Gorden [12] has tabulated both the grain boundary and lattice diffusion coefficients for aluminum diffusion in aluminum oxide. From his analysis, the activation energy for aluminum diffusion in aluminum oxide is in the range of 400 KJ/mole. The diffusion of the aluminum ions through the oxide barrier could be the rate controlling step in the wetting of silicon carbide by aluminum.

The necessary information to prove if transport of aluminum is the rate controlling step in the non-wetting to wetting transition cannot be obtained from sessile drop experiments. The contact angle is a function of many factors. Surface porosity has a strong influence on the spreading behavior. Furthermore, the rate of change of contact angle is not an accurate measure of the activation process. A direct measure of the fractional formation of interfacial phase would be a better parameter with which to study the activation process. An unequivocal conclusion cannot be obtained unless independent experiments are performed to identify the kinetics of the interfacial phase formation. Experiments of this nature are in progress at the Colorado School of Mines.

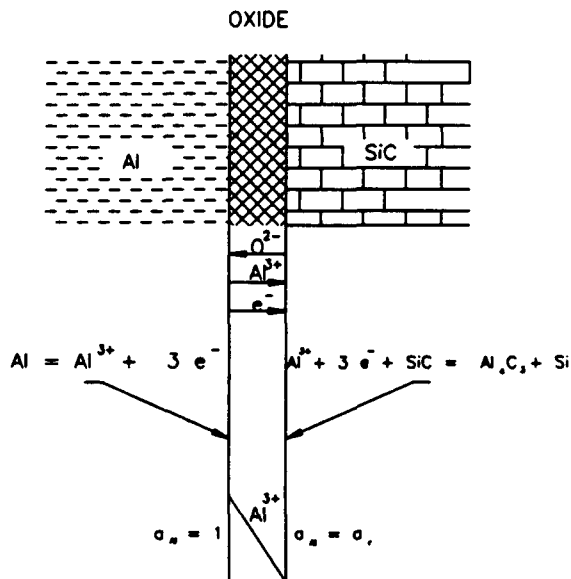


Figure 3 Schematic Representation of the Transport Processes Involved in The Interface Formation

Figure 3 shows a schematic representation of the transport processes involved during the interface formation. The oxide skin forms on the liquid metal using the oxygen from the adsorbed atmospheric gases. The thickness of the skin is related to the amount of oxygen that is adsorbed on the surface. In reducing atmospheres it could be very low. Once all the adsorbed

oxygen is depleted, further transport of aluminum ions results in the formation of aluminum carbide at the interface. Diffusion of the metal through the oxide requires the transport of both the metal ions and electrons. The metal atoms ionize at the metal/oxide interface and diffuse through the lattice. For the reaction between the aluminum ions and the ceramic to be complete, the electrons from the oxide/metal interface must reach the oxide/ceramic interface. Transport of metal ions is dependent upon the concentration of the metal ion vacancies or interstitials in the oxide - vacancies more often than interstitials.

Transport of metal ions in ionic material is treated mathematically using the diffusion coefficient, D_{Al} :

$$D_{Al} = \gamma \lambda^2 [V_{Al}'''] \exp \frac{-\Delta G_m}{RT} \quad (5)$$

where γ is the Debye frequency, λ is the jump distance, $[V_{Al}''']$ is the concentration of vacant aluminum sites, and ΔG_m is the free energy for motion.

The electron transport is dependent upon the concentration of the electronic defects. Because alumina is a wide band gap material (band gap = 8.2 eV) the equilibrium electronic defect concentration at low temperatures ($T < 1600^\circ C$) is very low; therefore, aluminum oxide is an insulator at these temperatures. The equilibrium number of vacancies and electronic defects in the oxide are determined by the free energy of formation of various defects - intrinsic and extrinsic. The concentrations of these defects can be manipulated very effectively using a good understanding of the point defect chemistry.

Point Defect Chemistry

Defects in a material can be treated as separate species and unique thermodynamic properties can be associated with these defects. Therefore, the standard thermodynamic equations can be used to determine the equilibrium concentrations of these defects. Oxide materials contain three types of native defects: Schottky, cation Frenkel and anion Frenkel defects.

In pure alumina, the vacant aluminum ion concentration is a sum of contributions from the Frenkel and Schottky defects. To make an estimate of the kinetics of diffusion of the cations, prior knowledge of the free energy of formation of these defects is essential. Theoretical modeling studies have evaluated the enthalpies of point defect formation to a reasonable accuracy [13].

When liquid aluminum is alloyed, the oxide layer that forms on the metal is automatically doped with the alloying addition. To alleviate the mass and charge imbalance created by the presence of impurities in the oxide lattice, more vacancies, interstitials or electronic defects are created. The actual vacancy concentration is a function of the concentration of the impurity atom present in the oxide lattice. For example, the oxide layer on an aluminum-silicon alloy would be doped with silicon; this can be treated in point defect chemistry by writing a defect reaction for silicon dioxide in aluminum oxide as follows:



The above reaction is only one of many defect reactions that can occur. The reaction with the lowest free energy

for the temperature of interest will dominate the defect properties. If the reaction shown in Eqn. 6 were to be the dominant reaction at the temperature of interest (assuming that sufficient electronic defects exist) the excess V_{Al} would enhance the diffusion of aluminum through the oxide lattice. This is identically true for any supervalent alloying element such as silicon, titanium, zirconium that is present in the aluminum oxide lattice.

Experimental evidence indicates that the supervalent additions to liquid aluminum decrease the wetting transition temperature (Table II). Also, the diffusion coefficient for lattice and grain boundary diffusion coefficient decreases by three orders of magnitude when aluminum is alloyed with supervalent elements [12].

A subvalent alloy addition, on the contrary, decreases the vacant aluminum ion concentration according to the following reaction:

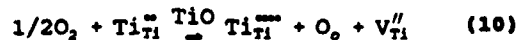


Defects can be formed in the oxide lattice simply by virtue of the equilibrium oxygen partial pressure. The free energy of formation is a constant at a given temperature for all metal oxides. Therefore, a stoichiometric oxide can be in equilibrium with its parent metal only at a particular oxygen partial pressure. For any metal oxide MO, if the surrounding partial pressure is different, one of the following two reactions occurs:



The magnitude of the difference between the environmental partial pressure and the stoichiometric partial pressure together with the free energy change associated with the above reactions control the extent to which the vacancies and electronic defects are present in the material.

The presence of vacancies causes a deviation from the stoichiometric metal:oxygen ratio of 1:1. The deviation can be represented mathematically as MO_{1-x} , where x is the non-stoichiometric parameter. For metal-oxides like titanium oxide, x can vary from 0 to 0.35. Table III shows the experimentally measured x values from the monograph on non-stoichiometry [14]. It is obvious from the table that the oxides of metals with multiple oxidation states show large deviations from stoichiometry. Consider the titanium oxide lattice. If some titanium ions in the lattice are promoted to a higher oxidation state, more equilibrium vacancies are created:



The free energy change for the above reaction can be expected to be reasonably small. Therefore, material transport through the titanium oxide lattice can occur with relative ease. In contrast, a reaction of the type shown in Eqn. 10 does not occur in aluminum, magnesium or chromium. Therefore, they form stable oxide layers. This explains why aluminum, magnesium, and chromium brazing consumables are not commonly used.

The metal-ceramic wetting literature shows evidence that titanium, zirconium, manganese and molybdenum have been repeatedly used in the industry to

Table III. Non-Stoichiometry Parameter X for Various Metal Oxides [14]

Oxide	Non-Stoichiometry (X)
TiO	-0.35 - +0.35
MnO	-0.15 - +0.15
FeO	+0.1
NiO	+0.001
Cr ₂ O ₃	not
MgO	measurable
Al ₂ O ₃	(< -0.0005)

promote wetting. Being reactive, they possess the thermodynamic activity to react with most ceramic compounds. However, another advantage with these metals is their multiple oxidation states; a large vacancy concentration in their oxide lattice causes a rapid transport of metal ions through the oxide layer.

Conclusions

The following conclusions can be drawn from the previous discussion:

- 1 Transport through the intervening oxide layer is the rate controlling phenomena in the wetting of ceramics by molten metals.
- 2 Metals with multiple oxidation states form oxides with a large degree of non-stoichiometry; and therefore wet ceramic substrates instantly because the ionic transport through such oxide barrier is very rapid.
- 3 Time dependent wetting by stable oxide formers is related to the rate of material transport through the oxide lattice; alloying additions to the molten metal can alter the rate of material transport.

References

1. P. R. Chidambaram, G. R. Edwards, and D. L. Olson, "A Thermodynamic Criterion to Predict Wettability at Metal-Ceramic Interfaces", submitted for publication in Met. Trans. B.
2. JANAF Thermochemical Tables, 2nd edition, (U. S. Dept. of Commerce, 1977, 20-257).
3. R. Mehrabian, R. G. Risk, and M. C. Flemmings,

"Preparation and Casting of Metal-Particulate Non-Metal Composites", Met. Trans., 5 (1973), 1899.

4. M. S. Newkirk et al., "Preparation of Lanxide™ Ceramic Matrix Composites: Matrix Formation of Direct Oxidation of Molten Metals", Ceram. Eng. Proc., 8 [7-8] (1987), 879.
5. V. Laurent, D. Chatain, & N. Eustathapoulos, "Wettability of SiC by Aluminum and Al-Si Alloys", J. Mater. Sci., 22 (1987) 244.
6. J. J. Brennan, and J. A. Pask, "Effect of Nature of Surface on Wetting of Sapphire by Liquid Aluminum", J. Amer. Ceram. Soc., 51 (1968), 569.
7. N. Eustathapoulos, J. C. Joud, P. Desse, & J. M. Hitcher, "The Wetting of Carbon by Aluminum and Aluminum Alloys", J. Mater. Sci., 9 (1974), 1223.
8. R. Warren, and C. H. Anderson, "Silicon Carbide Fibers and Their Potential for Use in Composite Material Part II", Composites, 15 (1984) 101.
9. H. Mizuhara, (1986), U.S. Patent No. 4603090.
10. Yu Naidich, "Wettability of Solids by Liquid Metals", Prog. in Surf. and Membrane Sci., 14 (1981), 353.
11. M. Erg, and A. W. Hennicke, "Ceramics in Advanced Energy Technologies", ed. H. Krockel et al., (Dreidel Publishing Co., 1982, 138).
12. R. S. Gorden, "Understanding Defect Structure and Mass Transport in Polycrystalline Al₂O₃ and MgO via Diffusional Creep": Advances in Ceramics, vol. 10, ed. W. D. Kingery 1984, 418.
13. W. C. Mackrodt, "Calculated Point Defect Formation Association and Migration Energies in MgO and α -Al₂O₃": Advances in Ceramics, vol. 10, ed. W. D. Kingery 1984, 62.
14. Per Kofstad, Nonstoichiometry, Diffusion, and Electrical Conductivity in Binary Metal Oxides, (Wiley Interscience, New York, 1972 101-300).

Acknowledgments

This research was supported both by the Strategic Defense Initiative Office/Innovative Science and Technology under ONR Contract #N00014-88-K-0500 and by the Welding Research Council. The encouragement of Dr. Steven Fishman is gratefully acknowledged.

Modeling of Brazing Processes That Use Coatings and Interlayers

Transport behavior of chemical elements at the braze interface is emphasized in the modeling of three coatings

BY S. LIU, D. L. OLSON, G. P. MARTIN AND G. R. EDWARDS

ABSTRACT. The possibility of using the new coating technologies in brazing is examined. By depositing one or more layers of filler metals on the joint surfaces, traditionally difficult-to-join materials can be brazed together. Barrier coatings, coatings for dissolution-solidification, and reactive metal coatings (interlayers) are the three different groups of coatings discussed. To control brazing, the optimal amount of coating applied must be determined and the interfacial chemical reactions must be understood, with the characterization of the products that result in the braze metal. Mathematical modeling of brazing using the three types of coatings is performed to describe the transport of chemical elements at the braze interface.

Introduction

The brazing of advanced engineering materials, and especially dissimilar materials, is coupled to the effective use of coatings. The most obvious application is to use the coating process to establish a highly wettable surface for the liquid filler metal. The coating may also be used as a barrier when the brazing filler metal is incompatible with the base material, to avoid diffusion of certain alloying elements and to prevent intermetallics formation.

Recent approaches (Ref. 1-3) to coating technology in brazing recognize that coatings are no longer just an intermediate passive barrier, but they take an active part in the brazing process. Mass transport, either from the brazing filler metal into the base material or the dissolution of the coating into the braze metal, can promote physical changes, such as increasing the liquidus temperature of the braze metal, which affect significantly the brazing process. With proper selection of the coating material and brazing filler metal,

very consistent brazing processes can be developed. The control of the chemical composition and thickness of the coating layers are far more critical than that required in traditional brazing filler metals. This paper places emphasis on the existing coating technology applied in brazing and presents an analysis of the mass transport behavior of these advanced coating-brazing processes. With the proper understanding and knowledge of the behavior of these coatings, filler metals and processing conditions can be selected according to sound engineering principles. It is postulated that joining of difficult-to-join materials should be possible by applying multiple coatings, which create conditions such as wetting and chemical affinity between the faying surfaces.

Brazing Coating Technology

There are many ways to apply coatings on parts to be brazed. They are: 1) electrolytic: electroplating or electroless deposition; 2) thermal: dip coating, barrel coating, roller coating, flow melting, etc.; 3) surface modification: cladding, thermal spraying, plasma spraying, etc.; and 4) physicochemical: sputtering deposition, vapor deposition, ion implantation, etc. Since both chemical homogeneity and thickness are important properties of a coating, the coating procedure must be well controlled. For components that require critical dimensional control, continuous sputter-cleaning and vapor deposition-type processes are preferred because of the uniform adhesion obtained at the interfaces.

Three different coating schemes are described below, each serving a specific

function in brazing. They are: 1) barrier coatings, 2) reactive metal coatings, and 3) coatings for dissolution-solidification.

Barrier Coatings

It has been common practice, when no known suitable brazing filler metal is available for the materials to be joined, to use a coating that can be wetted by the liquid braze (Ref. 4). The coating also serves as a barrier between the base metal and the braze during processing. A barrier layer must be dense, ductile and free from defects such as voids. It must also show good adhesion and wetting toward both the base and filler metals. Copper-phosphorus filler metal had been used in the past to join ferrous alloys; however, intergranular penetration of phosphorus was observed to promote subsurface embrittlement of the joint. A thin undercoating of nickel reduced phosphorus diffusion and provided good wetting for the copper-phosphorus filler metal (Ref. 5). Similar techniques are used in soldering brasses. A 1- to 2- μm -thick layer of nickel or copper barrier coating is often used to avoid zinc diffusion to tin or tin-lead filler metals (Ref. 6). In electronic packaging, tin-lead alloys alone will not wet a ceramic substrate. A layer of silver or gold of adequate thickness is often deposited to provide a wettable surface for the tin-lead alloys (Ref. 4).

Sometimes the barrier coating scheme may require a double coating. Material for the first layer is selected for its compatibility with the base metal and the second layer (overlayer or outer coating) is used to promote wetting with the liquid brazing filler metals, as illustrated in Fig. 1. The primary layer is generally a transition metal solution containing polyvalent elements such as titanium, manganese, zirconium, tantalum, or molybdenum, where the polyvalent states increase the bonding tendency. The second layer is usually a thin layer of noble metal which provides a surface that is oxide-free, or with a very thin oxide layer which readily decomposes or dissolves during brazing. Such oxygen-free surfaces have, in general,

KEY WORDS

Brazing Filler Metal
Brazing Coatings
Transient Liquidus Phase
Modeling
Brazing Metallurgy
Filler Metal Selection

S. LIU, D. L. OLSON, G. P. MARTIN and G. R. EDWARDS are with the Center for Welding and Joining Research, Colorado School of Mines, Golden, Colo.

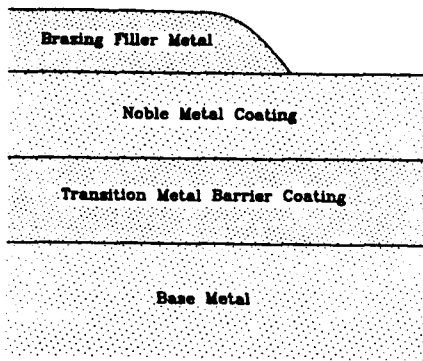


Fig. 1—Schematic diagram showing the noble metal and transition metal barrier coatings inserted between the base metal and the brazing filler metal.

high surface energy and offer excellent wettability. Metals such as silver, gold and copper serve this function, requiring little, if any, fluxing agent. The double coating scheme will also allow for longer brazing times since the thickness of the outer coating can be adjusted to satisfy the needs of specific thermal processing cycles.

Reactive Metal Coatings

The use of reactive metals in brazing has been shown to promote the formation of a thin interlayer between the brazing filler metal and the base metal (Refs. 12–15). This layer promotes adhesion between the faying surfaces of similar and dissimilar materials. Hence, the resulting strength of the braze is dependent upon the nature of the product layer and its thickness. An example is the use of titanium in noble-metal-based brazing filler metals for the joining of metals to ceramic materials. Titanium in the liquid braze metal reacts with the substrate to form a thin reaction layer as shown in Fig. 2. This product layer can be a complex oxide such as $\text{Cu}_2\text{Ti}_4\text{O}$ and $\text{Cu}_3\text{Ti}_3\text{O}_2$, or an intermetallic compound, depending whether the base material is an oxide ceramic or a metal. Certain types of complex oxide (for example, $(\text{Cr}, \text{Mn},$

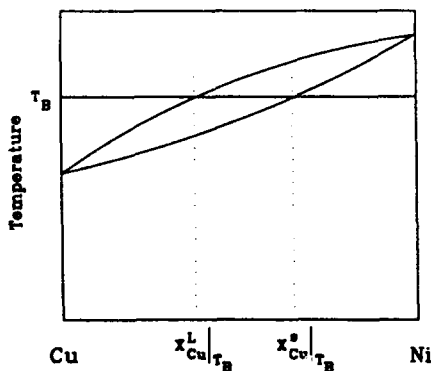


Fig. 3—An isomorphous copper-nickel binary phase diagram showing the solidus and liquidus compositions at the brazing temperature, T_B .

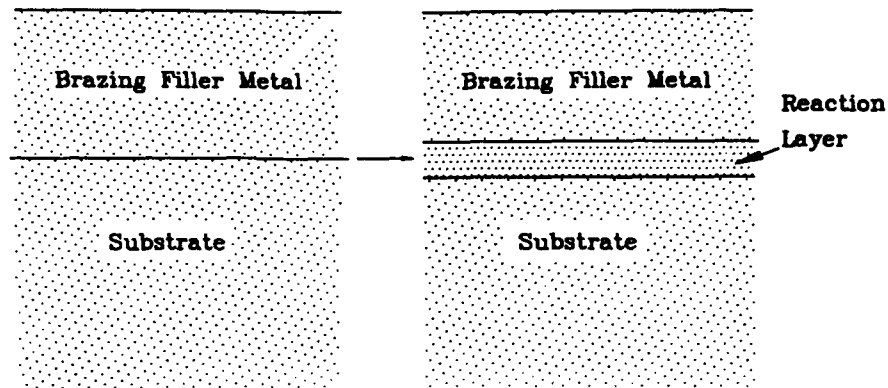


Fig. 2—Schematic drawing showing the formation of a reaction layer between the substrate and brazing filler metal.

$\text{Mg})\text{O} \cdot (\text{Cr}, \text{Mn}, \text{Al})_2\text{O}_3$ spinel) also promote adhesion between metal and oxides as observed in the case of poor slag detachability in stainless steel welding (Ref. 16). The characterization and understanding of the crystal structure and microstructure of the product layers must be carried out so that adequate process control can be achieved.

The thickness of this layer will depend on the reaction kinetics, which is a function of the reactive metal content, diffusion of species through the product layer, brazing time and temperature. Braze joints with inadequate product layer thickness, the result of improper brazing, may not meet the mechanical requirements specified for the joint. Hence, the use of reactive elements as brazing filler metal is a mass transport-based technology that must be investigated and understood.

Coatings for Dissolution-Solidification

Some coatings are deposited for the purpose of dissolution and solidification. In contrast to the passive barrier coatings, these dissolution-solidification coatings are considered active because of their contribution to the braze metal composition and its thickness. A good example is the transient liquid phase (TLP) bonding. TLP bonding is a diffusion brazing process that combines the features of both brazing and diffusion welding (Refs. 7–9). It uses as filler metal a thin interlayer or brazing filler metal of specific composition and melting temperature. At the bonding temperature, the interlayer may melt or a liquid may form by alloying between the interlayer metal and the base metal. The liquid, by capillary action, fills the joint clearance and contributes to the elimination of voids at the braze interface. While the joint members are held at the bonding temperature, diffusion of alloying elements occurs between the liquid and base metal. Isothermal solidification of the joint results because of the solute composition change in the braze. Maintaining the joint at the bonding temperature after solidification

will promote further homogenization of the chemical composition and microstructure. Solid-state diffusion of elements away from the interfacial region reduces the initially large chemical composition gradient, avoiding the formation of intermetallics at the braze. An element of high mobility, both in the liquid and solidified braze metal, will decrease the time for completion of the TLP process.

As an example, consider the brazing of nickel (or a cupronickel alloy) with a pure copper filler metal of half-thickness, W_0 . It can be seen in the phase diagram (Fig. 3) that when the temperature of the joint is raised to the brazing temperature T_B (T_B being greater than the melting point of copper), the copper melts and the solid nickel interface is enriched with copper, $x_{\text{Cu}}^S|_{T_B}$, which lowers its liquidus temperature to T_B (quasi-equilibration). Mass transfer of copper from the liquid phase proceeds to dissolve the nickel base metal and simultaneously enrich the liquid phase with nickel. This process continues until the liquid interphase composition, $x_{\text{Cu}}^L|_{T_B}$, becomes uniform throughout the liquid. Now, solid-state diffusion of nickel from the base metal will enrich the solid interphase region resulting in concomitant solidification (at a much slower rate than the previous base metal dissolution) under isothermal conditions. The liquid zone will eventually resolidify, and its composition will later become uniform, provided sufficient time is allowed for the solid-state diffusion process to occur. The events described above are depicted in Fig. 4.

Conventional transient liquid phase bonding is mostly applied to binary alloy systems which show some intermediate, low-temperature reactions such as eutectic transformation. However, by using an interlayer of adequate thickness that wets the base metal or barrier coating, alloy systems currently not considered for TLP bonding can also be joined by this method. Depending on the rate that the liquid braze dissolves the coating, the proper thickness of a suitable coating and the op-

timal brazing temperature can be determined, (Refs. 10-11).

An analytical model of the TLP bonding process with coating is developed and presented in a later section of this paper. The proposed approach can provide the basis for the selection of braze and coating materials and processing conditions.

Mathematical Modeling of Brazing Processes

It has been shown in the previous sections that with careful process control, coatings can be used effectively to braze difficult-to-join materials and produce bonds of high integrity. The need for process modeling to optimize joining parameters such as coating thickness, brazing time and temperature is also clear. This section will review the existing mathematical formulation of the mass transport processes involved in the brazing processes that utilize coatings.

Barrier Coatings

When using a double-layered barrier

coating in brazing, the layer closest to the base metal (inner coating) is considered passive, and the outer or overlayer is active. The major function of the inner coating is to isolate the base metal from the brazing filler metal since this may contain chemical elements that are undesirable to the system. The passive coating is generally a high-melting-temperature metal and highly adherent to the base metal. It should exhibit excellent base metal wetting and remain solid throughout the brazing process. On the other hand, the overlayer should promote wetting with the brazing filler metal and dissolve entirely or partly into the braze during brazing. Metal dissolution is well characterized and modeled (Refs. 17-20) with extensive literature available. Therefore, no further mathematical modeling on brazing with a barrier coating will be presented in this paper.

Coatings for Dissolution-Solidification

In the case of a coating for dissolution and solidification, the composition of the coating must be carefully selected to be

compatible with the brazing filler metal. The requirements for a brazing filler metal are illustrated in Fig. 5. The phase diagram is for a binary alloy, but this is not a necessary restriction since ternary brazing filler metals could also be considered. In Fig. 4, C_0^B is the initial brazing filler metal composition and B is the coating material. As B dissolves into the liquid braze metal at T_B , the liquid is continuously consumed to produce a solid of composition C_1^B , the final (new) composition of the solidified braze metal. The solidus of this new material has therefore been raised from T_1 to T_B .

Since brazing filler metals can be treated broadly as binary or ternary eutectic materials, there are specific ranges of braze metal compositions that can be used with a selected coating material. For example, consider the liquidus projection diagram in Fig. 6 where it is assumed that the three-phase triangles are traveling along the liquid projection lines according to a Class I, four-phase eutectic reaction (Ref. 21). Adjacent to each of these liquidus lines is a shaded zone which indicates compositions of potential brazing filler metals to be

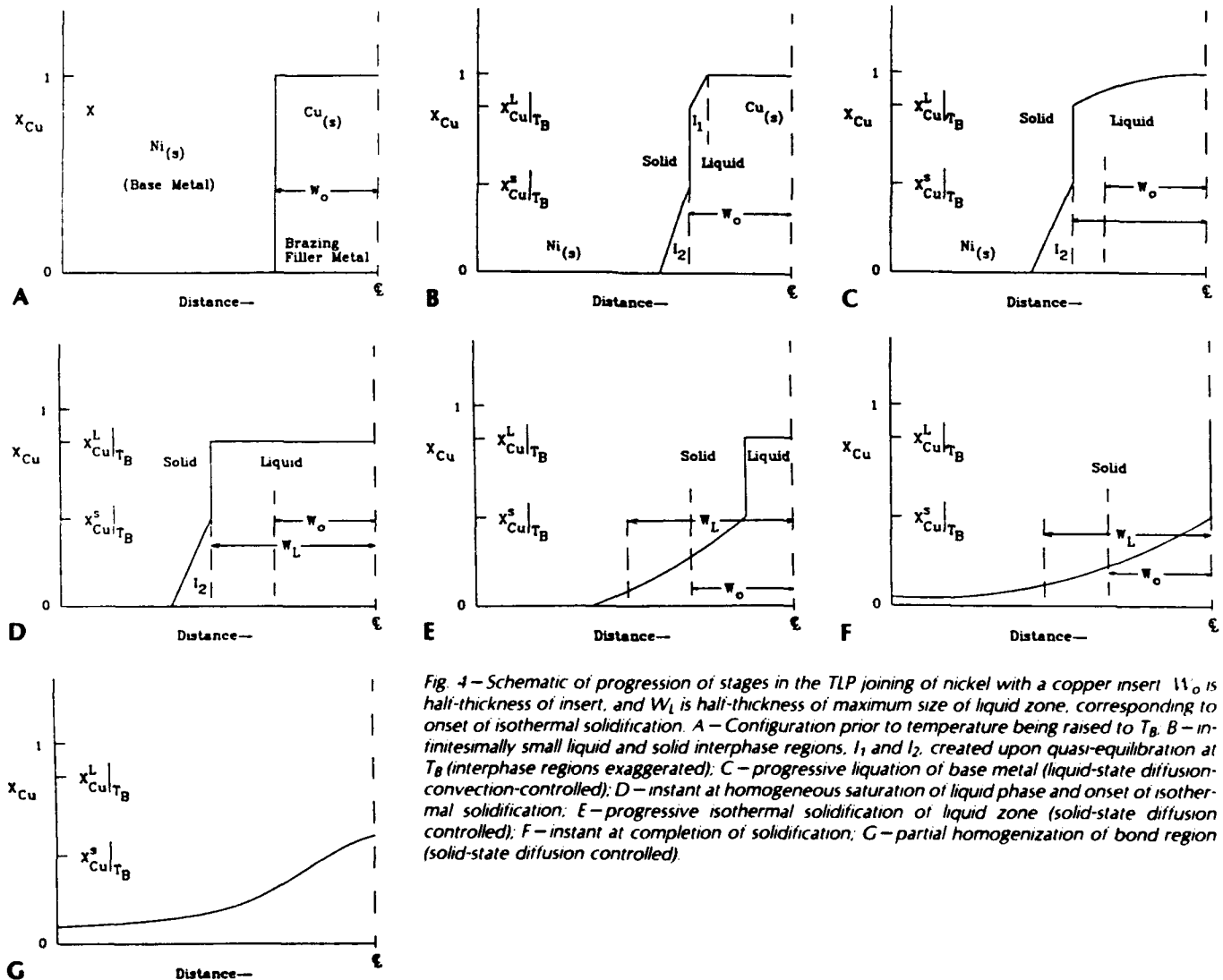


Fig. 4—Schematic of progression of stages in the TLP joining of nickel with a copper insert. w_0 is half-thickness of insert, and w_L is half-thickness of maximum size of liquid zone, corresponding to onset of isothermal solidification. A—Configuration prior to temperature being raised to T_B . B—infinitesimally small liquid and solid interphase regions, l_1 and l_2 , created upon quasi-equilibration at T_B (interphase regions exaggerated). C—progressive liquation of base metal (liquid-state diffusion-convection-controlled); D—instant at homogeneous saturation of liquid phase and onset of isothermal solidification; E—progressive isothermal solidification of liquid zone (solid-state diffusion controlled); F—instant at completion of solidification; G—partial homogenization of bond region (solid-state diffusion controlled).

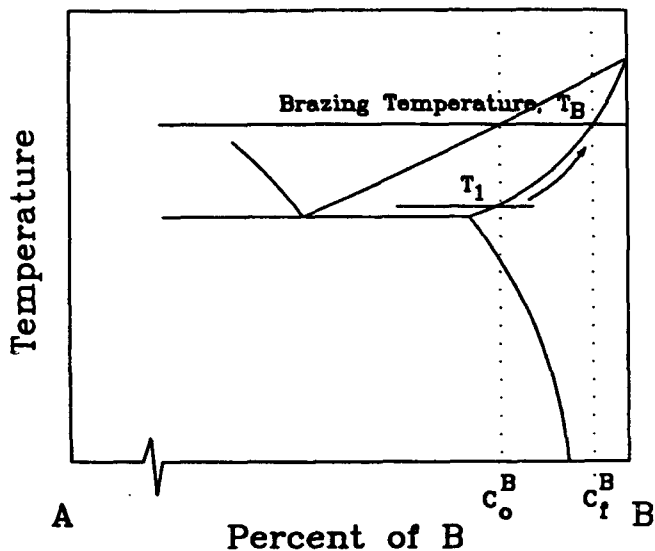


Fig. 5 - Partial binary phase diagram showing the compositions of the initial brazing filler metal, the coating, and the final braze metal composition at solidification.

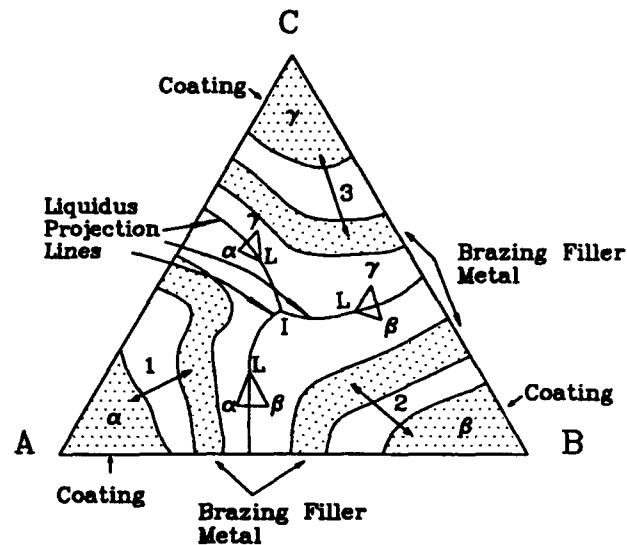


Fig. 6 - Ternary phase diagram indicating the different possible composition ranges of coating and brazing filler metal.

used, with their complementary coating materials. The coating materials are indicated in three separate alloy ranges, each adjacent to a brazing filler metal. The selection of brazing filler metal and complementary coating compositions are made for a given brazing temperature, and the time for which mutual dissolution will result in isothermal solidification. Phase equilibrium behavior illustrated in Fig. 6 can be found for some commonly used silver-iron-silicon filler metals (Ref. 10). Once the coating and brazing filler metals are identified, the resulting bond microstructure and properties will depend on the process temperature and time.

Lesoult (Ref. 22) modeled systematically the process of TLP bonding and divided the process into four stages: 1) dissolution of the interlayer; 2) homogenization of the liquid layer; 3) isothermal solidification; and 4) homogenization of the solidified braze metal. A binary system A-B was

considered, and the equilibrium phase diagram is shown in Fig. 6. The brazing filler metals, with a B-component concentration, C_0^B (an alloy with a limited amount of A), was sandwiched between two substrates of composition, C_0 . The dissolution and solidification stages were treated as a moving boundary problem involving a liquid and a solid, with local equilibrium at the solid-liquid interface. During dissolution, Fick's law was applied:

$$\frac{\partial C^L}{\partial t} = D_L \left(\frac{\partial^2 C^L}{\partial y^2} \right) \quad (1)$$

where C^L is the concentration of the B component in the liquid of an A-B binary system, and y is the coordinate within the liquid region. Using the Error Function solution, the concentration profile that satisfies the above equation is given by:

$$C^L = E + F \operatorname{erf} \left(\frac{y}{\sqrt{4D_L t}} \right) \quad (2)$$

where E and F are constants determined by the specific boundary conditions of the problem. D_L is the liquid diffusion coefficient of element B, and t is time. In addition, the interface displacement, Y_L , was constrained to obey the following square root law:

$$Y_L = K_L \sqrt{4D_L t} \quad (3)$$

K_L was determined to be dependent on the particular alloy system and more specifically, on the slopes of the liquidus and solidus lines of the phase diagram. These lines influence the temperature dependency of the equilibrium concentrations at the liquid-solid phase boundaries.

Due to its complexity, the stage of homogenization of the liquid layer was not modeled (Ref. 22). During solidification, the displacement of the solid-liquid inter-

face, at a particular brazing temperature, results from the solid-state diffusion of B to the saturated solid-liquid interface and can be expressed as:

$$Y_s = K_s \sqrt{4D_s t} \quad (4)$$

and K_s in this equation can be obtained by solving the following implicit equation numerically:

$$K_s \exp(-K_s^2) (1 + \operatorname{erf} K_s) \sqrt{\pi} = \frac{(C^{L\alpha} - C_0)}{(C^{L\alpha} - C^{\alpha})} \quad (5)$$

$C^{L\alpha}$, C^{α} , and C_0 are concentrations defined in Fig. 7, and appear in brackets to distinguish them from the notation used in the next section.

Similar to the dissolution case, K_s is dependent upon the properties of the materials system. Temperature will also influence K_s since the equilibrium concentrations $C^{L\alpha}$ and C^{α} are temperature dependent.

Tuah-Poku, Dollar and Massalski (Ref. 23) investigated, more recently, the mechanisms of TLP bonding and developed further the earlier model by Lesoult (Ref. 22) and Sekerka (Ref. 24). In particular, they determined that the first stage of TLP bonding occurs almost instantaneously, with atomic diffusion taking place mainly in the liquid near the interlayer interface. The second stage is controlled by the diffusion of element B (component of the interlayer) in both the liquid and solid. The widening of the liquid zone was determined to follow a parabolic law.

Modeling of TLP Brazing in This Work

In this study, the progressive stages of TLP bonding were reexamined and a different interpretation was developed. The

Table 1—Values of the Growth Constants G^* and G^{β} for Dissolution of the Base Metal and Brazing Filler Metal for Typical Values of Δ_0 and Δ_1

Δ_0	Δ_1	G^*	G^{β}
10	0.1	1.1513	0.3762
	0.2	0.9800	0.2416
	0.5	0.7502	0.1295
	1.0	0.5853	0.0819
	10.0	0.2095	0.0219
1	0.1	1.0597	1.0597
	0.2	0.8624	0.8624
	0.5	0.6201	0.6201
	1.0	0.4648	0.4648
	10.0	0.1568	0.1568
0.1	0.1	1.0395	1.7003
	0.2	0.8258	1.5372
	0.5	0.5529	1.3187
	1.0	0.3762	1.1513
	10.0	0.0819	0.5853

major difference between this formulation and the models described in the previous section are the first two stages. In this approach, the dissolution of the interlayer and the widening of the liquid zone, as described by the previous models, are considered to occur simultaneously, followed by homogenization and solidification.

Examining the α - β couple shown in Fig. 8 (one-half of a braze joint), it is easy to realize that at high temperatures, atoms A will diffuse toward the β phase, and B atoms will diffuse toward the α phase. With the formation of the initial liquid zone, two solid-liquid interfaces are formed. Though at different rates, these interfaces will advance in opposite directions, consuming the α and β phases, respectively. With time, the brazing filler metal, β , will be totally consumed, to form one single liquid zone.

Stage 1: Formation of the Liquid Zone

Referring to Fig. 8, in Stage 1, once the system is raised to the brazing temperature, T_B , the diffusion of element B in the quiescent liquid can be written as:

$$\frac{\partial C_B^L}{\partial t} = D_L \frac{\partial^2 C_B^L}{\partial y^2}, \quad Y_1^\alpha \geq y \geq -Y_1^\beta \quad (6)$$

with the following initial and boundary conditions:

$$I.C. \quad C_B^L(y, t=0): \text{indeterminate} \quad (7)$$

$$B.C.1 \quad C_B^L(y = -Y_1^\beta, t > 0) = C_B^{\beta L} \quad (8)$$

$$B.C.2 \quad C_B^L(y = -Y_1^\alpha, t > 0) = C_B^{\alpha L} \quad (9)$$

Y_1^α and Y_1^β are the α -liquid braze metal and β -liquid braze metal interfaces, respectively. The compositions representing these boundary conditions can be seen in the binary phase diagram in Fig. 7. It should be noted that this notation is different from that used by Lesoult (Ref. 22), and also by Tuah-Poku, *et al.* (Ref. 23). The superscripts s and l have been used to identify the solid and liquid phases associated with the two solid solutions, α and β . The initial condition is indeterminate because the region where liquid exists is infinitesimally small. In regard to the equilibrium at the liquid-solid (α and β) interfaces, because of the infinitesimally small solid interface regions, they do not contribute to the mass balance in the system. Based upon the overall mass balance of component B in the solid phases (α and β) from which the liquid zone is created, the following equations for motion of the interfaces are determined:

$$\frac{dY_1^\alpha}{dt} = \frac{D_L}{C_B^{\alpha o} - C_B^{\alpha L}} \frac{\partial C_B^L}{\partial y} \Big|_{Y_1^\alpha} \quad (10)$$

and

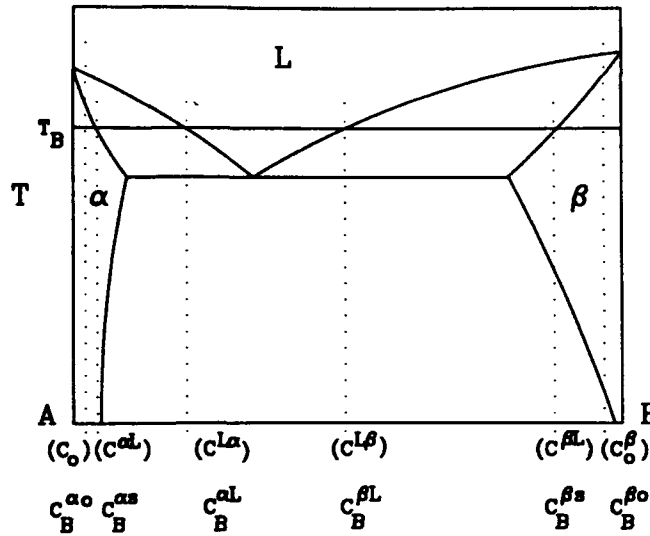


Fig. 7—Binary phase diagram showing the composition of the different phases in TLP brazing.

$$\frac{dY_1^\beta}{dt} = \frac{-D_L}{C_B^{\beta o} - C_B^{\beta L}} \frac{\partial C_B^L}{\partial y} \Big|_{-Y_1^\beta} - Y_1^\beta \quad (11)$$

Implicit in Equations 10 and 11 is that the partial molar volumes of all phases are equal (a restriction imposed on the solution presented here).

The initial conditions, provided that $C_B^{\alpha o}$ is less than $C_B^{\beta s}$ and $C_B^{\beta o}$ is greater than $C_B^{\alpha s}$, are:

$$Y_1^\alpha(t=0) = Y_1^\beta(t=0) = 0 \quad (12)$$

The solution to Equation 6 with the initial and boundary conditions represented by Equations 7-9 is:

$$C_B^L = U_1 + U_2 \operatorname{erf} \left(\frac{y}{2\sqrt{D_L t}} \right) \quad (13)$$

where U_1 and U_2 are constants that can be determined from the boundary conditions. Since the initial condition, as stated by Equation 7, is indeterminate, it does not impose a significant constraint on the behavior of the system as described by Equation 12.

The boundary conditions given by Equations 8 and 9 can be satisfied if:

$$C_B^{\beta L} = U_1 + U_2 \operatorname{erf} \left(\frac{-Y_1^\beta}{2\sqrt{D_L t}} \right) \quad (14)$$

and

$$C_B^{\alpha L} = U_1 + U_2 \operatorname{erf} \left(\frac{-Y_1^\alpha}{2\sqrt{D_L t}} \right) \quad (15)$$

Also, since U_1 and U_2 are constants, as well as the liquidus compositions $C_B^{\beta L}$ and $C_B^{\alpha L}$ (isothermal process), then the position of the solid-liquid interfaces can, therefore, only be described by:

$$Y_1^\alpha = 2G_1^\alpha \sqrt{D_L t} \quad (16)$$

and

$$Y_1^\beta = 2G_1^\beta \sqrt{D_L t} \quad (17)$$

where G_1^α and G_1^β are the dimensionless

growth constants associated with each interface. It should be noted that the initial conditions indicated by Equation 12 are also satisfied by Equations 16 and 17.

Equations 14 and 15 can therefore be rewritten as:

$$C_B^{\beta L} = U_1 - U_2 \operatorname{erf}(G_1^\beta) \quad (18)$$

and

$$C_B^{\alpha L} = U_1 + U_2 \operatorname{erf}(G_1^\alpha) \quad (19)$$

On subtracting Equation 18 from 19 and rearranging, the following equation is obtained to determine U_2 :

$$U_2 = \frac{C_B^{\alpha L} - C_B^{\beta L}}{\operatorname{erf}(G_1^\alpha) + \operatorname{erf}(G_1^\beta)} \quad (20)$$

Equations 16 and 17 can now be used to develop equations from which the growth constants G_1^α and G_1^β may be obtained. Differentiating these equations with respect to time gives:

$$\frac{dY_1^\alpha}{dt} = \frac{G_1^\alpha \sqrt{D_L}}{\sqrt{t}} \quad (21)$$

$$\frac{dY_1^\beta}{dt} = \frac{G_1^\beta \sqrt{D_L}}{\sqrt{t}} \quad (22)$$

Now, differentiating Equation 15 with respect to y , yields:

$$\frac{\partial C_B^L}{\partial y} = U_2 \frac{2}{\sqrt{\pi}} \exp \left(-\frac{y^2}{4D_L t} \right) \frac{1}{2\sqrt{D_L t}} \quad (23)$$

which, when evaluated at $y = Y_1^\alpha$ and $y = -Y_1^\beta$, leads to:

$$\frac{\partial C_B^L}{\partial y} \Big|_{y=Y_1^\alpha} = U_2 \frac{2}{\sqrt{\pi}} \exp(-G_1^{\alpha 2}) \quad (24)$$

$$\frac{1}{2\sqrt{D_L t}}$$

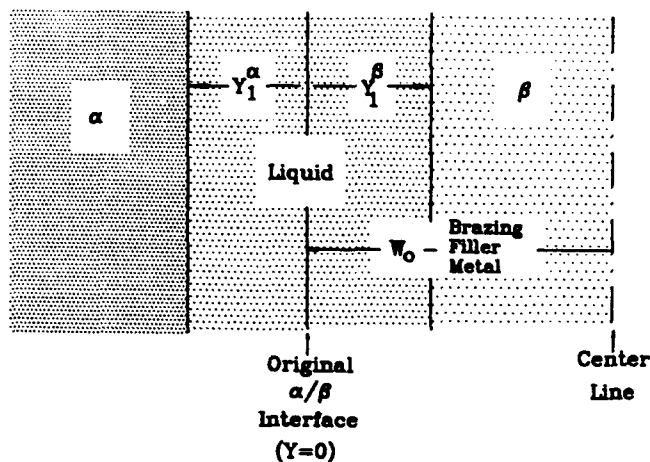


Fig. 8 - Configuration of α -phase base material, liquid region and β -phase brazing filler metal during isothermal liquification of solid phases, at time, t , after system is raised to brazing temperature, T_B .

$$\frac{\partial C_B^I}{\partial y} \Big|_{y=Y_1^{\alpha}} = U_2 \frac{2}{\sqrt{\pi}} \exp(-G_1^{\beta 2}) \quad (25)$$

Substituting Equations 21, 22, 24 and 25 appropriately into Equations 10 and 11, the following equation is obtained when these two recast equations are divided, one by the other:

$$\frac{G_1^{\alpha}}{G_1^{\beta}} = \frac{C_B^{\beta 0} - C_B^{\beta L}}{C_B^{\alpha 0} - C_B^{\alpha L}} \exp(G_1^{\beta 2} - G_1^{\alpha 2}) \quad (26A)$$

Also, when Equation 20 is used to replace U_2 in Equation 24 and this is then substituted into the right-side of Equation 10, while the left side is replaced using Equation 21, the following additional equation is obtained:

$$G_1^{\alpha} = \frac{C_B^{\alpha L} - C_B^{\beta L}}{\text{erf}(G_1^{\beta}) + \text{erf}(G_1^{\alpha})} \frac{1}{\sqrt{\pi}} \exp(-G_1^{\alpha 2}) \quad (27A)$$

Equations 26A and 27A can be rewritten as follows:

$$\Delta_0 G_1^{\beta} \exp(G_1^{\beta 2} - G_1^{\alpha 2}) - G_1^{\alpha} = 0 \quad (26B)$$

$$\Delta_1 G_1^{\alpha} \sqrt{\pi} [\text{erf}(G_1^{\beta}) - \text{erf}(G_1^{\alpha})] - \exp(-G_1^{\alpha 2}) = 0 \quad (27B)$$

where

$$\Delta_0 = \frac{C_B^{\beta 0} - C_B^{\beta L}}{C_B^{\alpha 0} - C_B^{\alpha L}} \quad (28)$$

$$\Delta_1 = \frac{C_B^{\alpha 0} - C_B^{\alpha L}}{C_B^{\alpha 0} - C_B^{\beta L}} \quad (29)$$

and it is noted that Δ_0 and Δ_1 are both positive quantities. These simultaneous equations, 26B and 27B, can be solved numerically to obtain the growth constants G_1^{α} and G_1^{β} once Δ_0 and Δ_1 have been defined. Values of the growth constants are tabulated in Table 1. It should be noted that the physical behavior associated with the system is properly manifested by the values of the growth constants. For example, when Δ_0 is unity, the growth constants are identical in magnitude. This is to be expected, since the enrichment of the liquid B provided via the β -phase filler metal is exactly compensated by the dilution due to the same volume of the α -phase base metal being consumed. Furthermore, when Δ_0 is greater than unity the growth constant G_1^{α} is greater than G_1^{β} , as a result of a larger volume of the α -phase being required to compensate for the β -phase as the transient liquid is formed. The situation is reversed when Δ_0 is fractional.

The formulation and solution presented here is significantly different from that presented by Tuah-Poku, Dollar and Masalski (Ref. 23) and attributed to Lesoult (Ref. 22), where only the growth constant for the liquid braze metal zone was considered.

The time at which a brazing filler metal of initial half-width, W_0 , is consumed is given by:

$$t_1 = \frac{W_0^2}{4 G_1^{\beta 2} D_L} \quad (30)$$

Also, the half-width of the liquid zone at this instant (prior to homogenization of

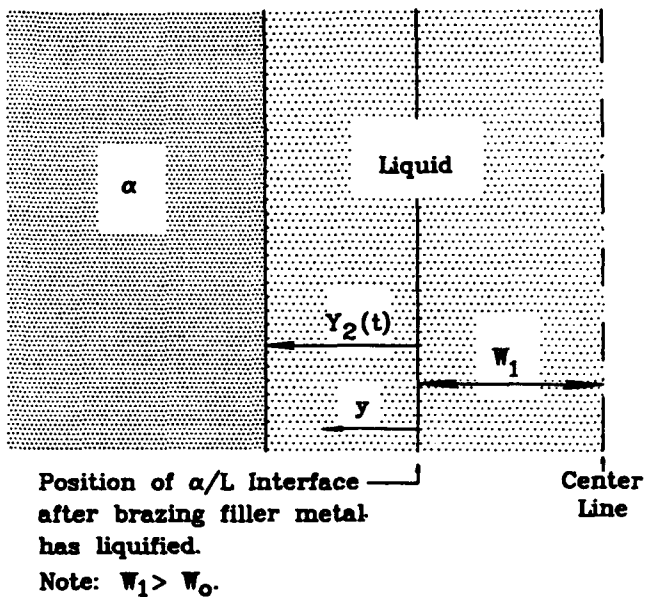


Fig. 9 - Configuration of system, at time, t , after brazing filler metal, of half-thickness, W_0 , has liquified and liquid region becomes homogenized due to further dissolution of α -phase base metal.

the liquid), W_L , is given by:

$$W_L = W_0 + 2 G_1^{\alpha} \sqrt{D_L t_1} \quad (31)$$

Therefore, given the brazing temperature, metal compositions and interlayer thickness, then the time for interlayer dissolution, t_1 , and the liquid zone half-width developed, W_L , can be calculated.

Stage 2: Homogenization of the Liquid Zone

During homogenization, Stage 2, the diffusion of B in the liquid phase is again described by:

$$\frac{\partial C_B^L}{\partial t} = D_L \frac{\partial^2 C_B^L}{\partial y^2}, \quad Y_2(t) > y > -W_1 \quad (32)$$

where now, only one moving boundary is present. The configuration at time, t , after this stage has started, is shown in Fig. 9. The initial condition is:

$$C_B^L(0 > y \geq -W_1, t = 0) = F(y) \quad (33)$$

where:

$$F(y) = C_B^{\beta L} + (C_B^{\alpha L} - C_B^{\beta L}) \left[\text{erf}(G_1^{\beta}) + \text{erf} \left(G_1^{\alpha} + \frac{y}{\sqrt{2 D_L t_1}} \right) \right] \text{erf}(\Delta_0 G_1^{\beta}) \quad (34)$$

$$W_1 = W_0 + 2 G_1^{\alpha} \sqrt{D_L t_1} = 2 \sqrt{D_L t_1} (G_1^{\alpha} + G_1^{\beta}) \quad (35)$$

since W_0 can be replaced using Equation 30.

The initial condition, Equation 34, describes the concentration profile in the liquid at the end of Stage 1. The boundary conditions are:

$$C_B^L [y = Y_2(t), t > 0] = C_B^{\alpha L} \quad (36)$$

$$\frac{\partial C_B^L}{\partial y} \Big|_{y = -w_{11}} = 0 \quad (37)$$

$$\frac{dY_2}{dt} = \frac{-D_L \frac{\partial C_B^L}{\partial y} \Big|_{Y_2(t)}}{(C_B^{\alpha L} - C_B^{\alpha O})} \quad (38)$$

with initial condition,

$$Y_2(t = 0) = 0 \quad (39)$$

A solution to Equation 32, with the initial and boundary conditions, and the moving boundary condition, most likely, will have to be determined numerically. While it is recognized that the time to complete Stages 1 and 2 of the process is small compared to that for Stage 3, nevertheless the maximum half-width, W_{max} , attained by the liquid zone is an inherent requirement for determining the time, t_3 , for the isothermal solidification of the induced liquid zone.

The maximum half-width of the liquid zone can be calculated from mass balance constraints. For conservation of the component B:

$$W_{max} C_B^{\alpha L} = W_0 C_B^{\beta O} + (W_{max} - W_0) C_B^{\alpha O} \quad (40)$$

or

$$W_{max} = \frac{C_B^{\beta O} - C_B^{\alpha O}}{C_B^{\alpha L} - C_B^{\alpha O}} W_0 \quad (41)$$

Stage 3: Isothermal Solidification

Stage 3 is the isothermal solidification of the induced liquid zone. The configuration at some instant, t , after solidification has started is shown in Fig. 10. Diffusion of B in the solid α -phase can be described by the following equation:

$$\frac{\partial C_B^{\alpha}}{\partial t} = D_s \frac{\partial^2 C_B^{\alpha}}{\partial y^2}; \infty \geq y \geq -Y_3 \quad (42)$$

The initial and boundary conditions are:

$$I.C. C_B^{\alpha}(y, t = 0) = C_B^{\alpha O} \quad (43)$$

$$B.C.1 C_B^{\alpha}(y = -Y_3, t > 0) = C_B^{\alpha S} \quad (44)$$

$$B.C.2 C_B^{\alpha}(y \rightarrow \infty, t) = C_B^{\alpha O} \quad (45)$$

The equation for motion of interface is:

$$\frac{dY_3}{dt} = \frac{-D_s}{C_B^{\alpha L} - C_B^{\alpha S}} \frac{\partial C_B^{\alpha}}{\partial y} \Big|_{y = -Y_3} \quad (46)$$

with initial condition:

$$Y_3(t = 0) = 0 \quad (47)$$

Note that $C_B^{\alpha S} < C_B^{\alpha L}$ and consequently component B diffuses into the solid base metal, thereby depleting the liquid of B and leading to its isothermal solidification. Equation 42 is satisfied by:

$$C_B^{\alpha} = U_1 + U_2 \operatorname{erf} \left(\frac{y}{2\sqrt{D_s t}} \right) \quad (48)$$

and the initial condition (Equation 43) and boundary condition (Equation 45) require that:

$$C_B^{\alpha O} = U_1 + U_2 \quad (49)$$

Also, the boundary condition given by Equation 44 can only be satisfied if:

$$C_B^{\alpha S} = U_1 + U_2 \operatorname{erf} \left(\frac{-Y_3}{2\sqrt{D_s t}} \right) \quad (50)$$

Furthermore, since U_1 and U_2 are constants, as well as the solidus composition, $C_B^{\alpha S}$ in the α phase during isothermal solidification, therefore the argument of the error function must also be a constant; consequently the position of the solid-liquid interface can only be described by:

$$Y_3 = 2 G_3 \sqrt{D_s t} \quad (51)$$

where G_3 is a dimensionless growth con-

stant; and the initial condition as described by Equation 47 is satisfied by Equation 51. Consequently, since $\operatorname{erf}(-x) = -\operatorname{erf}(x)$, Equation 50 can be rewritten as:

$$C_B^{\alpha S} = U_1 - U_2 \operatorname{erf}(G_3) \quad (52)$$

Also, a general expression for the concentration gradient is obtained by differentiating Equation 48, with respect to y :

$$\frac{\partial C_B^{\alpha}}{\partial y} = U_2 \frac{2}{\sqrt{\pi}} \exp \left(\frac{-y^2}{4D_s t} \right) \frac{1}{2\sqrt{D_s t}} \quad (53)$$

Subtracting Equation 52 from Equation 49 gives the following expression for U_2 :

$$U_2 = \frac{(C_B^{\alpha O} - C_B^{\alpha S})}{1 + \operatorname{erf}(G_3)} \quad (54)$$

Finally, Equation 51 can be differentiated to obtain the velocity of the interface, viz:

$$\frac{dY_3}{dt} = G_3 \frac{\sqrt{D_s}}{\sqrt{t}} \quad (55)$$

Now, Equation 54 can be used to replace U_2 in Equation 53, and this expression together with Equation 55 to replace the respective terms in Equation 46, the following implicit equation for G_3 is obtained:

$$G_3 [1 + \operatorname{erf}(G_3)] \sqrt{\pi} \exp(-G_3^2) = \frac{C_B^{\alpha S} - C_B^{\alpha O}}{C_B^{\alpha L} - C_B^{\alpha S}} \quad (56)$$

which is identical to the equation attributed to Lesoult according to Tuah-Poku, Dollar and Massalski (Ref. 23).

If the maximum half-width of the induced liquid zone is W_{max} , then the elapsed time to complete the isothermal solidification is given by Equation 57, below:

$$t_3 = \frac{W_{max}^2}{4 G_3^2 D_s} \quad (57)$$

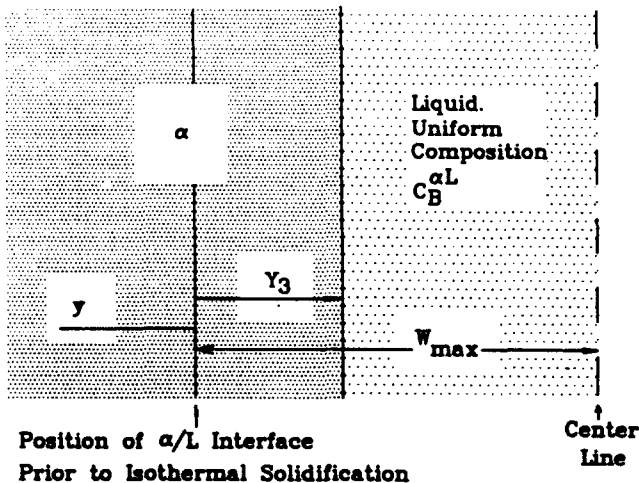


Fig. 10—Configuration of system, at time, t , after liquid region has homogenized and solidification has started due to solid-state diffusion of B, from liquid region into α -phase base metal.

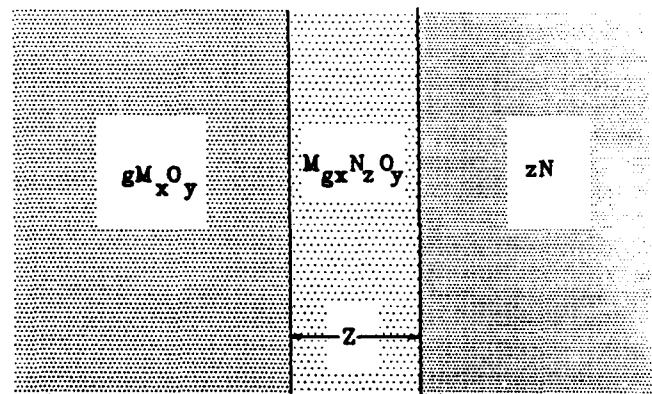


Fig. 11—Schematic diagram showing the formation of a complex oxide layer in the joining of metals to ceramic materials.

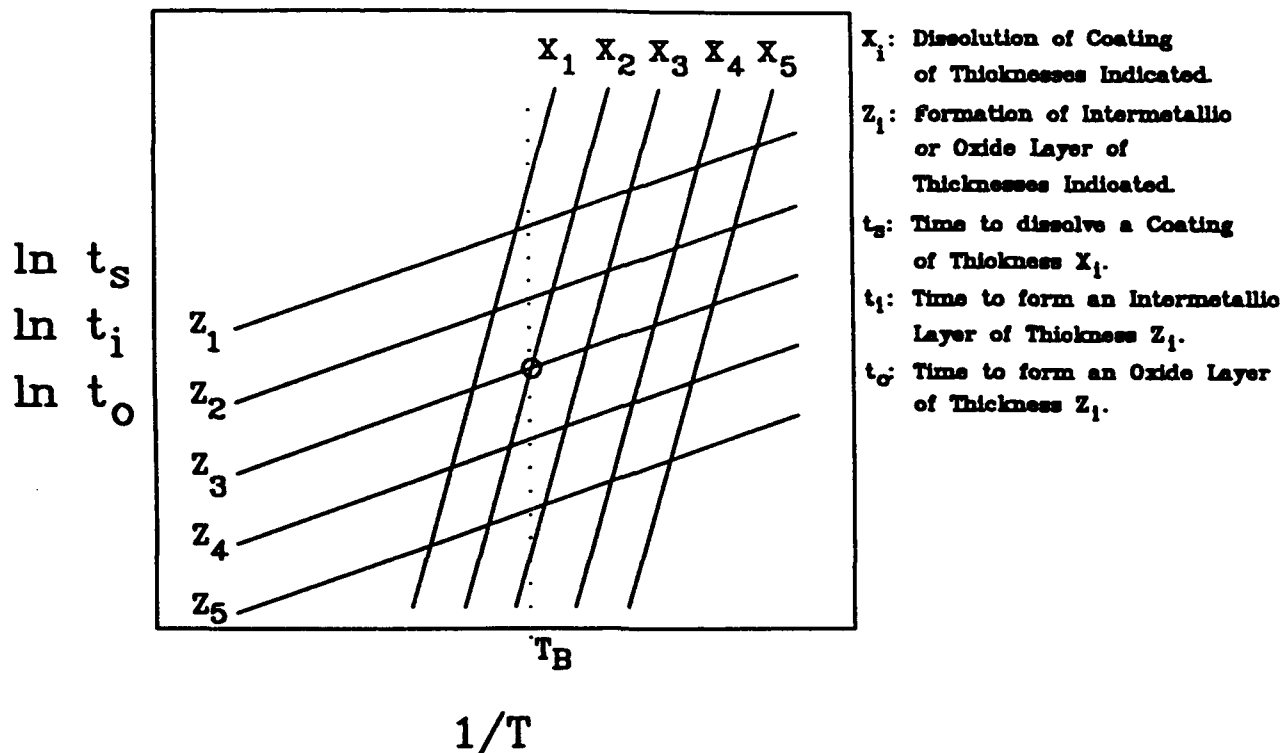


Fig. 12—Conceptual brazing process control as a function of the time of dissolution of the coating, the time of oxide and intermetallic formation, and the brazing temperature. For an acceptable oxide layer thickness, Z_3 , and maximum tolerable coating dissolution thickness, X_2 , the brazing temperature should be T_B as indicated on the diagram.

where G is determined by solving Equation 56 numerically, for a given C^{aq} , C^{g} , and C^{m} .

Modeling of Reactive Metal Brazing in This Work

There are numerous possible rate-controlling steps in this process. If the brazing filler metal has a very dilute reactive metal addition, the rate-controlling process may be the transport of the reactive element in the liquid braze to the reaction interface. One possible mass transport controlled process would be liquid diffusion where the reactive metal is consumed at the interface in product formation. However, a more realistic situation is where the product film or reaction layer is adhesive to and protective of the base metal, then solid-state diffusion across the interlayer will be the controlling process. A simple mathematical description for this moving boundary problem is given below. It is assumed that the chemical potentials are invariant at both interfaces and the layer thickness increases with time.

Depending on the base material to be joined—ceramic oxide or metal—the reaction product will be specific to that system. In metal-to-ceramic joining, it is most likely that an oxide layer will form. In the case of a metal, the equilibrium phase diagram determines whether a solid solution or intermetallic phase will form. The case of oxide formation is chosen to illustrate the procedure of determining the

processing time, temperature and thickness of the coating to achieve an acceptable brazement. From the boundary condition described above, a parabolic time dependent growth of the product layer results. Figure 11 illustrates this oxide formation case.

Given the following reaction of oxidation:



and rate expression for growth of the product phase is given by:

$$Z^2 = 2K't \quad (59)$$

with:

$$K' = K_0 \exp\left(\frac{-Q}{RT}\right) \quad (60)$$

where K' is the rate coefficient, K_0 is the preexponential factor, Z is the thickness of the product layer, and RT has the usual significance. The time to form a reaction layer of thickness Z can be determined by solving Equations 59 and 60.

$$\ln t_0 = \ln\left(\frac{Z^2}{2K_0}\right) - \frac{Q}{RT} \quad (61)$$

where Q is the activation energy of the process and R is the universal gas constant. In the case of intermetallic formation, a similar equation will result.

Equation 61 is an important analytical tool in controlling reactive metal brazing. Too thin a reaction layer may not result in a sound braze while too thick a layer will

result in excessive oxide/intermetallic compound growth and poor mechanical properties. Therefore, an optimal reaction layer thickness can be controlled by regulating process temperature and time.

Conceptual Application of Modeling to Process Control

In brazing, temperature, time and filler metal are some of the more important process parameters to be controlled and optimized. When a coating is introduced between the base material and brazing filler metal, active dissolution may occur at the interface between the brazing filler metal and the coating material. At the same time, chemical reactions may also occur at the base metal-coating interface. Since the kinetics of the two processes are in general not the same, it is essential to determine a set of optimal time and temperature for these simultaneous processes. It is obvious that the dissolution process should not consume the entire layer of coating, nor the intermetallic formation create an excessively thick product layer. To match the effects of interlayer dissolution and subsequent consumption of the coating with the formation of the oxide (or intermetallic) layer, the time for dissolution of selected coating thicknesses, X_1, X_2, \dots, X_5 , can be plotted as a function of temperature. Increasing the temperature decreases the time of dissolution. The time of oxide (or intermetallic) formation and growth to selected

thicknesses, Z_1, Z_2, \dots, Z_5 , can also be plotted likewise on the same figure. The two sets of parallel lines can be observed in Fig. 12. Since the thermally activated mechanisms of the two processes are different, the slope of the second set of lines is also different from that of the first set. For the oxide (or intermetallic) formation lines, the slope, associated with the parabolic growth law, is equal to Q/R ; where Q is the activation energy of the transport mechanism of the growth process. Given a certain constraint of thickness of the oxide (or intermetallic) layer, then, the thickness of a coating that will be completely consumed by dissolution as well as the time and corresponding temperature of brazing can be determined from Fig. 12.

To illustrate the concept, consider the case where the oxide product layer must be limited to a thickness, Z_3 and an acceptable brazing time can be achieved at a temperature of T_1 , the diagram indicates that the coating will be dissolved and be penetrated to a distance X_2 by the transient liquid phase bonding process. Consequently, the coating thickness selected must be larger than X_2 .

In Fig. 12, the slope of the X lines (dissolution of the coating layer) is assumed to be greater than that of the oxide or intermetallic formation, Z lines. In the case that the slopes of both are changed, Z lines with greater slope than X lines, the interpretation procedure can still be followed.

Summary

It is apparent that coating technology, in particular the type for dissolution and solidification, can be applied in brazing. Multiple-layered coatings of different compositions can be tailored for difficult-to-join materials. With the mathematical models developed in this work, it is possible to begin addressing the design issues of brazing with custom coatings: types of coating, thickness of each layer, brazing time and temperature. Depending on the degree of dissolution of the coating and brazing filler metal, and the type of products that form at the base metal-coating and coating-brazing filler metal interfaces, the approach developed in this work will provide the basis for selecting brazing time, temperature and thickness of the coating for successful brazing.

Acknowledgment

The authors acknowledge and appreciate the support of the Office of Naval Research.

References

1. Funamoto, T., Kokura, S., Kato, M., Shida, T., and Oshima, K. 1985. A study on formation of alloyed layer of low melting temperature on bonding surface of IN 738 LC with sputtering. *Quarterly Journal of the Japan Welding Society*, 3(4):207-212.

2. Kato, M., Funamoto, T., and Wachi, H., Matsuzaka, T., Shida, T., and Kokura, S. 1987. A study of alloyed layer of low melting temperature on bonding surface of IN 738 LC with boron pack cementation. *Quarterly Journal of the Japan Welding Society*, 5(3):84-87.

3. Funamoto, T., Kato, M., Wachi, H., Kokura, S., Shida, T., and Matsuzaka, T. 1987. Diffusion weldability of IN 738 LC with alloyed layer on bonding surface by boron pack cementation. *Quarterly Journal of the Japan Welding Society*, 5(3):87-93.

4. Klein Wassink, R.J. 1984. Coated materials. *Soldering in Electronics*, 177-180, Electrochemical Publications Limited.

5. AWS. 1976. *Brazing Manual*, American Welding Society, Miami, Fla.

6. Bratton, S. C., and Clarke, M. 1959. Detection of zinc diffusion into tin coatings on brass. *Trans. Inst. Metal Finish.*, 36:230-232.

7. AWS. 1980. Diffusion welding and brazing. *Welding Handbook-Vol. 3*, 7th Edition, pp. 311-336, American Welding Society Miami, Fla.

8. Paulonis, D. F., Duvall, D. S., and Owczarski, W. A. 1972. *U.S. Patent 3,678,570*.

9. Duvall, D. S., Owczarski, W. A., and Paulonis, D. F. 1974. T.I.P.: a new method for joining heat-resisting alloy. *Welding Journal*, 53(4):203-214.

10. Lammel, J. M., and Chalmers, B. 1959. The isothermal transfer from solid to liquid in metal systems. *Trans. TMS-AIME*, 215:499-508.

11. Bredtz, N., and Schwartzbart, H. 1959. Metallurgy of bonding in brazed joints. *Welding Journal*, 38:305-s to 314-s.

12. Tressler, R. E., Moore, T. L., and Crane, R. L. 1973. Reactivity and interface characteristics of titanium-alumina composites. *Journal of Materials Science*, 8:151-161.

13. Nicholas, M. G., Valentine, T. M., and Waite, M. I. 1980. The wetting of alumina by copper alloyed with titanium and other elements. *Journal of Materials Science*, 15:2197-2206.

14. Nicholas, M. G. 1986. Active metal brazing. *Trans. and Journal of the British Ceramic Society*, 85:144-146.

15. Nicholas, M. G., and Mortimer, D. A. 1985. Ceramic/metal joining for structural applications. *Materials Science and Technology*, 1:657-665.

16. Pincus, A. G. 1954. *Ceramic Age* 63:16,20, 30-33.

17. Tanzilli, R. A., and Heckel, R. W., 1968. Numerical solutions to the finite, diffusion-controlled, two phase, moving-interface problem (with planar, cylindrical, and spherical interfaces). *Trans. TMS-AIME*, 242:2313-2321.

18. Ohno, R. 1986. Rates of dissolution of solid iron, cobalt, nickel, and silicon in liquid copper and diffusion rate of iron from liquid Cu-Fe alloy into liquid copper. *Met. Trans. B*, 17:291-305.

19. Ishida, T. 1986. Rate of dissolution of solid nickel in liquid tin under static conditions. *Met. Trans. B*, 17:281-289.

20. Nakao, Y., Nishimoto, K., Shinozaki, K., Yun, K. C., and Hori, Y. Dissolution phenomenon of base metal into liquid insert metal. *Quarterly Journal of the Japan Welding Society*, 6(4):519-526.

21. Rhines, F. N. 1956. *Phase Diagrams in Metallurgy - Their Development and Application*, McGraw Hill Publishing Co.

22. Lesoult, G. 1976. Modeling of the TLP Bonding Process I. Report of the Center for the Joining of Materials, Carnegie-Mellon University.

23. Tuah-Poku, I., Dollars, M., and Massalski, T. B. 1988. A study of the transient liquid phase bonding process applied to a Ag/Cu/Ag sandwich joint. *Met. Trans. A*, 19:675-686.

24. Sekerka, R. F. 1980. On the modeling of TLP bonding. *Proc. of Physical Metallurgy of Metals Joining Conf.*, TMS-AIME, St. Louis, Mo.

Appendix

C_B^l	Concentration of B, in the (binary) liquid phase.
C_B^s	Concentration of B, in the α -phase (base metal) solid solution.
$C_B^{\alpha 0}$	Initial (uniform) concentration of B in the α -phase.
$C_B^{\beta 0}$	Initial (uniform) concentration of B in the β -phase.
C_B^s	Solidus concentration of B in the saturated α solid solution, at the isothermal solidification (brazing) temperature, T_B .
$C_B^{\beta s}$	Solidus concentration of B in the saturated β solid solution, at the isothermal solidification (brazing) temperature, T_B .
$C_B^{\alpha l}$	Liquidus concentration of B which is in equilibrium with the saturated α solid solution, of composition C_B^s .
$C_B^{\beta l}$	Liquidus concentration of B which is in equilibrium with the saturated β solid solution, of composition C_B^s .
G_1	Growth constant for liquification of base metal, during Stage 1.
G_1^f	Growth constant for liquification of brazing filler metal, during Stage 1.
G_2	Growth constant for liquification of base metal, during homogenization of liquid region - Stage 2.
G_3	Growth constant for solidification of liquid region - Stage 3.
Δ_0	$\frac{C_B^{\beta 0} - C_B^{\beta l}}{C_B^{\alpha l} - C_B^{\alpha 0}}$
Δ_1	$\frac{C_B^{\alpha 0} - C_B^{\alpha l}}{C_B^{\beta l} - C_B^{\beta s}}$

A Thermodynamic Criterion to Predict Wettability at Metal-Alumina Interfaces

P.R. CHIDAMBARAM, G.R. EDWARDS, and D.L. OLSON

Metals are known to wet ceramics by chemical bond formation. Existing theories, using reaction thermodynamics, can predict the relative wetting trends in wetting systems but fail to distinguish between the wetting and nonwetting systems. Wetting is considered as a surface phenomenon, and the spontaneity of wetting is controlled by ΔG_w , a thermodynamic term defined here as the Gibbs free energy of wetting. A model that treats wetting as a reaction between the surface phase of the ceramic and the molten metal is presented to calculate ΔG_w . The model is used to predict wetting tendencies of various molten metals on α -alumina surfaces. The predictions are compared with previously published results, as well as with the experimental results of this study. Experimental wettability parameters were measured using a capillary rise apparatus. Measurements were made for various metals wetting an aluminum-oxide surface. Based on this model, a thermodynamic wetting map that delineates wetting and nonwetting regimes is drawn. A map of this nature can be used advantageously in ceramic joining and metal-matrix composites applications.

I. INTRODUCTION

PREDICTING wettability at the metal-ceramic interface is becoming increasingly important with the advent of modern composite materials. An appropriate choice of metal-ceramic pairs is critical in many applications, such as joining metals to ceramics, joining ceramics to ceramics with a metallic interlayer, microdesigning of metal/ceramic composites, electronic packaging material design, and designing refractories in extractive metallurgy. Yet, there are no models that successfully predict whether or not a particular metal or alloy will wet a given ceramic substrate.

Based on the nature of attractive forces existing across the interface, wetting can be classified into two broad categories: (a) physical wetting, where the reversible physical forces, such as the van der Waals and dispersion forces, provide the attractive energy required to wet the surface, and (b) chemical wetting, where a reaction occurs between the mating surfaces and the resultant chemical bonds are responsible for wetting. Since metals are known to wet ceramics essentially by chemical bond formation,⁽¹⁾ physical wetting is not discussed in this article.

Since wetting here is synonymous with reaction, chemical thermodynamics is an obvious analytical approach which can be used to model the metal-ceramic system. As can be seen in Section II, bulk thermodynamics can predict relative trends in such wetting systems, but this approach cannot be used to predict whether a given system is wetting or nonwetting.

A thermodynamic criterion that has been developed by treating wetting as a surface phenomenon is presented here. The reaction that is required for chemical wetting

is between the surface phase of the ceramic and the molten metal. The free-energy change for this reaction, ΔG_w , can be used to predict wetting tendencies. A negative ΔG_w implies a wetting system. It should be emphasized that this approach is appropriate only to predict wetting at the initiation of wetting and does not address the complex interfacial structure observed at equilibrium by other researchers.^(2,3)

Capillary rise experiments using alumina tubes were performed as a part of this study to verify the model predictions. Consistent contact angle measurements were made for various noble metals on α -alumina surfaces. The results obtained are discussed with the help of a wettability map. Apart from identifying the wetting and nonwetting systems, these maps are useful in predicting the stability of the interface.

II. CONVENTIONAL THERMODYNAMIC APPROACH

A simplistic approach to model the system using bulk thermodynamics would be to consider that wetting is possible whenever the ΔG_r for the reaction at the interface is negative. For example, when alumina ceramic is in contact with a molten metal M, the following reaction can occur:



The Gibbs free-energy change ΔG_r for this reaction can be calculated using a simple relation shown in Eq. [2]:

$$\Delta G_r = 3 \Delta G_{\text{M}_x\text{O}}^\circ - \Delta G_{\text{Al}_2\text{O}_3}^\circ + RT \ln \frac{a_{\text{Al}}^2}{a_{\text{M}}^{3x}} \quad [2]$$

The free-energy change ΔG_r represents the energy released or required when aluminum-oxide is reduced by the metal, M. A negative ΔG_r implies a spontaneous reaction and, hence, wetting. The reaction proceeds until equilibrium is reached ($\Delta G_r = 0$). In order to predict the sign and magnitude of ΔG_r , at the start of the reaction, the activity values a_{Al} and a_{M} must be determined. The

P.R. CHIDAMBARAM, Graduate Research Assistant, G.R. EDWARDS, Director, and D.L. OLSON, Professor, are with the Department of Metallurgical and Materials Engineering, Center for Welding and Joining Research, Colorado School of Mines, Golden, CO 80401.

Manuscript submitted February 18, 1991.

activity of the metal a_M in its pure state is unity; if present in the alloy form, a_M can be calculated using the following equation:

$$a_M = \Gamma X_M \quad [3]$$

where Γ is the activity coefficient of metal in the alloy and X_M is the mole fraction of the metal in the melt. The activity coefficient, Γ , depends on the nature of interaction between the metal M and the solute. There are established theoretical models that can be used to calculate Γ ; these calculations have already been done for most binary alloys^[4] and are tabulated in Table I.

The activity of aluminum a_{Al} in the metal or alloy is also calculated using Eq. [3]; however, an appropriate value for X_{Al} needs to be assumed. The value of X_{Al} is zero when no reaction has occurred. In the present calculations, it has been assumed that wetting occurs, if sufficient driving force ($\Delta G_r < 0$) exists after the fractional dissolution of aluminum in the vicinity of the interface attains 1 pct. Therefore, an X_{Al} value of 0.01 is used in the calculations. The standard free energy of compound formation ΔG° at the temperature of interest of the oxide is obtained easily from the thermodynamic handbook tabulations.^[5] The ΔG_r calculated from these values are shown in Table I.

Contact angle θ is an accepted measure of wettability at the metal-ceramic interface.^[6] The general case of a liquid metal in contact with the ceramic is shown in Figure 1, where a balance of surface tension forces results in the familiar Young equation:

$$\gamma^v \cos \theta = \gamma^s - \gamma^l \quad [4]$$

where γ^s , γ^v , and γ^l are the corresponding surface energies of solid/vapor, liquid/vapor, and solid/liquid interfaces, respectively. A system is considered wetting when the wettability parameter $\gamma^v \cos \theta$ is greater than zero (Figure 1(a)). Therefore, the wettability parameter can be used to verify the thermodynamic predictions.

The surface tension balance presented above is valid only for nonreacting interfaces. According to Pask,^[7] when a reaction occurs at the interface, the free-energy change per unit area per unit time also enhances wetting; in this case, the Young equation should be corrected for this additional driving force. In the present analysis, the wettability parameter is not used to evaluate the degree of wetting in the wetting systems precisely for this reason. However, the contact angle values reported in the literature are presented to establish the fact that wetting has

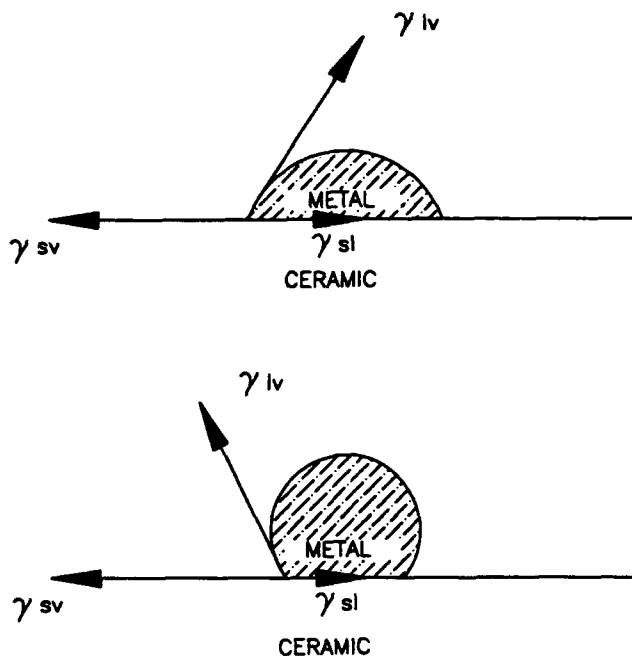


Fig. 1—A schematic illustration of wettability for a liquid metal in contact with a ceramic substrate.

been observed experimentally. Researchers in numerous previous studies have estimated the contact angle between alumina and molten metals. A good summary of these values is presented by Nicholas,^[1] Naidich,^[6] and Beruto *et al.*^[8] The wettability parameter here is evaluated using the specific surface energy data obtained from the tabulation by Murr^[9] and the contact angles from various sources listed in Table I.

Figure 2 shows a plot of the measured wettability parameters $\gamma^v \cos \theta$ taken from literature^[6,10] against ΔG_r for various metal-alumina interfaces. The parameters used in the calculation are listed in Table I. Data points shown in the plot were calculated for a 100 °C superheat above the melting temperature of the metal.

The plot is divided into four quadrants based on the positive and negative values of either terms. Quadrants 1 and 4 would represent the wetting and nonwetting regimes, respectively. Most noble metals lie in the nonwetting region (fourth quadrant). The bulk thermodynamic values predict that the reaction shown in Eq. [1] would proceed in the forward direction (ΔG_r is negative) for

Table I. Model Parameters, ΔG_r , and Wettability Predictions for Alumina Surface

Metal Alloy	T (°C)	ΔG° (kJ/mole)	Γ	ΔG_r (kJ/mole)	γ^v (mJ/m ²)	θ	$\gamma^v \cos \theta$ (mJ/m ²)
Cu	1183	-28.1	0.1	238.7	1300	160 ^[6]	-1221.6
Ni	1555	-76.5	0.01	156.4	1660	122 ^[6] 128 ^[8]	-847.8 -1021
Fe	1635	-142.3	0.03	110.3	1840	110 ^[8]	-629.3
Sn	432	-227.5	0.2	185.4	542	131 ^[8]	-355.6
Pb	523	-148.7	0.15	224.6	442		
Cu-5 pct Ti	1150	-290	0.1	10	1300	14 ^[6]	1261.4
Cr	1950	-630.3	0.1	53	1590	65 ^[6]	671.9
Mn	1345	-268.3	0.1	38.5	1060	70 ^[8]	362.5

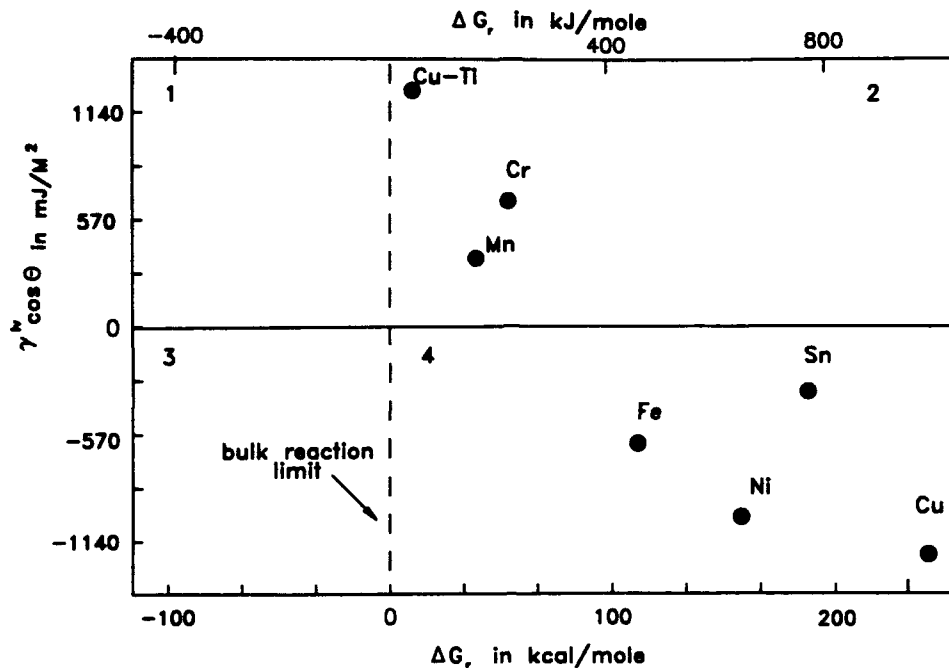


Fig. 2—The wettability of various liquid metals in contact with α -alumina, reported as the $\gamma \cos \theta$ of the Young equation, and compared to ΔG_w . The temperature for each metal was chosen to be 100 °C above the melting point.

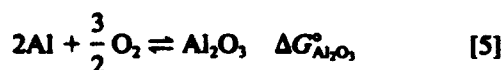
metals such as calcium, magnesium, and lithium. However, they are not shown in the plot because the experimental wettability parameters are not available. If present, these metals should lie in the wetting regime (first quadrant). The second and third quadrants are physically meaningless regimes. It can be seen from the plot that many commercially useful metals and alloys, such as manganese, chromium, and copper-titanium alloys, lie in the physically meaningless regime, where there are experimental observations that wetting occurs but bulk thermodynamics predicts otherwise.

Numerous previous studies by other researchers have attempted to explain this anomaly.^[11,11,12] Some researchers^[11] argue that the heat of solution for oxygen and for aluminum in reactive metals, such as titanium, are of considerable magnitude and the net heat change by Hess' law causes the reaction to proceed in the forward direction. This explanation cannot account for the fact that addition of a few percent reactive metal to an otherwise noble solvent causes a nonwetting-to-wetting transition.

III. SURFACE WETTING MODEL

A. Surface Phase Concept

The surface of a material can be treated as a separate phase in equilibrium with its bulk.^[13] This concept has been widely used by metallurgists in the field of surface adsorption and surface tension.^[14] In the case of a ceramic, alumina, for example, a Gibbs free energy of formation can be defined for a surface phase that is similar to the formation energy of the bulk:



The value of ΔG^{surf} would be less negative than ΔG° because the atoms on the surface are missing half their nearest neighbors and, thus, are loosely bound compared to the atoms in the bulk. Reducing the surface phase, therefore, requires less energy than reducing the bulk phase. It can be argued that a reaction between the surface phase of the ceramic and the molten metal is sufficient to cause wetting:



B. Free Energy of Wetting

The free-energy change for the reaction shown in Eq. [7], ΔG_w , defined as the Gibbs free energy of wetting, is much less than ΔG , given in Eq. [1]. Hence, some metals can wet a ceramic, even when a bulk reaction between the metal and the ceramic is thermodynamically not feasible. Quantitative wetting tendency predictions can be made if a numerical value for ΔG^{surf} is estimated.

A free surface is a defect state with an associated specific* defect energy, γ . Thermodynamically, γ is de-

*The term specific energy is used to signify an energy per unit area.

defined as the work required to increase the area of surface by unit amount in an adiabatic system of constant volume and constant composition. For a single component system, therefore:

$$\gamma = \left(\frac{\partial F^{\text{surf}}}{\partial A} \right)_{n,T,V} \quad [8]$$

where F^s is the surface excess Helmholtz free energy. Since the volume occupied by the surface is zero, the Helmholtz excess energy and the Gibbs excess energy, G^s , for the surface are equal. Integrating Eq. [8] and substituting Gibbs surface excess energy, we get

$$G^s = A\gamma \quad [9]$$

where A is the area occupied by one mole of the material on the surface.

It is common to evaluate A using the relation^[14]

$$A = mN \left(\frac{V_m}{N} \right)^{2/3} \quad [10]$$

where V_m is the molar volume, N is the Avogadro's number, m is the fraction of nearest-neighbor atoms lying in an adjacent layer, and therefore, m is a function of local surface structure. For consistency, we have assumed that the number of nearest neighbors surrounding an atom in the surface phase is nine and three atoms are in the layer immediately below. Therefore, a value of $1/4$ is used for m in the calculation.

The G^s quantifies in Gibbian terms the excess energy associated with the surface phase with respect to the bulk phase. Therefore, in terms of formation energies,

$$\Delta G^{surf} = \Delta G^\circ + G^s \quad [11]$$

where ΔG° is the formation energy of the ceramic substrate (Eq. [5]). Equation [11] implies that the surface phase is more readily available for reduction; *i.e.*, the energy required to reduce the surface phase is less than that of the bulk by G^s . The free-energy change for the reaction shown in Eq. [7] is

$$\Delta G_w = 3\Delta G_{M_2O}^\circ - \Delta G_{Al_2O_3}^\circ + G^s + RT \ln \left(\frac{a_{Al}^2}{a_M^3} \right) \quad [12]$$

in other words,

$$\Delta G_w = \Delta G_r + G^s \quad [13]$$

This reaction (Eq. [7]) does not go to completion. The surface phase is exhausted as soon as a monolayer of reaction product is formed. However, the sign and magnitude of ΔG_w indicate the spontaneity of wetting.

The specific surface energy at zero Kelvin, γ° , and the surface entropy, S^s (temperature coefficient of surface energy), are required to estimate the surface specific energy γ at the temperature of reaction according to Eq. [14]:

$$\gamma = \gamma^\circ + S^s \Delta T \quad [14]$$

The Gibbs surface excess energy, G^s , can be calculated from γ using Eq. [9].

Data on specific free surface energies and the temperature coefficients of specific surface energy for ceramics are not readily available. However, some values are tabulated,^[15] and theoretical techniques do exist to calculate these parameters.^[16]

The term ΔG° for compounds represents the free energy of formation in an isolated system. In the present situation, the reaction product forms at the interface adjacent to the alumina. Therefore, the ΔG° value should be corrected for any interaction between the oxide formed and the alumina prior to substitution of that value into

Eq. [12]. However, the heat of mixing or the heat of complex oxide formation from the two metal oxides is negligible compared to the heat of formation of the oxide itself.^[17] Kubaschewski tabulated the heat of formation of various oxides^[17] and demonstrated that the heat of formation of various complex oxides from the respective parent oxides is an order of magnitude less negative than that of the simple metals themselves. Therefore, as a first approximation, the correction factor can be neglected. In fact, the ΔG_w predictions will not be very different, even if a complex oxide forms at the interface instead of M_2O for the very same reason. Formation of complex spinel oxide from the M_2O at the interface between M_2O and the ceramic substrate does not result in large energy changes.

C. Reaction Wetting (Alloys)

It is common practice in the industry to add a few percent of reactive metals to an inert solvent to enhance wettability. Adapting the procedure developed here to predict wettability trends in the alloy-ceramic interface is straightforward. It is reasonable to assume that there are no chemical interactions between the noble solvent and the ceramic surface. If necessary, the procedure already outlined can be used to establish the lack of interaction between the noble solvent and the ceramic. The metal, M , in Eqs. [7] and [12] would then represent the reactive metal. The activity of the metal is no longer unity. It is dependent upon the concentration of the alloying addition available at the interface and also upon the activity coefficient of the alloying element in the melt. Quantitative estimates of surface segregation can be made using the empirical expression developed by Miedema *et al.*^[18] For dilute solutions:

$$\frac{C_A^{surf}}{C_A^{bulk}} = \exp \left(\frac{f\Delta H_{sol} - g(\gamma_A - \gamma_B) V_A^{2/3}}{3RT} \right) \quad [15]$$

where A and B are the solute and the solvent, respectively, γ is the surface energy, ΔH_{sol} is the heat of solution of A in B , V_A is the molar volume of A , and f and g are constants.^[18]

IV. EXPERIMENTAL TECHNIQUE

The sessile-drop experiment is a popular method to evaluate the experimental contact angles.^[6] Considerable inaccuracy is associated with these experiments; the results are very sensitive to the local atmospheric conditions around the drop. This problem is particularly severe in reactive metals which are prone to surface oxidation. There is a continuous depletion of the reactive metal in the alloy. Also, the solid oxide layer on the metal influences the stable drop shape.

Contact angles in the present work were determined experimentally using the capillary rise technique. The liquid levels, in the capillary rise method, can be measured to a better accuracy than solid angles subtended by the liquid drop in the sessile drop experiments. As opposed to the sessile drop experiments, the capillary rise technique uses large volumes of metal; therefore, the surface area-to-volume ratio is considerably reduced. The

surface contaminants can be bubbled off the tube by bubbling argon through the capillary tube, and the measurements are made away from the oxidized area.

The capillary rise apparatus was designed to measure the depression of the liquid level in the ceramic tube with respect to the level in the crucible. A schematic of the experimental apparatus is shown in Figure 3. Experiments were performed in a sealed mullite chamber which was evacuated using a mechanical pump and backfilled with high-purity argon. The argon gas was recirculated through the molecular sieve to scavenge the moisture in the chamber; the recirculation system was run at an over pressure of 35 kPa to prevent any air infiltration. The α -alumina tube was mounted on the moving support assembly above the 45-mm-diameter by 76-mm-long cylindrical graphite crucible. The metal of interest was melted and maintained at the required temperature in the chamber.

The liquid level in the crucible was measured using an acoustic feedback technique. The chamber was brought to the atmospheric pressure by venting through vent no. 2 shown in Figure 3. Argon gas was blown through the ceramic tube at a flow rate of 10^{-6} m³/min, and simultaneously, the capillary tube was lowered. The moment the bottom of the capillary tube touched the liquid metal, bubbles were formed. The acoustic emissions associated with bubble formation were captured by a microphone (Figure 3). The level of the tube when argon began to bubble was marked as the liquid level in the crucible.

The liquid level inside the alumina tube was measured using the electrical continuity principle. A continuous nichrome wire, terminated at a centimeter inside the ceramic tube, was mounted in place prior to the experi-

mentation. The other end of the continuity wire was connected to the graphite crucible. The circuit also consisted of an electric lamp that served as a continuity detector. Once the liquid level in the crucible was ascertained using the acoustic technique, the pressure inside the tube was brought to the atmospheric pressure by releasing the argon gas through vent no. 1. The pressure inside the tube was thus equilibrated to the pressure in the chamber. The tube was then lowered into the molten metal until continuity was detected.

The difference between the liquid level inside the tube and the level in the crucible is the capillary drop, h . The height, h , can be related to the wettability parameter, $\gamma^v \cos \theta$, by the Laplace-Young equation:

$$\gamma^v \cos \theta = \frac{r\rho gh}{2} \quad [16]$$

where r is the radius of the capillary tube, g is the acceleration due to gravity, and ρ is the density of the liquid.

Coors AD-998 alumina tubes (4-mm inside diameter) were used to measure the wetting angle against pure copper, tin, lead, and copper-5 wt pct titanium alloy. Metals of 99.99 pct purity were used. Homogeneous copper-titanium alloys were prepared in a vacuum induction melting unit from a copper-30 wt pct titanium master-alloy (obtained from Metallurgical Products, Pittsburgh, PA).

A graphite foil was used as a sleeve to prevent any reaction between the graphite crucible and copper-titanium alloy. The composition of the alloy was verified by the energy-dispersive X-ray attachment to the scanning electron microscope. No change in composition was observed for the alloy after the wetting experiment.

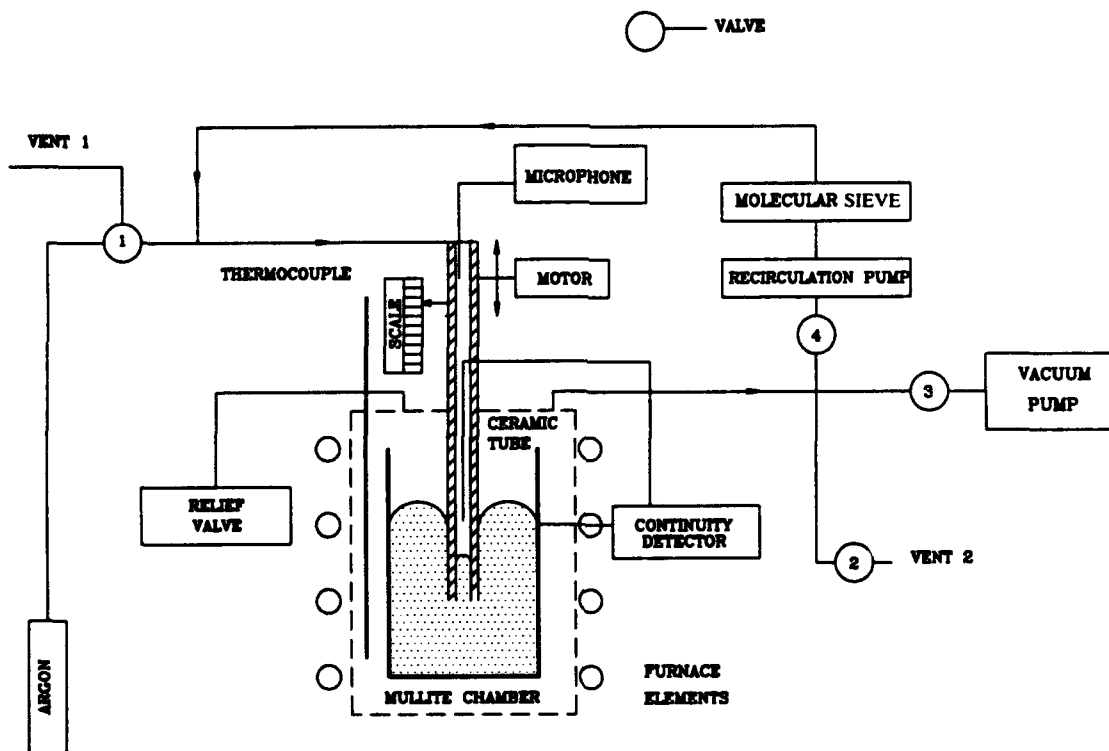


Fig. 3—Experimental apparatus for capillary rise measurements.

Therefore, the loss of titanium due to oxidation and reaction with the graphite foil was considered negligible.

V. RESULTS

The free energies of formation ΔG° at all temperatures of interest were obtained from a thermochemical handbook.^[5] The specific surface energy data are more difficult to obtain. Kingery *et al.*^[15] report a value of 905 mJ/m² for aluminum oxide at 1800 °C; and Tasker,^[19] based on theoretical calculations, reported an average specific surface energy of polycrystalline alumina to be 2600 Mj/m² at zero degree Kelvin. From these values, a surface specific entropy (temperature coefficient of specific surface energy) of 0.8 Mj/m²K was estimated. Based on these values, ΔG^{surf} was estimated for all temperatures of interest. Equation [12] was then used to calculate ΔG_w for various metals. The most stable oxide of the metal was used to calculate the ΔG° . Free energies and other parameters used in the calculation are tabulated in Table II. A positive ΔG_w was obtained for copper, iron, nickel, tin, and lead; while a negative free energy of wetting was obtained for titanium, chromium, and manganese. This observation is consistent with the previously published experimental results (the $\gamma^v \cos \theta$ values from literature are reproduced from Table I for comparison).

Reproducible measurements of contact angle have been recorded using the capillary rise equipment for a few alumina-metal systems. A nonwetting behavior was observed for copper, tin, and lead wetting on an alumina surface. Figure 4 shows the measured wettability parameter $\gamma^v \cos \theta$ as a function of temperature for these metals. The wettability parameter was found to decrease with increasing temperature. The present experimental results for a 100 °C superheat for each metal are also shown in Table II. An increase in the capillary level by 0.8 cm in a 0.4-cm alumina tube was observed for the copper-titanium alloys, thereby implying a wetting behavior. However, a wettability parameter was not estimated in wetting systems for reasons explained earlier in this article.

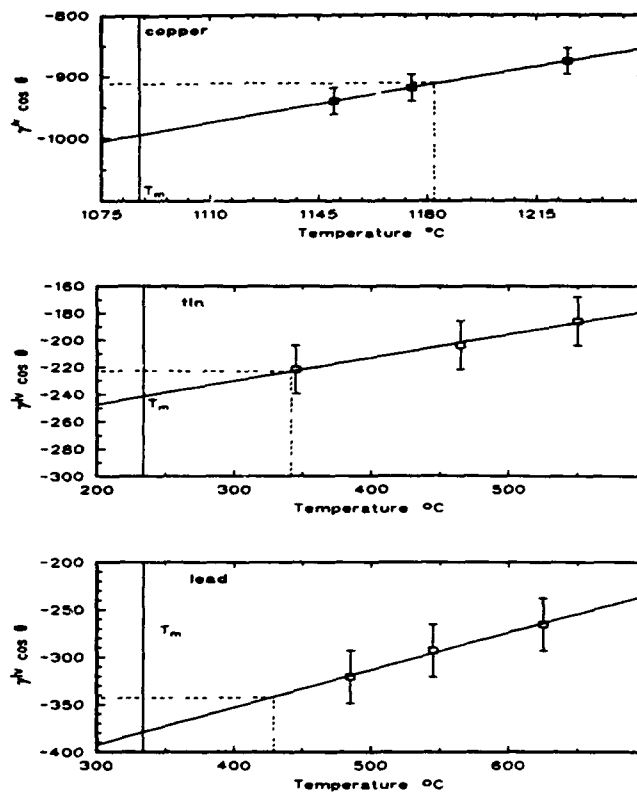


Fig. 4—Experimental wettability parameters for copper, tin, and lead in contact with α -Al₂O₃ at various temperatures.

VI. DISCUSSION

To verify the surface wetting model predictions, a wettability map, similar to Figure 2, was drawn between ΔG_w and $\gamma^v \cos \theta$ (Figure 5). The experimental results from this study are shown in the plot with error bars. The values in Table II, which are reported for a 100 °C superheat above the melting temperature of each metal, are used in the map. The ΔG_w values in the wetting regime are shown as vertical lines, since the experimental

Table II. Free Energies ΔG^{surf} , ΔG_w , and Wettability Predictions for Alumina Surface

Metal Alloy	T (°C)	ΔG^{surf} (mJ/m ²)	ΔG_w (kJ/mole)	θ	$\gamma^v \cos \theta$ (mJ/m ²)
Cu	1183	-182.0	135.17	160 ⁽⁶⁾	-1221.6
				134*	-915.8
Ni	1555	-175.1	69.12	122 ⁽⁶⁾	-847.8
				128 ⁽⁸⁾	-1021
Fe	1635	-174.3	28.5	110 ⁽⁸⁾	-629.3
Sn	432	-195.9	25.41	131 ⁽⁸⁾	-355.6
				114*	-218.5
Pb	523	-194.5	81.34	134*	-310
				—	—
Cu-5 pct Ti	1150	-172.2	-83.27	—	—
Cr	1950	-173	-22.9	65 ⁽⁶⁾	—
Mn	1345	-179.8	-48.84	70 ⁽⁸⁾	—
				30 ⁽¹⁰⁾	—

*Present experimental result

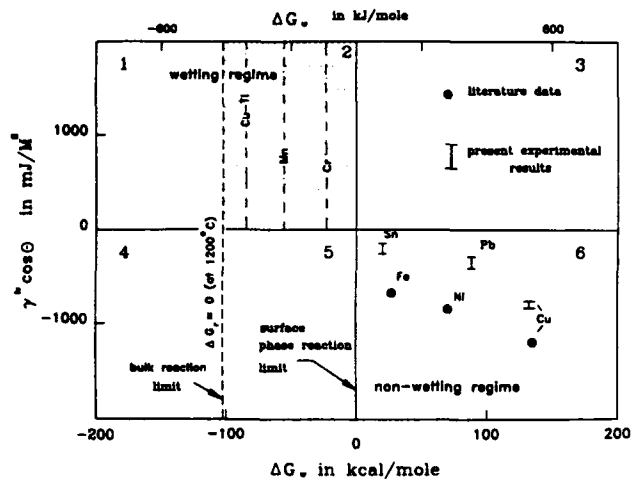


Fig. 5—Wettability map for various liquid metals in contact with α - Al_2O_3 . The temperature for each metal was chosen to be 100 °C above the melting point.

capillary rise value cannot be translated into the wettability parameter. The data points shown in Figure 5 will change with temperature; however, as demonstrated by Figure 4, the temperature sensitivity of the wettability parameter is very small.

The wetting and nonwetting regimes shown in the plot correspond to a negative and positive free energy of wetting. Nonreactive metals, such as, copper, tin, iron, and nickel, fall within the nonwetting region. The uniqueness of the present approach is its ability to accurately predict a wetting behavior for reactive metals, such as titanium, chromium, and manganese. The wetting regime also encompasses a bulk thermodynamic reaction regime (region 1). A dotted line is drawn at the point where ΔG_r is zero; chemical reactions can occur spontaneously at any point to the left of this line. The difference between ΔG_r and ΔG_w is the surface energy G^{sz} (Eq. [13]), which is a function of temperature. It can be seen from the map that titanium, chromium, and manganese are present in a regime (region 2) where wetting is possible but no bulk reaction can occur. This region is highlighted in the plot by shadowing. Similar to the plot shown in Figure 2, regions 3 through 5 are physically meaningless regimes; the presence of any element in these regions would imply a failure of the model.

A wettability map of this nature is very useful in selecting metal-ceramic pairs, both for materials processing of composites and joining applications. Intimate contact between the metal and the ceramic can be obtained only when the metal lies in region 1 or 2 in the wettability map. The liquid metal should wet the surface of the ceramic substrate to maximize the load-carrying capability of the metal-ceramic pair. However, a consideration just as important as wettability is the stability of the metal-ceramic interface. If the metal lies in the bulk reaction regime (region 1), an unstable interface is formed. The bulk chemical reaction at the interface is limited only by the kinetic processes. With sufficient mass transport, a large interfacial reaction zone will be formed. Interfacial reaction products typically are brittle materials and, therefore, can cause a premature failure in the

mechanical applications of the metal-ceramic component. Hence, a good companion metal, for a given ceramic, should lie within the wetting regime where no bulk reaction is possible (highlighted region). In this situation, the liquid metal is of an optimal thermodynamic activity which is sufficient to reduce the surface phase but not the bulk substrate. Therefore, a stable interface results as soon as the surface phase is exhausted. These concepts of suitable, but not excessive, interfacial reactivity should apply equally well to the materials processing of metal-matrix composites and to metal-ceramic joining.

The theoretical approach demonstrated here is based on purely thermodynamic principles; therefore, this approach should be valid for all interfaces where a chemical reaction occurs at the interface. Although alumina was the only ceramic discussed in this article, the theoretical method can be used to identify the metals/alloys that form stable interfaces with any given ceramic substrate.

The free-energy changes ΔG_r and ΔG_w are the driving forces for reaction and wetting, respectively, and the values estimated are true only at the initiation of wetting. Therefore, they can be used only as a criterion to predict if wetting would occur for a given system. This model does not attempt to explain the equilibrium interfacial compositions.

VII. CONCLUSIONS

A thermodynamic criterion has been established to predict wettability at metal-ceramic interfaces—wetting occurs when the free energy of wetting, ΔG_w , is negative. This ΔG_w is the free-energy change associated with the reaction between the surface phase of the ceramic and the metal. The model predictions have been verified for alumina ceramic.

Capillary rise technique can be successfully used to experimentally measure the contact angle for nonwetting systems.

LIST OF SYMBOLS

A	area occupied by one mole of surface phase
a_M	activity of the species M
C_M	concentration of the species M
F^{sz}	surface excess Helmholtz free energy
ΔG°	standard Gibbs free energy of formation
ΔG_r	Gibbs free energy of reaction
ΔG^{surf}	Gibbs free energy of formation of the surface phase
ΔG_w	Gibbs free energy of wetting
G^{sz}	surface excess Gibbs free energy
g	acceleration due to gravity
ΔH_{sol}	enthalpy of solution
h	height of capillary change
m	near-neighbor correction factor
N	Avogadro's number
r	capillary radius
S^s	surface specific entropy
V_m	molar volume
X	mole fraction

α	alpha phase
γ	specific surface energy
γ^0	specific surface energy at zero Kelvin
γ^v	solid-vapor interfacial energy
γ^l	liquid-vapor interfacial energy
γ^s	solid-liquid interfacial energy
Γ	activity coefficient
ρ	density

ACKNOWLEDGMENTS

This research was supported both by the Strategic Defense Initiative Office/Innovative Science and Technology, under ONR Contract No. N00014-88-K-0500, and by the Welding Research Council. The encouragement of Dr. Steven Fishman is gratefully acknowledged.

REFERENCES

1. M.G. Nicholas: *Mater. Sci. Forum*, 1988, vol. 29, pp. 127-50.
2. M. Naka, Y. Hirono, and I. Okamoto: *Trans. JWRI*, 1987, vol. 2, pp. 81-87.
3. R.E. Tressler, T.L. Moore, and R.L. Crane: *J. Mater. Sci.*, 1973, vol. 8, pp. 151-61.
4. R. Hultgren, P.D. Desai, D.T. Hawkins, and M. Gleiser: *Se-*

- lected Values of Thermodynamic Properties of Binary Alloys, ASM, Metals Park, OH, 1973, pp. 125-804.
5. JANAF Thermochemical Tables, 2nd ed., U.S. Dept. of Commerce, 1977, pp. 20-257.
6. Yu. Naidich: *Prog. Surf. Membrane Sci.*, 1981, vol. 14, pp. 353-486.
7. J.A. Pask: *Ceram. Bull.*, 1987, vol. 66 (11), pp. 1587-92.
8. D. Beruto, L. Barco, and A. Passerone: in *Oxide and Oxide Films*, A.K. Vijh, ed., Marcel Dekker Inc., New York, NY, 1981, vol. 6, pp. 1-84.
9. L.E. Murr: *Interfacial Phenomena in Metals and Alloys*, Addison-Wesley Publishing Co., Reading, MA, 1975, pp. 101-05.
10. G.V. Samsonov: *The Oxide Handbook*, translated by R.K. Johnston, 1982, Plenum Press, New York, NY, pp. 400-08.
11. A.J. Moorehead, H.M. Henson, and T.J. Henson: in *Ceramic Microstructures '86: Role of Interfaces*, J.A. Pask and A.G. Evans, eds., Plenum Press, New York, NY, 1988, pp. 949-58.
12. J.T. Klomp: in *Joining Ceramics, Glass and Metal*, W. Kraft, ed., DGM, Verlag, Germany, 1989, pp. 55-64.
13. J.W. Gibbs: *Collected Works of J.W. Gibbs*, Yale University Press, New Haven, CT, 1948, vol. 1, pp. 219-50.
14. K.S. Yeum, R. Speiser, and D.R. Poirier: *Metall. Trans. B*, 1989, vol. 20B, pp. 693-703.
15. W.D. Kingery, H.K. Bowen, and D.R. Ulman: *Introduction to Ceramics*, 2nd ed., John Wiley, New York, NY, 1976, p. 187.
16. R.H. Bruce: in *Science of Ceramics*, G.H. Stewart, ed., Academic Press, London, 1965, vol. 2, p. 359.
17. O. Kubaschewski: *High Temperatures-High Pressures*, 1972, vol. 4, pp. 1-12.
18. A.R. Miedema: *Z. Metallkd.*, 1978, vol. 69, pp. 455-61.
19. P.W. Tasker: in *Adv. Ceram.*, W.D. Kingery, ed., 1984, vol. 10, pp. 176-89.

FUNDAMENTAL ISSUES CONCERNING THE MICRODESIGNING OF METAL-CERAMIC INTERFACES

PR. Chidambaram, G. R. Edwards and D. L. Olson
Center for Welding and Joining Research
Colorado School of Mines; Golden Co-80401

Abstract:

Three distinct types of metal-ceramic interfaces are summarized. The nature of the bonding, problems in quantifying wettability, the thermodynamic driving force for interface formation, and certain aspects of interfacial stability are discussed with the help of examples. The surface wetting model developed previously by the authors is also discussed.

INTRODUCTION

Designing with materials for high technology applications is a fast emerging field in materials engineering, and many new composite components with properties that are tailored to the specific application have been developed [1-3]. The compatibility of the different materials which comprise a composite is an essential consideration in tailoring a composite to its design. In particular, the formation and stability of the internal interfaces pose a significant challenge to the materials designer.

In this paper, we discuss the various approaches available for forming stable metal-ceramic interfaces - both solid-solid and solid-liquid. Metal-ceramic composite components are being used in the structural and electronic packaging industry. A structural component such as a silicon nitride rotor brazed to a stainless steel shaft requires bond energies of the order of the cohesive strength of silicon nitride ($\sim 1600 \text{ mJ/M}^2$).

Ceramic materials are typically ionic or covalent, while metallic materials derive their cohesive energy from metallic bonds. Therefore, when in contact, the difference in the nature of bonding between the metal and the ceramic results in a largely positive interfacial energy. Since interface formation demands external energy, the system is non-wetting. The first challenge of the materials designer is to render the ceramic surface wettable by the molten metal. The interfacial energy can be reduced by developing certain attractive forces across the interface. Based on the nature of the attractive forces, wetting can be classified as physical or chemical. This type of classification also aids in the independent development of quantitative calculations of the wetting tendencies.

The general case of a liquid metal in contact with the ceramic is shown in Figure 1, where a balance of surface tension forces results in the familiar Young equation:

$$\gamma^{lv} \cos \theta = \gamma^{sv} - \gamma^{sl} \quad (1)$$

In this expression, γ^{sv} , γ^{lv} and γ^{sl} are the corresponding surface energies of solid/vapor, liquid/vapor and solid/liquid interfaces respectively. The wettability parameter, $\gamma^{lv} \cos \theta$, describes the wetting tendency of the liquid on the solid substrate. A positive value signifies a wetting system. This is a very simplistic interface model, and is inadequate to describe many chemically wetting metal-ceramic systems. Chemically wetting systems rely on irreversible chemical bond formation at the interface; when new interfacial phases form a

simple surface tension balance presented in Eqn. 1 is no longer valid.

Physical and chemical wetting principles are illustrated with examples in the following sections. Each approach is evaluated in terms of the wetting susceptibility, bond energies and the stability of the interface. Apart from wetting, spreading of the liquid on the ceramic surface is an important consideration from a processing point of view. An attempt is made to understand spreading in each situation. A predictive model developed by the authors to isolate the reaction wetting systems is also discussed [4].

PHYSICAL WETTING

Physical wetting can be defined as the phenomenon observed in a solid-liquid system where the interface formation is energetically favored by the reversible physical forces across the interface. Van der Waals forces and electrostatic attractions are examples of such physical forces.

van der Waals Forces

Benjamin and Weaver [5] treated the first monolayer of the metal deposited on the ceramic as a physically adsorbed gas, and developed procedures to calculate the van der Waals attractive forces. McDonald and Eberhard [6] used a physio-chemical approach to quantitatively explain the observed wetting angles and the work of adhesion. The observed work of adhesion was treated as a sum of the contributions from the physical and chemical forces. They estimated the van der Waals forces from the ionization potentials and the polarizabilities of the metal atoms according to Benjamin and Weaver [5]. For most metals in contact with alumina, the van der Waals energy was estimated to be $\sim 500 \text{ Mj/m}^2$. These forces are relatively weak compared to the bond energies developed from chemical bonds. Naidich [7] used a similar approach to calculate the van der Waals energies and obtained energies of the same orders of magnitude.

Image Charges

Stoneham and Tasker in a series of publications [8-10] argue that the image interactions based on the polarizability of a ceramic is the primary force of adhesion. When a planar boundary separates two media of differing dielectric constants, the charges in each medium feel the effect of the boundary (Figure 2). The electrostatic force that results can be calculated in simple terms by the so-called image charges. The boundary is imagined to be a mirror plane and each charge contributes to the interaction term a force whose magnitude depends on the two dielectric constants ϵ^I and ϵ^{II} . Therefore, at a distance z from the boundary, a charge Q causes an image charge related work of adhesion (E):

$$E = \frac{Q^2}{2Z\epsilon^I} \left[\frac{\epsilon^I - \epsilon^{II}}{\epsilon^I + \epsilon^{II}} \right] \quad (2)$$

Assuming a boundary separation of $Z = 20 \text{ nm}$, the dielectric constant of the ceramic to be $\epsilon^I = 10$, the dielectric constant of the metal to be $\epsilon^{II} = \infty$, and the charges to be singly ionized with a surface charge density of $10^{19} \text{ charges/m}^2$, the image term yields an interfacial energy of 290 mJ/m^2 . This energy can reach 1500 mJ/m^2 if multiple charge states are present. According to this theory, materials with high charge density are the most amenable

for electrostatic wetting. The dielectric constant is a material property that measures the charge densities. Most metals wet any ceramic with a dielectric constant greater than 6.5.

Critical to obtaining the large work of adhesion suggested by Stoneham and Tasker (E in Eqn 2.) is the assumed distance of separation. It seems unreasonable to assume a separation of 20 nm. Also, all the surface defects are not present in the top monolayer. Furthermore, there is no concrete experimental evidence to corroborate the magnitude of this term.

Examples

Metal-ceramic interfaces in electronic components do not have stringent bond energy requirements. Physical forces can be very useful in such applications, because an interfacial chemical reaction can result in deleterious interfacial properties. Another form of physical adhesion promotion has been observed in ion beam enhanced adhesion of thin films. A thin metallic film deposited on a ceramic or glass substrate demonstrates an improvement in adhesion of two orders of magnitude after a post bonding irradiation treatment [11-12]. This phenomena has been observed in alumina, silica, and glass substrates with various metal depositions, including gold, silver, and copper. There are no convincing theoretical explanations available in the literature to explain this phenomenon.

Wetting and Spreading

The Young equation (Eqn. 1) is relatively descriptive of the energy balance in physically wetting systems. Therefore, the contact angle quantitatively measures the wetting tendency. The interfacial work of adhesion can be derived from the Young equation:

$$W = \gamma^{lv} [1 + \cos \theta] \quad (3)$$

This situation is more complicated in chemically wetting systems. Physical wetting does not pose any serious threat to interfacial stability. No electron or charge is transferred across the interface when physical wetting occurs; hence, the interfacial stability is maintained. Spreading can be defined to occur when the liquid, after attaining the zero contact angle configuration, has further driving force to cover the surface of the solid. The liquids that are capable of spreading do not form stable contact angles. Thermodynamically, spreading occurs when $(\gamma^{sv} - \gamma^{sl}) > \gamma^{lv}$. This condition is satisfied when γ^{sl} is very small; often spreading is known to occur when γ^{sl} is negative. Mathematically, spreading can be expressed in terms of a spreading coefficient S, defined as:

$$S = \gamma^{sv} - \gamma^{sl} - \gamma^{lv} \quad (4)$$

According to this equation, spreading can occur only when S is positive.

CHEMICAL WETTING

Interface formation by virtue of chemical bonds across the interface can be defined as chemical wetting. Chemical bonds are formed when the electronic structure of the surface

atoms of both the mating species are altered. Such changes can occur by a charge transfer reaction or by a simple mixing process of one phase dissolving in the other.

SOLUTION REACTIONS

Chemical bonds are formed automatically when one phase dissolves in the other. Two materials of similar bonding nature tend to exhibit moderate mutual solubilities. An elegant exploitation of this situation in metal-ceramic oxide system is achieved by oxidizing the metal:



The metal oxide and the ceramic oxide can then combine as a solution. The ceramic phase diagrams can be used as a predictive tool to identify both the systems that are amenable to solution wetting and the appropriate processing temperature. Three illustrative phase diagrams are shown in Figure 3. These oxide-oxide phase diagrams show two types of mixing amongst the two components, a terminal solid solubility (Figure 3b) and a complex oxide or compound formation (Figure 3c). In Figure 3a, there is no solubility in the solid state; and therefore, it is impossible to form chemical bonds, below the eutectic temperature, between the two components that exhibit this type of phase diagram. However, the components found in phase diagram of the type shown in Figures 3b or 3c are amenable to solid solubility and can be processed below the eutectic temperature to obtain a favorable interface. In all three cases, at temperature T_1 , when MO is a liquid, the liquid dissolves the solid to reach the liquidus composition, and hence will wet the solid.

A solid-solid contact at the processing temperature is kinetically unfavorable. Also, an intimate atomic contact at the interface is essential to realize the maximum possible bond energy. These factors make a liquid-solid contact much more desirable for materials processing. Ceramic oxides of commercial interest usually melt at relatively high temperatures. Therefore, this approach is very effective in systems where a low melting metal oxide can be formed. The eutectic compositions in the metal-oxygen phase diagrams, (iron-oxygen and copper-oxygen (Figure 4)) are very conducive to such a liquid phase formation at the interface.

Wetting and Spreading

It is helpful to quantitatively order the various wetting tendencies. In physically wetting systems, it was shown that the contact angle is a quantitative measure of the wetting tendencies; however, in chemically wetting systems it is not true. Formation of a new phase interposes a new interface, and the simplistic Young equation cannot describe the interfacial balance in this case. Furthermore, the contact angle in solution wetting systems is also a function of the nature of the solid and the liquid. Sharps et. al [19] demonstrated that when equilibrium solids and liquids are brought into contact, the liquid does not spread on the solid. Figure 5 shows the copper-gold phase diagram and some observed sessile drop configurations [19]. A solid of composition that falls on the solidus (B in Figure 5) or a liquid composition on the liquidus (C in Figure 5) are considered to be passive phases; any other composition is considered to be active. The liquid spreads on the solid whenever the solid

is active. When an active liquid (D on B in Figure 5) is in contact with a passive solid the liquid dissolves some of the solute from the solid and a solution bonding occurs; however, the contact angle does not reduce to zero [19]. When the solid dissolves the liquid (D or B on A in Figure 5) a rapid decrease in contact angle and spreading are observed. Hence the contact angle is not a true representation of the interfacial energy balance.

The above idea can be applied to the phase diagrams shown in Figure 3 to investigate the spreading tendencies. At T_1 when liquid MO and solid CO are in contact, the phase diagram in Figure 3a would correspond to a passive solid and active liquid (D on B in Figure 6). In this situation, even though a solution reaction occurs, spontaneous spreading is not observed. For the same conditions in Figure 3b and 3c, both the solid and the liquid are active and hence, a desirable spreading is observed.

Examples

The solution wetting approach has been used in glass-metal sealing since 1950 [13], and detailed studies concerning mechanism of glass softening and oxide solution have been published [14-15]. Since the ceramic-metal couple is the topic of interest in the present paper, glass-metal systems will not be further discussed. Wetting by solution reactions were demonstrated by Chaklader et. al. in the alumina-copper oxide system [16], and later the same system was commercially applied [17]. Pure copper does not wet alumina [4]; however, copper oxide additions to copper causes rapid wetting. Figure 4 shows the copper-oxygen phase diagram [18]. As can be seen from the figure, copper- 0.39 wt. % oxygen eutectic melts at 1065°C. Upon preoxidation of copper (Eqn 5.) or copper oxide addition a eutectic melt forms at the interface, above 1065°C. When in contact with alumina, the oxide undergoes a solution reaction with alumina. A closer look at the copper oxide - alumina phase diagram (Figure 6) reveals that it is similar to the phase diagram in Figure 3c. Therefore, a spinel phase forms according to the reaction:



and exhausts the liquid at the interface. Once the liquid oxide phase is exhausted, pure copper is in contact with alumina and the spinel. Since copper does not have the thermodynamic potential to reduce either phase, a stable interface is formed. Since both liquid copper oxide eutectic and alumina are active phases, spontaneous spreading occurs. The final equilibrium structure consists of Al_2O_3 in contact with CuAlO_2 . Although the above discussion was based on oxide ceramics, this approach can be used equally well in non-oxide ceramics.

In summary, the three desirable conditions for solution wetting are: a) a low melting eutectic metal-anion combination, b) some solubility or spinel formation at the processing temperature, and c) a solid that is active (i.e. a solid that can dissolve the liquid). Interfacial stability during application is rarely a problem because the active liquid phase is exhausted, and the metal does not have independent thermodynamic activity to reduce the ceramic.

REDUCTION REACTIONS

Active brazing or direct bonding [20-22] is a popular technique that has been recently developed to braze metals to ceramics. The procedure involves reducing the anions on the surface of the ceramic with a reactive metal in the braze. Only reactive metals with sufficient thermodynamic activity to reduce the ceramic can be used for this purpose. Titanium, zirconium, manganese and molybdenum are popular materials for this purpose; they are very often added in a small percentage to an otherwise noble braze alloy. The main advantage of this process is its effectiveness on most commercial ceramics, including: alumina [21], silicon carbide [23], and silicon nitride [24]. A crucial problem with redox wetting is the interfacial stability. A reduction reaction occurs only when the free energy change for the reaction is negative. This implies that further reaction can occur in service, and a large interfacial reaction layer can be formed. Ceramic composite components, metal-ceramic brazed parts, and ceramic thermal barrier coatings are typically used at relatively high temperatures; hence, the interfacial reaction rate is relatively high. Extensive interfacial phase zones have been observed in the zirconium-alumina system [25] and in aluminum-silicon carbide metal matrix composites [26]. However, not all reduction wetting systems suffer from interfacial instability. The conventional molybdenum-manganese process [27-28] and the solid state niobium-alumina brazing process [29] do not form large interfacial reaction layers.

Example

The niobium-alumina interface is of great commercial interest for two reasons. Both materials have very similar thermal expansion coefficients, and a reasonable lattice matching at the niobium (110) and alumina (0001) interface. High resolution transmission electron microscopy studies on diffusion-bonded, single crystal alumina-niobium by many researchers [30-32] have revealed an atomically smooth interface. In a recent study, F. S. Ohuchi and M. Kohyama [29] used X-ray and ultra violet photoelectron spectroscopy to monitor the in situ electronic structure changes of the alumina surface atoms upon deposition of various metals. These techniques map the core and valence electron density of states. A shift in the peak position corresponds to an electronic structural change that is associated with chemical bond formation. Based on the spectroscopic analysis and empirical tight binding energy band calculations, they concluded that a chemical bond develops between the deposited niobium atom and the oxygen atom on the surface of alumina.

A thermodynamic rationalization of such a bond formation would involve the following reactions:



The free energy changes for these reaction can be calculated from standard thermodynamic expressions. The required standard free energy of formation is available from thermodynamic data books [33]. An assumption concerning the activity of aluminum needs

to be made before the Gibbs free energy change can be estimated. For the present purposes, ideal mixing at a percent dissolution of aluminum in niobium is used [4]. The reaction shown in Eqn. 8 is a complex ceramic double oxide formation reaction, and commonly, the thermodynamic data for such reactions are not available. However, Kubaschewski [34] tabulated the double oxide formation energies involving alumina and an other transition metal oxide. For these materials, the free energy of double oxide formation was found to be less than 10 kcal/mole. Therefore, it is reasonable to assume that the energy change for the reaction shown in Eqn. 8 is negligible compared to the reduction reaction in Eqn. 7. The Gibbs free energy change for reaction shown in Eqn. 7 was estimated to be + 42 kcal/mole. Therefore, according to bulk thermodynamic calculations, a chemical reaction is not feasible.

Surface Wetting Model

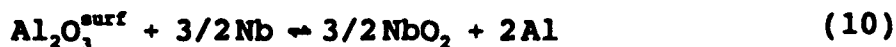
Such discrepancies in liquid metal-alumina systems were explained by a surface wetting model developed at the Colorado School of Mines by the current authors [4]. Wetting was treated as a surface phenomenon and a surface reaction monolayer was considered sufficient to cause wetting. Although this model was developed for liquid metal-alumina systems, it can be used without much modification to explain the observed behavior in the niobium-alumina system.

The surface of alumina can be treated as a separate phase with unique thermodynamic properties. A surface phase formation energy, ΔG^{surf} that is similar to the bulk formation energy, ΔG° can be defined. The atoms on the surface are at a higher energy than the bulk; this energy can be expressed in terms of Gibbs excess energy, G^{xs} :

$$\Delta G_{\text{Al}_2\text{O}_3}^{\text{surf}} = \Delta G_{\text{Al}_2\text{O}_3}^{\circ} + G^{\text{xs}} \quad (9)$$

The procedure established to estimate G^{xs} involves the use of experimentally estimated surface specific energy γ ; details of the calculation are published elsewhere [13].

Now, a reaction between the surface phase of alumina and niobium can be considered,



and the free energy change for that reaction denoted as free energy of wetting ΔG_w :

$$\Delta G_w = 3/2\Delta G_{\text{NbO}_2} - \Delta G_{\text{Al}_2\text{O}_3}^{\circ} + G^{\text{xs}} + RT \ln \left(\frac{a_{\text{Al}}^2}{a_{\text{Nb}}^{3/2}} \right) \quad (11)$$

This value was estimated to be - 120 kJ/mole. Hence this reaction can proceed in the forward direction. Figure 7 [4] shows the similar ΔG_w plotted against the experimentally measured wetting angles for molten metals and alloys. The positive $\gamma^{\text{lv}} \cos \theta$ and the negative ΔG_w imply a wetting system. Noble metals fall in region 6 since they do not have sufficient thermodynamic activity to reduce the surface or bulk phase of alumina. Titanium, manganese

and chromium fall in the region where a surface wetting is possible but a bulk reaction is not. This corresponds to wetting process where ΔG_r is positive while ΔG_w is negative. As seen earlier, this is also true for the solid state reaction between niobium and alumina. Hence, niobium would fall in region 2 of the plot in Figure 7. Niobium, when in contact with alumina, reduces the oxygen on the surface. As soon as the surface phase is exhausted, the driving force for reaction no longer exists and a stable, atomically smooth interface is obtained. This model has also been applied to quartz-metal interfaces, and a reasonable correlation between the theoretical predictions and the experimental wettabilities was observed (Figure 8) [35].

Wetting and Spreading

Quantitative wettability predictions are very complex for redox systems. There are very few models that attempt to address the quantitative aspects of reaction wetting. Pask [36] argues that interfacial energy balance is altered by the energy released in the reaction, and that the reaction energy can be included in the Young equation as a correction term. However, as mentioned before, formation of a new phase generates a new interface, and a single interfacial energy term cannot completely describe the interfacial energy.

The instant the reactive metal comes in contact with the ceramic, a non-wetting contact angle is formed because no reaction has occurred. The interfacial reaction products or chemical bonds form by surface nucleation and growth [37] under the reactive melt. There are no concrete models that explain why the liquid spreads beyond the initial triple point. Figure 9 schematically describes the dynamic situation where the liquid spreads on the solid ceramic. The observed contact angle is a complex function of the kinetic arrests at the triple point. Experimental procedures to isolate this phenomenon and understand the driving force for spreading are currently in progress at the Colorado School of Mines. The contact angle, often reported as the quantitative measure of the wetting tendency [6,7] does not contain any information concerning the fundamental work of adhesion.

CONCLUSIONS

Three distinct types of metal-ceramic interfaces exist. The essential features of these interfaces are summarized in Table I.

- Physically wetting systems are very rare and very few commercial examples exist. The bond energies obtained in this type of interface are relatively low. The interface formed obeys the classical interfacial equilibrium analysis.
- Metal-ceramic interfaces of commercial interest rely on chemical bond formation at the interface. Wetting and spreading in these systems cannot be treated by using the initial surface and interfacial energy terms.
 - Solution wetting systems do not suffer from excessive interfacial reaction. Ceramics that can be advantageously joined to metals by this approach are limited by the solubility and interfacial liquid layer formation.
 - Most ceramics can be bonded to metals using a reduction reaction route; however, the interfacial stability demands careful consideration. Wettability maps can be used to identify the metals or alloys which reduce only the

surface phase of the ceramic and remain in equilibrium with the bulk of the ceramic.

Acknowledgments : This research was supported by the Strategic Defence Initiative Office/Innovative Science & Technology under ONR contract # N00014-88-K-0500. The encouragement of Dr. S. Fishman is gratefully acknowledged

REFERENCES

- 1) C. F. Lewis, *Materials Engineering*, May (1986), p 33-37
- 2) J. Kubel Jr., *Materials Engineering*, Nov. (1985), p 23-26
- 3) W. R. Mohn, and G. A. Gegel, in *Proc. of Second Conf. on Advanced Composites*, ASM Intl., Dearborn, MI, USA, (1986), p. 69-73
- 4) PR. Chidambaram, G. R. Edwards and D. L. Olson, *Met. Trans. B*, (1992), vol. 23B, p 215-222
- 5) P. Benjamin and C. Weaver, *Proc. Roy. Soc., London, Ser. A*, (1959), vol. 252, p 418-430
- 6) J. E. McDonald, and J. G. Eberhart, *Trans. AIME*, vol. 233, (1965), p. 512-517.
- 7) Yu Naidich, *Prog. in Surf. and Membrane Sci.*, vol. 14 (1981), p. 353-486.
- 8) A. M. Stoneham, and P. W. Tasker, *J. Phys. C., Solid State Physics*, vol. 18 (1985), p. 1543 - 50
- 9) A. M. Stoneham and P. W. Tasker, *Phil. Mag. B*, vol. 55, No. 2, (1987), p 237-252
- 10) A. M. Stoneham and P. W. Tasker, in *Ceramic Microstructure 86*, Ed J. A. Pask et. al., New York Plenum Press, p 155-165
- 11) T. A. Tombrello, *Mat. Res. Symp. Proc. Vol. 25* (1984), p 173-178
- 12) J. E. E. Baglin, G. J. Clark, and J. Bottiger, *ibid*, p 179-188
- 13) J. A. Pask, *Proc. IRE.*, vol 36, (1948), p 286-289
- 14) A. P. Tomasia and J. A. Pask, *J. Am. Ceram. Soc.* vol. 64, (1981), p 523-28
- 15) J. J. Brennen and J. A. Pask, *ibid.*, vol. 56, (1973) p. 56-62
- 16) A. C. D. Chaklader, A. M. Armstrong, and S. K. Mishra, *ibid*, vol. 51, (1968), p. 630-33
- 17) J. F. Burgess, C. A. Neugebauer, and G. Flanagan, *J. of Electrochemical Soc.: Solid St. Sci. and Tech.*, vol. 122, (1975), p 688-90
- 18) *Phase Diagrams for Ceramists*, M. K. Reser editor, Am. Ceramic Soc., (1964) Columbus, Ohio, p. 232
- 19) P. R. Sharps, A. P. Tomsia, and J. A. Pask, *Acta Metall.*, vol. 29 [7], (1981) p. 855-65
- 20) H. Mizuhara (1986), U.S. Patent 4603090.
- 21) A. J. Moorhead, and H. Keating, *Welding Journal*, October (1986), p. 17-31
- 22) A. J. Moorehead, H. M. Henson and T. J. Henson: in *Ceramic Microstructures'86 : Role of Interfaces*, edited by Pask, J. A., and Evans, A. G., Plenum Press, New York and London, (1988), p. 949-958
- 23) D. B. Gundel and F. E. Wawner, *Scripta. Met. et. Materila*, vol. 25. (1991), p. 437-441
- 24) R. E. Loehman, *Ceramic Bulletin*, vol. 68, No. 4, (1989), p. 891-96

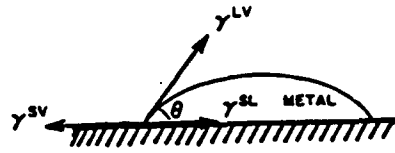
- 25) K. Bang, Ph. D. Thesis, Colorado School of Mines, Golden, Co, (1991)
- 26) E. Than, H. Podlesak, and G. Leonhardt, Vacuum, vol. 41, No. 7-9, (1990), p. 1750-52
- 27) M. Erg, and A. W. Hennicke, "Ceramics in Advanced Energy Technologies", Krockel, H. et al. editors, Dreidel Publishing Co., (1982), p. 138.
- 28) M. E. Twentyman, and P. Hancock, in "Surface and Interfaces in Ceramic and Ceramic-Metal Systems", J. A. Pask, and A. G. Evans, editors, Materials Science Research, vol. 14 (1981), Plenum Press, New York, p. 535.
- 29) F. S. Ohuchi and M. Kohyama, J. Am. Cerm. Soc., vol. 74, (1991), p. 1163-87
- 30) Y. Ishida, H. Ichinose, and S. Tanaka, in "Ceramic Microstructures '86; Role of Interfaces", Park J.A. and Evans, A.G., editors, Plenum Press, New York, (1988), p. 379-86.
- 31) W. Mader, Mat. Res. Symp. Proc. vol. 82, (1987), p. 403
- 32) M. Kuwabara, J. C. H. Spence, and M. Ruhle, J. Mater. Res., Vol. 4, No. 4, (1989), p. 972-977
- 33) JANAF Thermochemical Tables, 2nd edition, U. S. Dept. of Commerce, (1977), p. 20-257
- 34) O. Kubaschewski, High Temperatures-High Pressures, vol. 4, p. 1-12, (1972)
- 35) PR. Chidambaram, G. R. Edwards, and D. L. Olson, Proc. of SOJOM Conf. on Joining, Trichirapalli, India, (1991), p. 331-338
- 36) J. A. Pask., Ceramic Bull., vol. 66, NO. 11, (1987), p. 1587-92
- 37) PR. Chidambaram, and G. R. Edwards, AWS Conf. Detroit (1991)

Table I. Summary of the Three Distinct Types of Metal-Ceramic Interfaces

Wetting	Driving Force For Interface Formation	Typical Bond Energies mJ/M²	Predictive Tool	Examples
Physical	van der Waals Electrostatic	~ 500	- Dielectric Constant	NiO-M
Chemical		~ 1600		
Mixing	ΔG_m		Phase Diagrams	CuO-Al ₂ O ₃
Redox	ΔG_w		Wettability Maps	Ti-Al ₂ O ₃

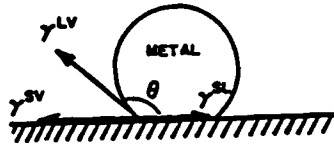
- Figure 1.** A schematic illustration of wettability for a liquid metal in contact with a ceramic substrate.
- Figure 2.** A schematic illustration of the image charges developed at metal-ceramic interfaces [9].
- Figure 3.** Oxide-oxide phase diagrams showing various types of solubilities
- Figure 4.** The copper-oxygen phase diagram [18].
- Figure 5.** a) The copper-silver phase diagram.
b) The sessile drop morphology for various solid-liquid interfaces [19].
- Figure 6.** The Aluminum oxide - copper oxide phase diagram [18].
- Figure 7.** Wettability map for various liquid metals in contact with $\alpha\text{-Al}_2\text{O}_3$. The temperature for each metal was chosen to be 100°C above the melting point [4].
- Figure 8.** Wettability map for various liquid metals in contact with Quartz. The temperature for each metal was chosen to be 100°C above the melting point [35].
- Figure 9.** Schematic Diagram illustrating the spreading of a liquid drop on a ceramic substrate

• WETTING ($\theta < 90$, $\gamma^{SL} < \gamma^{SV}$)



a)

• NON-WETTING ($\theta > 90$, $\gamma^{SL} > \gamma^{SV}$)



$$\gamma^{LV} \cos \theta = \gamma^{SV} - \gamma^{SL}$$

b)

Figure 1. A schematic illustration of wettability for a liquid metal in contact with a ceramic substrate.

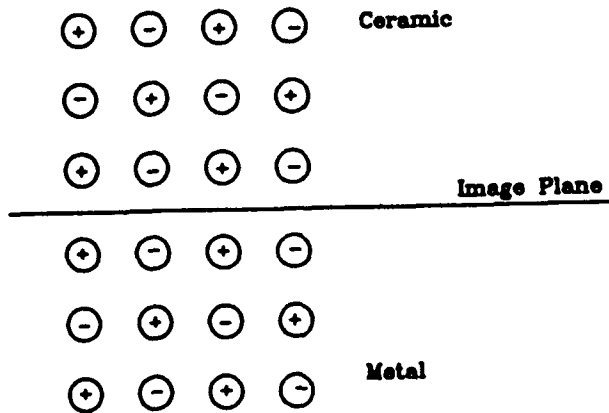


Figure 2. A schematic illustration of the image charges developed at metal-ceramic interfaces [9]

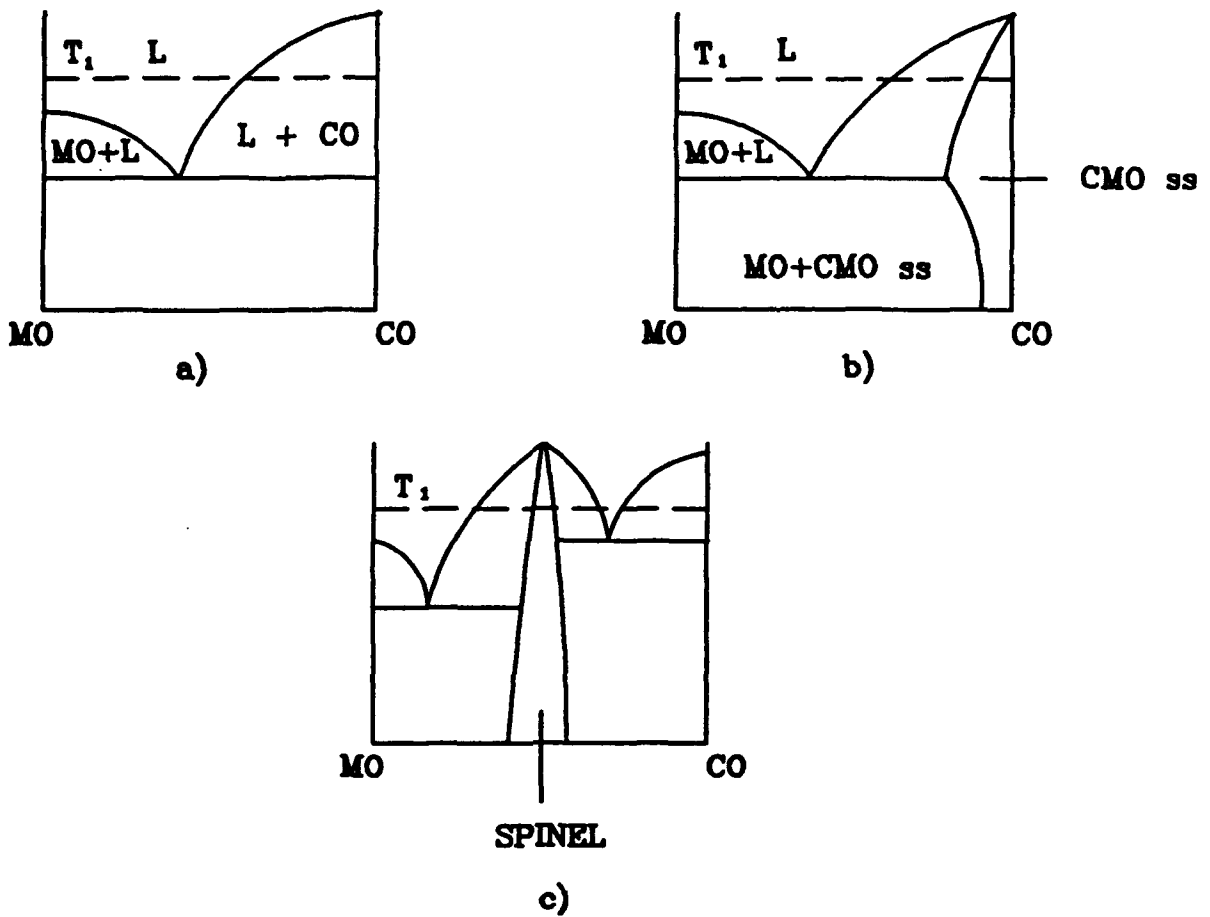


Figure 3. Oxide-oxide phase diagrams showing various types of solubilities

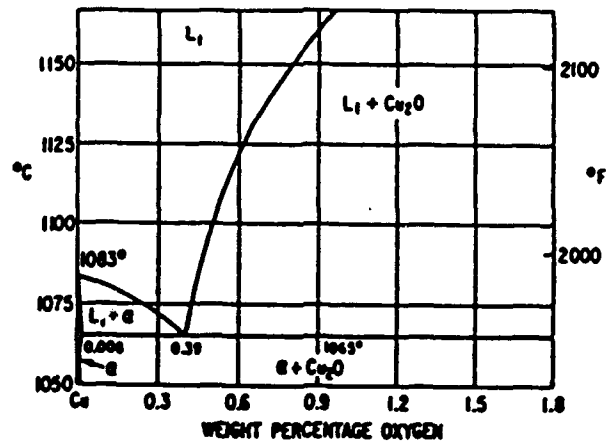


Figure 4. The copper-oxygen phase diagram

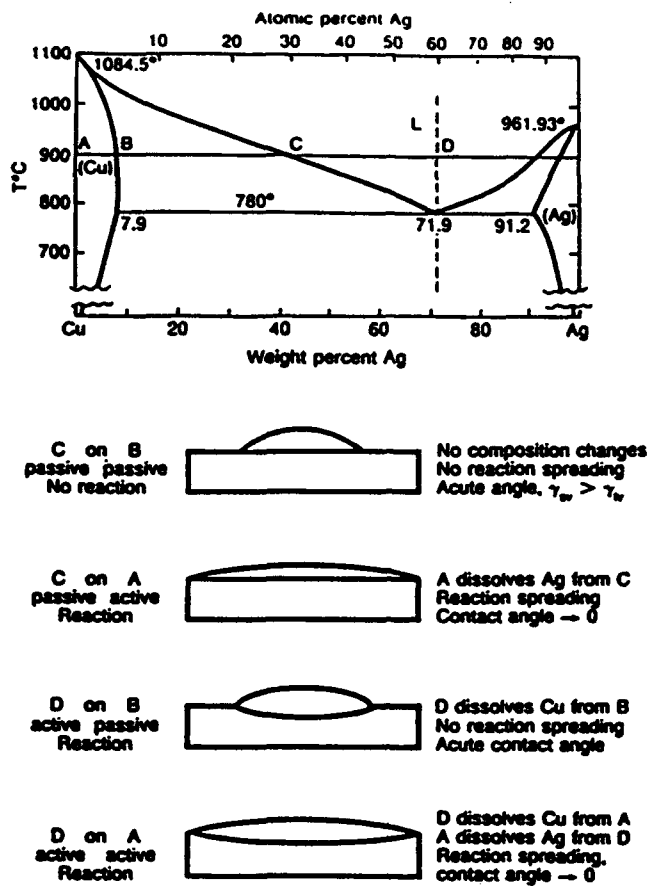


Figure 5. a) The copper-silver phase diagram
 b) The sessile drop morphology for various solid-liquid interfaces [19]

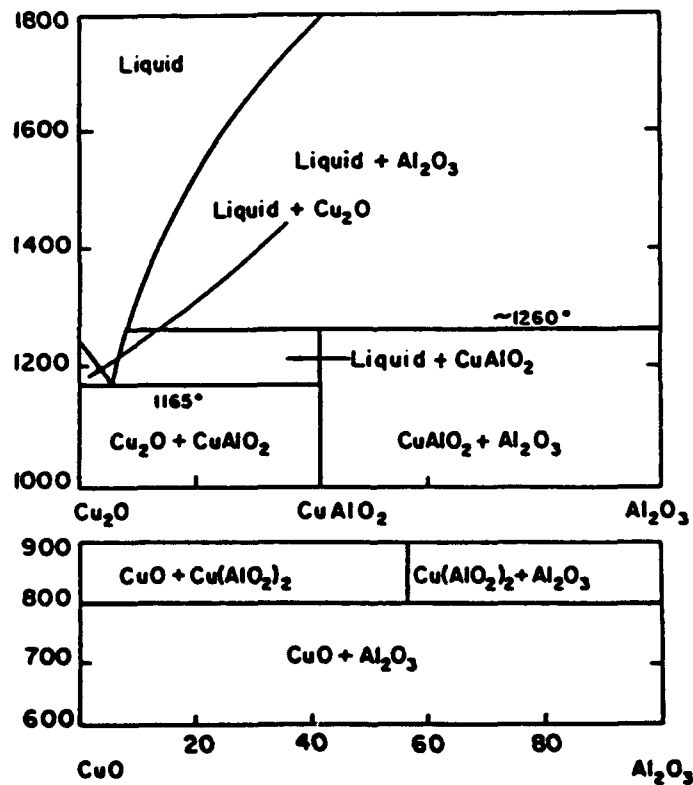


Figure 6. The Aluminum oxide - copper oxide phase diagram [18]

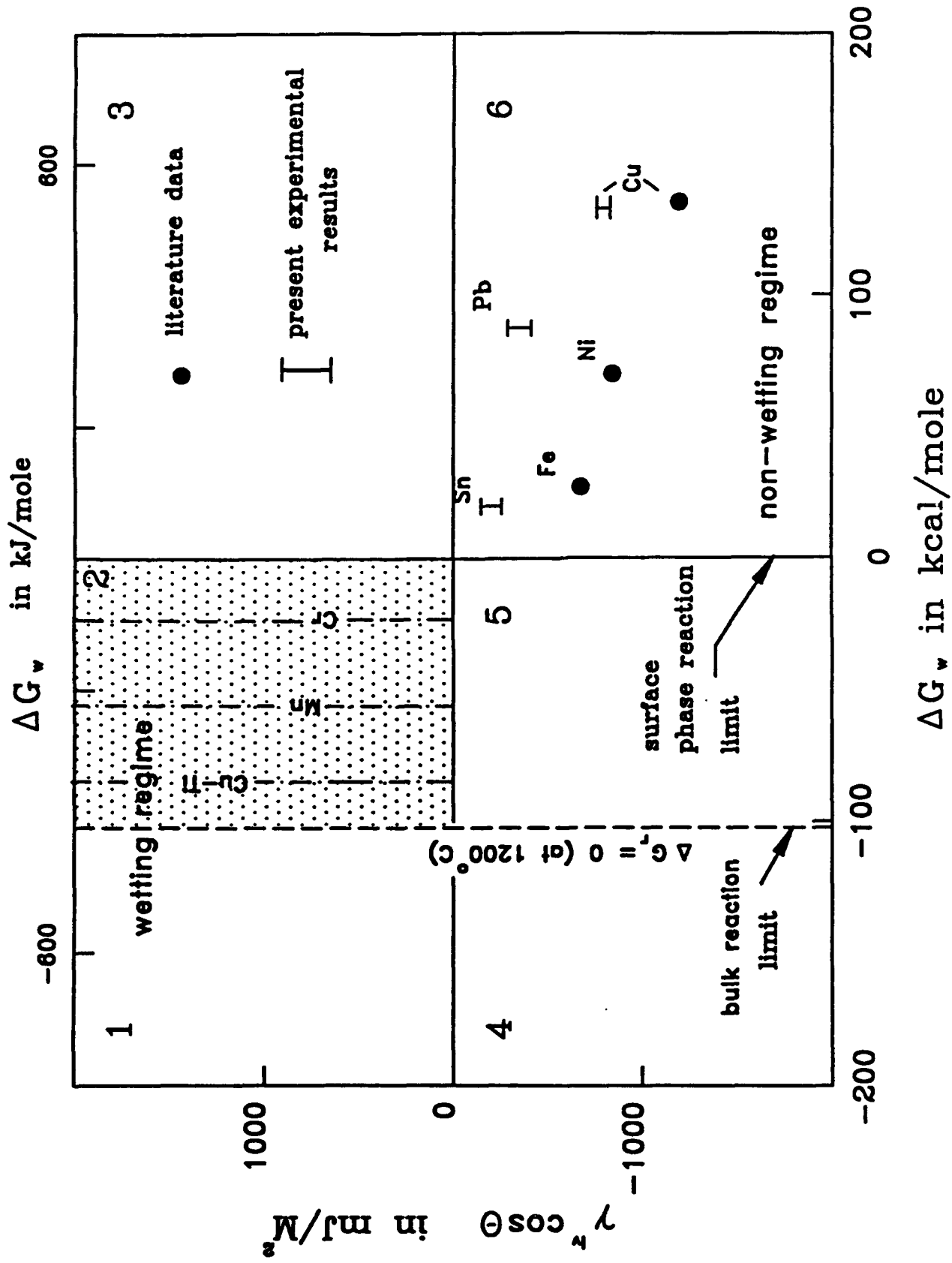


Figure 7. Wettability map for various liquid metals in contact with $\alpha\text{-Al}_2\text{O}_3$. The temperature for each metal was chosen to be 100°C above the melting point [4].

WETTABILITY MAP (SiO₂)

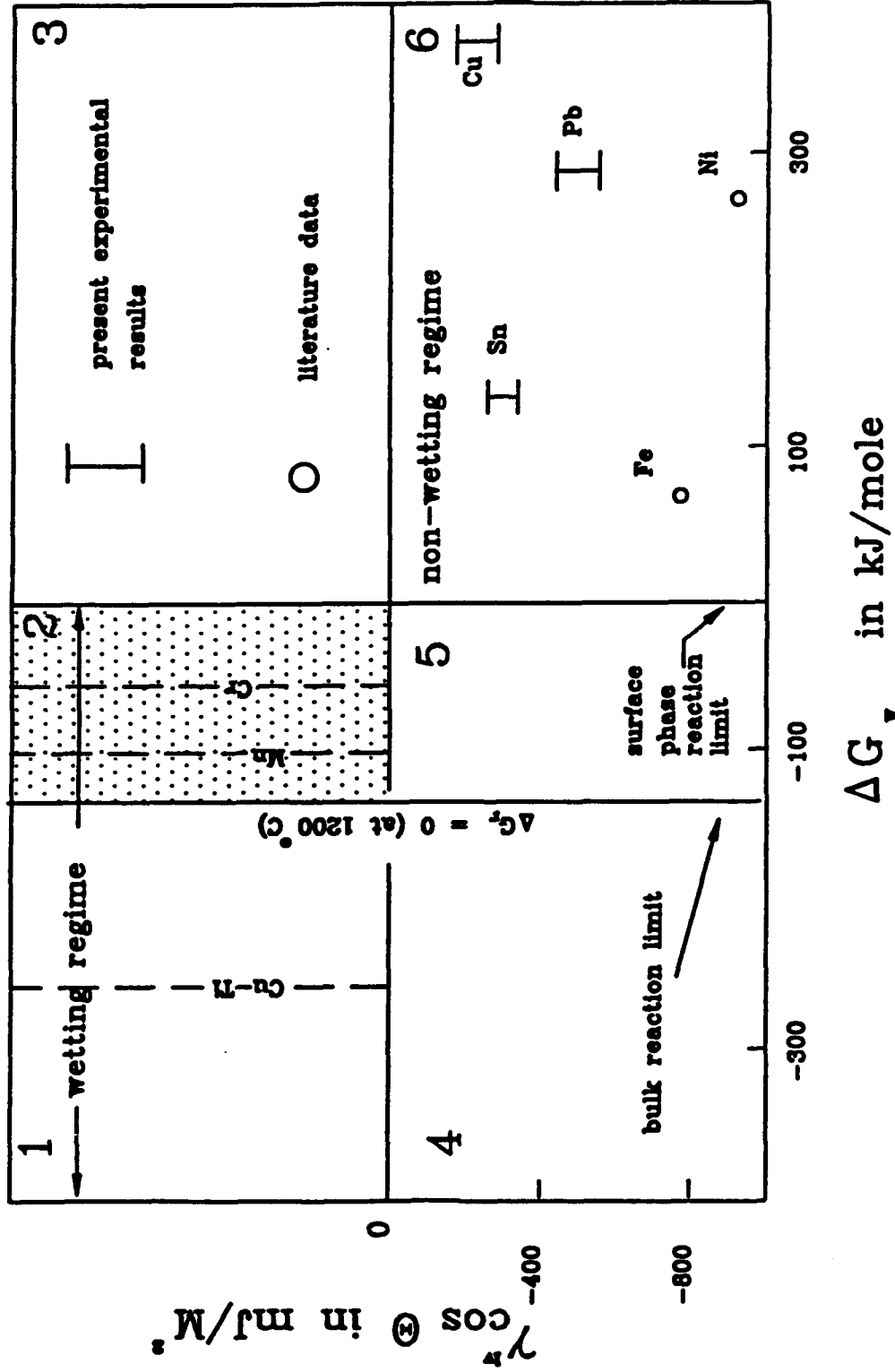


Figure 8. Wettability map for various liquid metals in contact with Quartz. The temperature for each metal was chosen to be 100°C above the melting point [35].

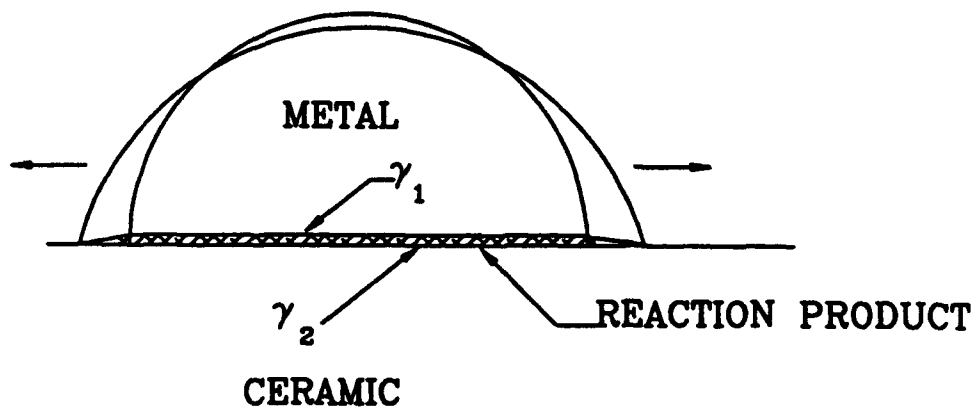


Figure 9. Schematic Diagram illustrating the spreading of a liquid drop on a ceramic substrate

Interfaces

in

Metal-Ceramics Composites

Proceedings of the international conference on Interfaces in Metal-Ceramics Composites, sponsored by the TMS Process Fundamental Committee and Composite Committee and held at the TMS Annual Meeting, February 18-22, 1990 in Anaheim, California.

Edited by

R.Y. Lin

University of Cincinnati
Cincinnati, Ohio

R.J. Arsenault

University of Maryland
College Park, Maryland

G.P. Martins

Colorado School of Mines
Golden, Colorado

S.G. Fishman

Office of Naval Research
Arlington, Virginia

A Publication of

TMS
Metals • Metallurgy • Materials

INFILTRATION MECHANISMS AND KINETICS OF LIQUID ALUMINUM

INFILTRATION OF α -SiC COMPACTS

J.D. Seitz, G.R. Edwards, G.P. Martins, and P.Q. Campbell

**Center for Welding and Joining Research
Colorado School of Mines
Golden, Colorado 80401**

ABSTRACT

Production of discontinuous ceramic-reinforced metal matrix composites by liquid metal infiltration offers major economic advantages over solid-state processing. Nevertheless, there are many inherent problems associated with the technique as related to wettability and liquid-metal flow behavior. To be presented are the results of research conducted to develop a better understanding of the interfacial pre-conditioning reactions in relation to the incubation time prior to the onset of liquid metal infiltration. Analysis of results of experiments has yielded information on the temperature sensitivity and pressure dependence of the incubation time, as well as the temperature sensitivity of the incipient-flow threshold pressure.

**Interfaces in Metal-Ceramics Composites
Edited by R.Y. Lin, R.J. Arsenault,
G.P. Martins and S.G. Fishman
The Minerals, Metals & Materials Society, 1989**

INTRODUCTION

Metal matrix composites are often the leading contenders for advanced technological applications where specific (density normalized) properties are of great importance. Attempts to adopt this material for less critical applications have been frustrating because of the high fabricating costs associated with these materials. Most successful primary fabrication techniques involve some kind of solid state process [1]. The liquid metal processes to date are less successful; however, these processes are significantly more economical. The inherent problems associated with the liquid metal approach are related to the non-wetting nature of ceramic surfaces. Hence, the primary task of fabrication processes adopting this route would be to render the ceramic wettable by the molten metal.

Extending the squeeze casting technique to infiltrate the liquid metal into the porous ceramic is of recent interest [2,3,4]. Infiltration occurs when the applied external pressure overcomes the resisting force due to interfacial free energy. In a previous study, Martins et al. [5] have quantified the physical parameters associated with the fluid-flow behavior of the infiltration process, and have analytically described the rate of infiltration.

A process similar to squeeze casting is a probable route for commercial production of discontinuously reinforced composites. Therefore, a fundamental understanding of the infiltration behavior, and its dependence on process parameters such as temperature and pressure are of considerable importance. There have been many efforts in the past to characterize the infiltration behavior [6,7], yet we are far from a complete understanding of this complex interfacial phenomena.

The present work is an effort to study experimentally the effects of pressure and temperature on the infiltration kinetics of liquid aluminum into SiC porous compacts. Initial experiments [9] established the

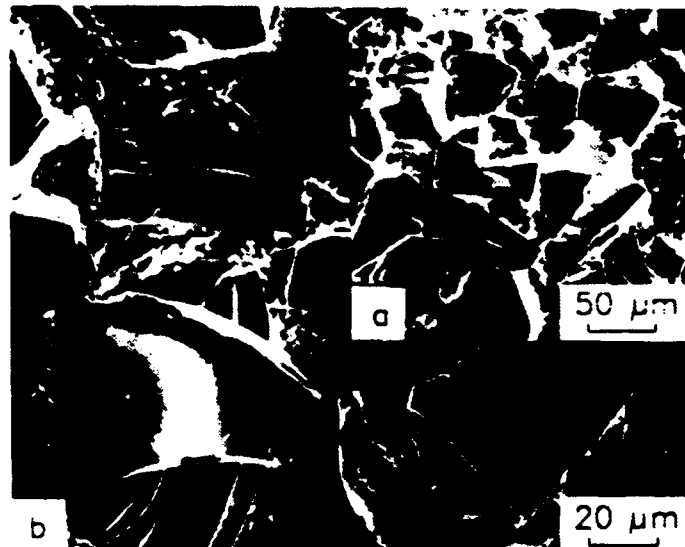
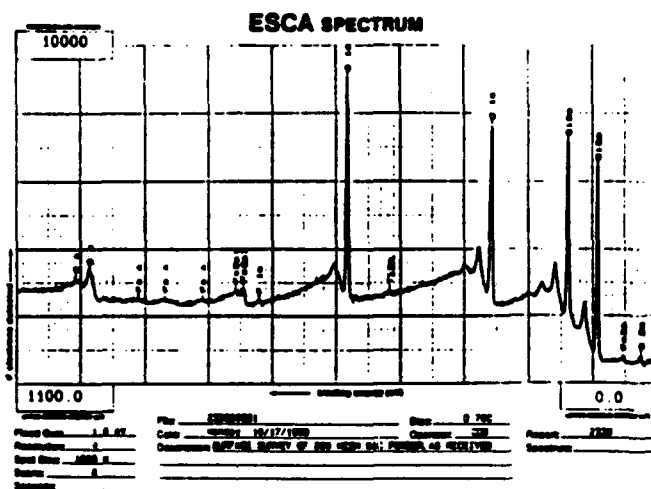


Figure 1. SEM photomicrographs of α -silicon carbide powder (a) X200 and (b) X500.

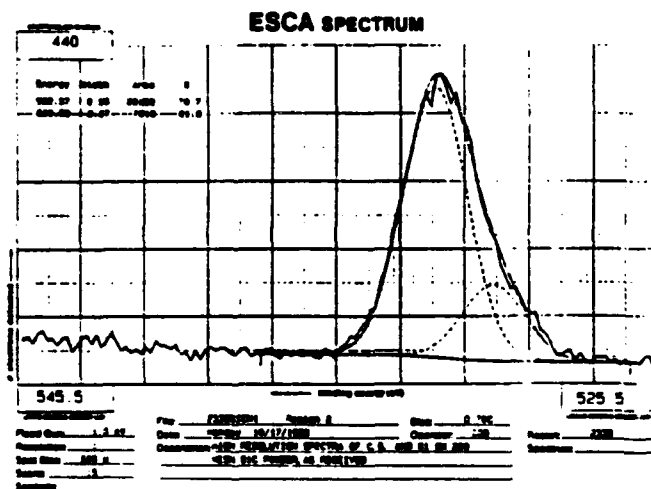
existence of an incubation time before any infiltration could be initiated. A pre-conditioning reaction model was hypothesized to explain the incubation time. A phenomenological rate equation for pre-conditioning was experimentally established, and the threshold pressure -- the minimum pressure required for infiltration after incubation -- was estimated for the system, at several temperatures. The results obtained are discussed in light of the above model and the theoretical development by Martins et al [5].

EXPERIMENTAL PROCEDURE

Infiltration samples were prepared by cold compacting α -SiC particles with a mean diameter of $60 \mu\text{m} \pm 15 \mu\text{m}$, to a void fraction of approximately 0.35. Scanning electron micrographs of the particles are shown in Figure 1. Examination of the surfaces of the SiC particles by x-ray photoelectron spectroscopy (XPS) revealed the presence of oxygen. The XPS spectra of the SiC particles in the as-received condition are shown in Figures 2(a) and 2(b). The surface survey



(a)



(b)

Figure 2. XPS spectra of as-received SiC particles (a) surface survey, (b) deconvoluted O1s spectrum.

indicates the presence of a significant amount of oxygen. A narrow scan of the O1s peak followed by deconvolution of its spectrum uncovered two distinct peaks at binding energies of 530.5 and 532.4 eV. The lower energy peak corresponds to electrons from a SiO₂ suboxide. The presence of either adsorbed oxygen, or water is correlated to the higher energy peak. A one to two monolayer of organic contamination was also detected. This organic contamination together with the adsorbed oxygen species, contributed to a layer not more than 20 Å (0.2 nm).

The compact was formed in a 304 stainless steel tube, approximately 92.0 mm (3.63 in.) long, outer diameter of 19.1 mm (0.75 in.), and inner diameter of 12.7 mm (0.50 in.). The powder was supported by a sintered stainless steel filter (with 15 μm pores) located in its bottom end and was compacted from the top with a slug of aluminum, approximately 6.0 gm, under an applied load of 11.1 kN (2500 lbs). The inner surface of the stainless steel tube was coated with a ceramic adhesive barrier-coating to prevent reaction with aluminum. Argon was supplied to the stainless steel fixture holding the compact, via a 6.4 mm (0.25 in.) stainless steel tube connected to a stainless steel compression fitting (with brass ferrule) attached to the top of the aforementioned fixture.

After the fixture was placed in the cold zone of the furnace chamber, the chamber was purged of oxygen by evacuating and back filling it three times with argon. The fixture was then lowered into the hot zone and allowed to equilibrate for one hour. A schematic of the infiltration chamber is given in Figure 3.

The infiltration process was initiated by closing the bottom inlet valve (argon supply to the chamber) and venting the chamber to atmosphere; thereby creating a pressure difference across the compact. After a specified time had elapsed, the vent was closed and the argon valve was re-opened to equilibrate the system. The fixture was then raised into the

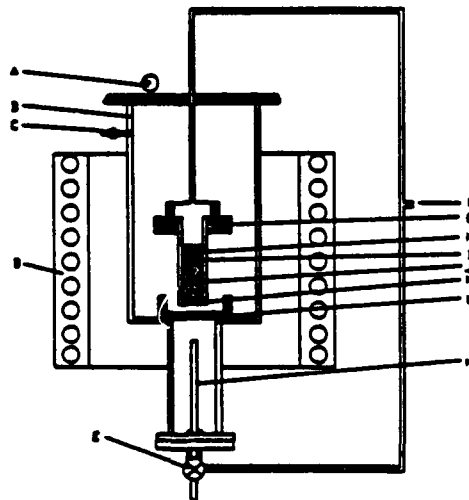


Figure 3. Schematic of the experimental infiltration apparatus: (a) pressure gauge, (b) controlled-atmosphere chamber, (c) vent valve, (d) Marshall furnace, (e) bottom valve, (f) argon supply, (g) compression-seal fittings, (h) stainless steel tube, (i) aluminum slug, (j) silicon carbide compact, (k) porous plug, (l) graphite crucible, and (m) thermocouple.

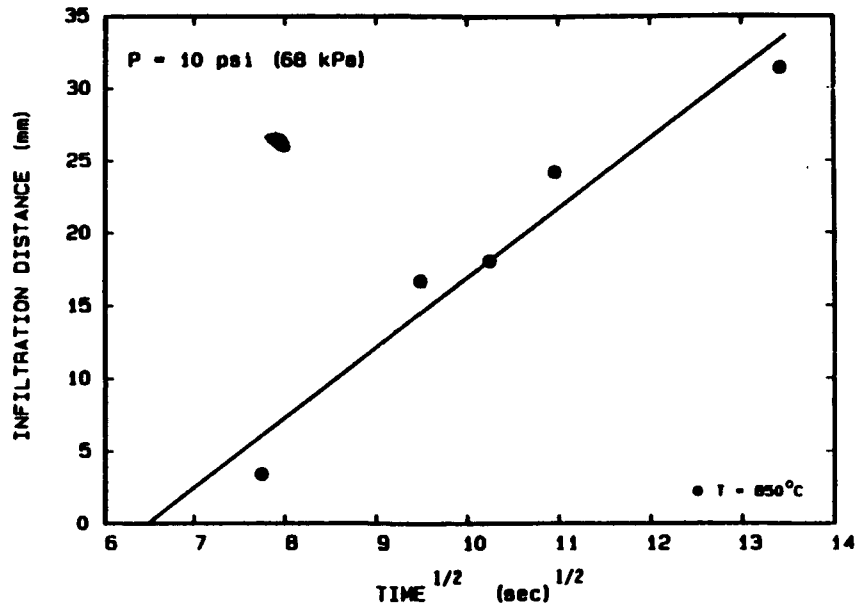


Figure 4. Infiltration distance versus square root of elapsed time for aluminum in silicon carbide at an applied pressure of 10 psi (68 kPa).

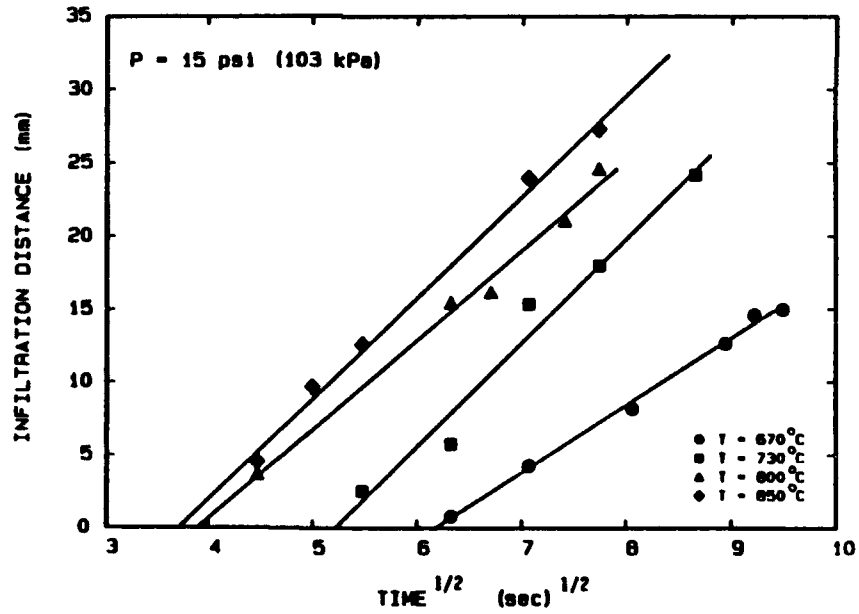


Figure 5. Infiltration distance versus square root of elapsed time for aluminum in silicon carbide at an applied pressure of 15 psi (103 kPa).

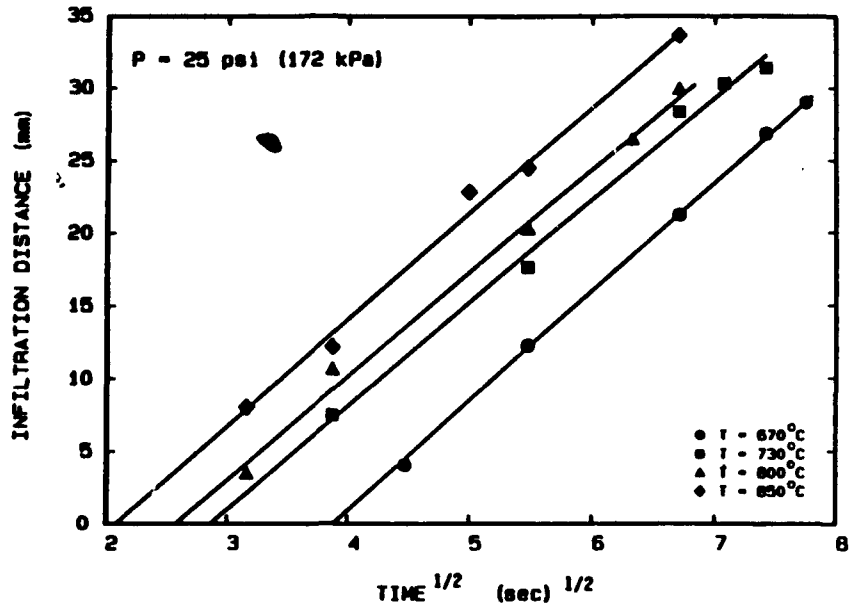


Figure 6. Infiltration distance versus square root of elapsed time for aluminum in silicon carbide at an applied pressure of 25 psi (172 kPa).

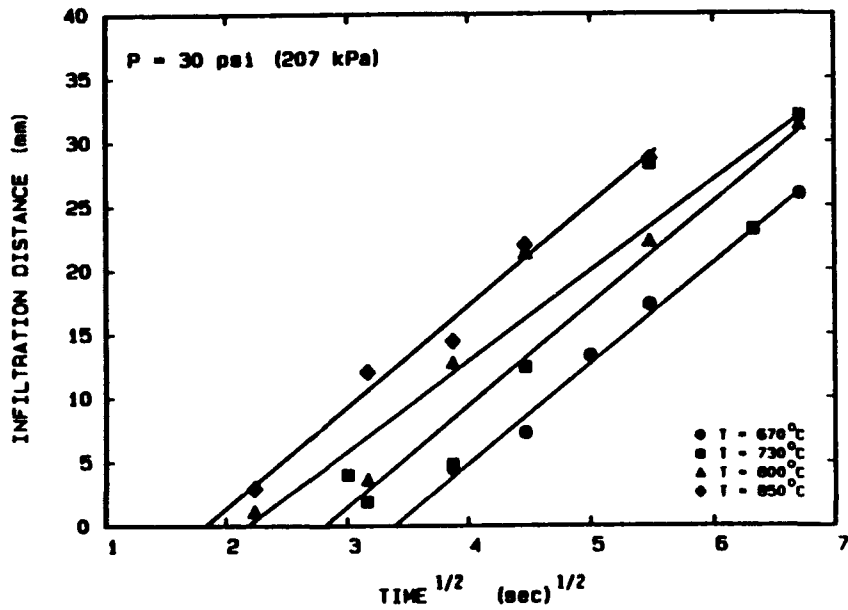


Figure 7. Infiltration distance versus square root of elapsed time for aluminum in silicon carbide at an applied pressure of 30 psi (207 kPa).

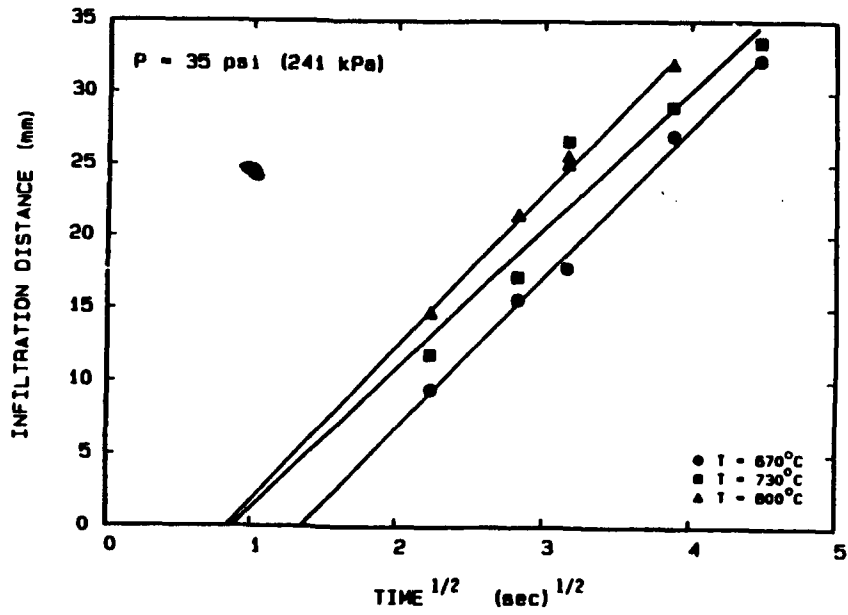


Figure 8. Infiltration distance versus square root of elapsed time for aluminum in silicon carbide at an applied pressure of 35 psi (241 kPa).

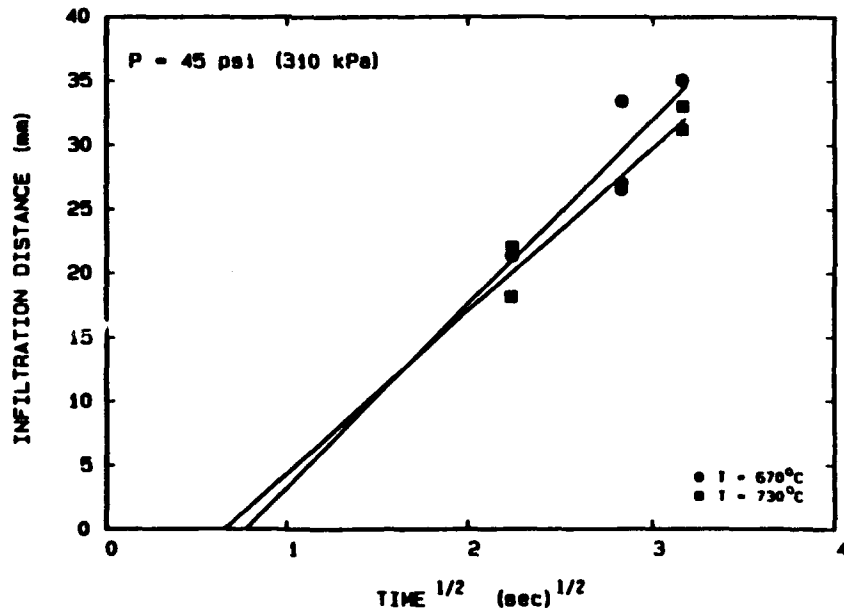


Figure 9. Infiltration distance versus square root of elapsed time for aluminum in silicon carbide at an applied pressure of 45 psi (310 kPa).

cold zone and allowed to cool. The sample was subsequently removed, sectioned longitudinally, and the infiltration distance (the distance to which the liquid metal penetrated the porous compact) was measured.

RESULTS AND DISCUSSION

The results of the study are shown in Figures 4-9, where the infiltration distance as a function of time is presented for different temperatures and pressures. These figures show that the incubation time (minimum time required for the initiation of infiltration) occupied a significant fraction of the overall process time, and thus became the primary focus for the analysis of the data.

Incubation Studies

The incubation time can be estimated from the plotted data shown in Figures 4-9, by extrapolating the line to zero infiltration distance. These incubation times are tabulated in Table I. Inspection of the table clearly shows a significant temperature dependence, with incubation time decreasing as temperature increases. This behavior prior to ingress of liquid metal into the porous compact, can be interpreted as a pre-conditioning reaction, with a thermally activated mechanism.

Table 1. Incubation times for the infiltration of 60 μm diameter α -silicon carbide particles at various pressures and temperatures.

ΔP (psi)	ΔP (kPa)	T ($^{\circ}\text{C}$)	t_0 (sec)
10	< 68 >	850	42.2 + 2.9
15	<103>	670	38.0 + 2.9
		730	27.1 + 1.4
		800	15.4 + 2.0
		850	13.6 + 5.7
25	<172>	670	15.3 + 3.1
		730	8.1 + 1.7
		800	6.6 + 1.3
		850	4.4 + 1.0
30	<207>	670	11.3 + 1.1
		730	7.8 + 0.4
		800	4.6 + 0.4
		850	3.3 + 0.6
35	<241>	670	1.8 + 0.6
		730	0.8 + 0.2
		800	0.7 + 0.5
45	<310>	670	0.6 + 0.2
		730	0.5 + 0.2

On the basis that the pre-conditioning reaction is a first order process, an empirically determined activation energy can be obtained from the data for incubation times. Thus, for isobaric conditions the

following equation may be used:

$$1/t_0 = \alpha [\exp (-Q/RT)] \quad (1)$$

where t_0 is the incubation time, α is the pre-exponential factor, R is the gas constant, T is the absolute temperature, and Q is the thermal activation energy.

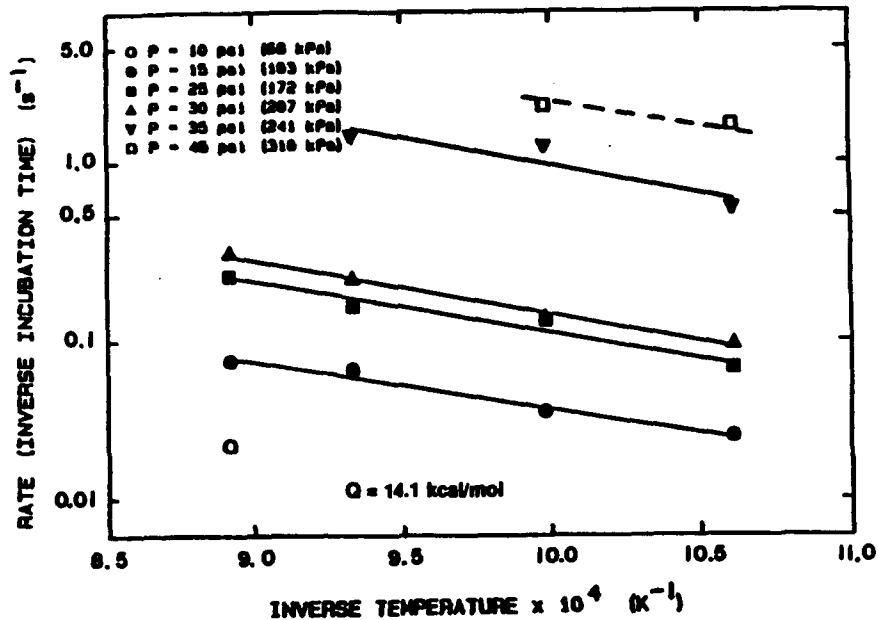


Figure 10. Arrhenius plot -- rate versus inverse temperature for various applied pressures.

If the equation above accurately characterizes the temperature dependence of pre-conditioning, a semi-log plot of pre-conditioning rate ($1/t_0$) versus inverse temperature ($1/T$), under isobaric conditions, should yield a single value of the activation energy, as shown in Figure 10. The activation energy was calculated to be 14.1 kcal/mole. For a given applied pressure difference across the compact, the quantity, α , is temperature independent. Its magnitude at a selected pressure can be used to determine the base-line pre-conditioning rate referenced to a selected temperature (e.g. 670°C).

The rate of pre-conditioning was also found to be sensitive to the pressure of infiltration. This is manifested by the isobaric lines in Figure 10 being displaced from each other. In turn this is reflected by the value of α in the equation for each line having a unique value for each pressure. As the applied pressure was increased, the value of α was found to increase non-linearly as shown in Figure 11. In this plot, α for a given pressure was calculated from equation (1) by substituting the value of t_0 corresponding to the test temperature, and using the average activation energy of 14.1 kcal/mole in the exponential term. Examination of Figure 10 shows that for pressures greater than 207 kPa (30 psig) the pre-exponential factor is significantly increased.

In an attempt to quantify this dependence, the data of Figure 11 were then correlated to an equation of the form:

$$\alpha = \alpha_0 \Delta P^n \quad (2)$$

where ΔP is the applied pressure, n and α_0 are fit parameters used to correlate the pressure dependency. The exponent characterizing the pressure dependence was determined by plotting α versus applied pressure on a decade grid as shown in Figure 12. Two distinct regimes of

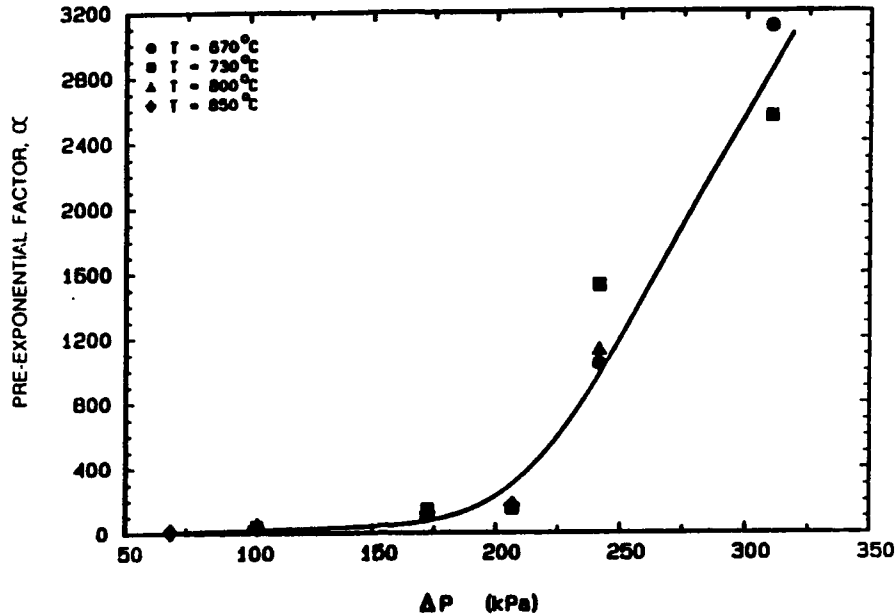


Figure 11. Pre-exponential factor α of equation (1) versus applied pressure plotted on a rectilinear grid.

pressure dependence can be found from this plot. For applied pressures lower than 207 kPa (30 psig) the exponent was calculated to be 2.9. At pressures greater than 207 kPa (30 psig), the exponent was found to be 7.2, indicating a change in mechanism. Corresponding values of α_0 are tabulated under CONCLUSION. Currently, no established theoretical models are available to rationalize the pressure dependence observed in these tests.

In order to develop an understanding of the phenomena related to the incubation time, it is necessary to visualize the physical configuration as the slug of molten aluminum is brought into contact with the face of the compact. It is apparent that the average void fraction/pore size at this face will be discontinuous relative to the bulk of the porous compact. Consequently, the behavior of the primary ingress of liquid metal will be significantly different to that, once the liquid has penetrated past the face, to a distance of approximately one particle (average) diameter. In addition, the liquid interface of the molten aluminum slug can be considered as a membrane whose mechanical properties are governed not only by the surface tension of the liquid but also by an oxide film which is likely to be present. The pressure difference applied across the molten slug of aluminum in conjunction with the overall interfacial properties, will determine the deflection, and hence the radius of curvature of this membrane. This is illustrated for a simple

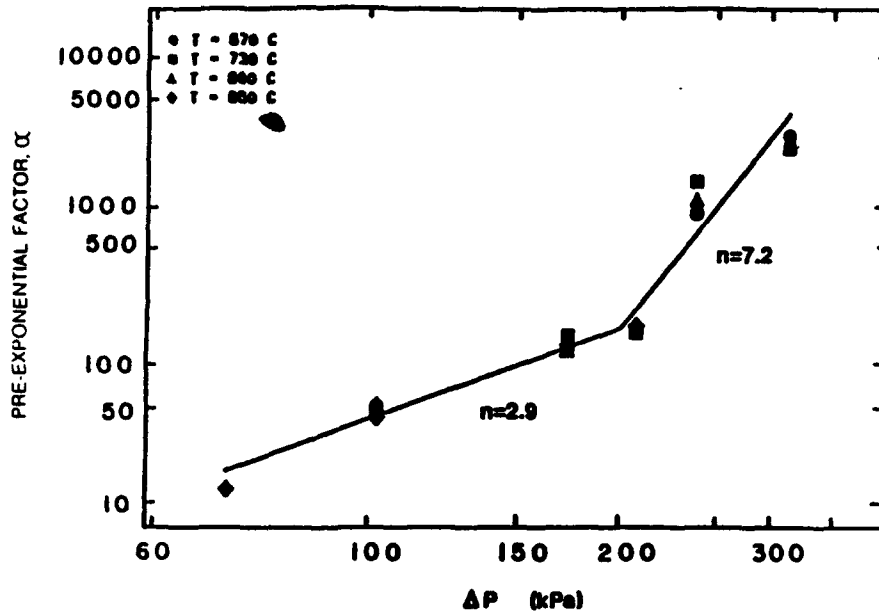


Figure 12. Pre-exponential factor α of equation (1) versus applied pressure plotted on a decade grid.

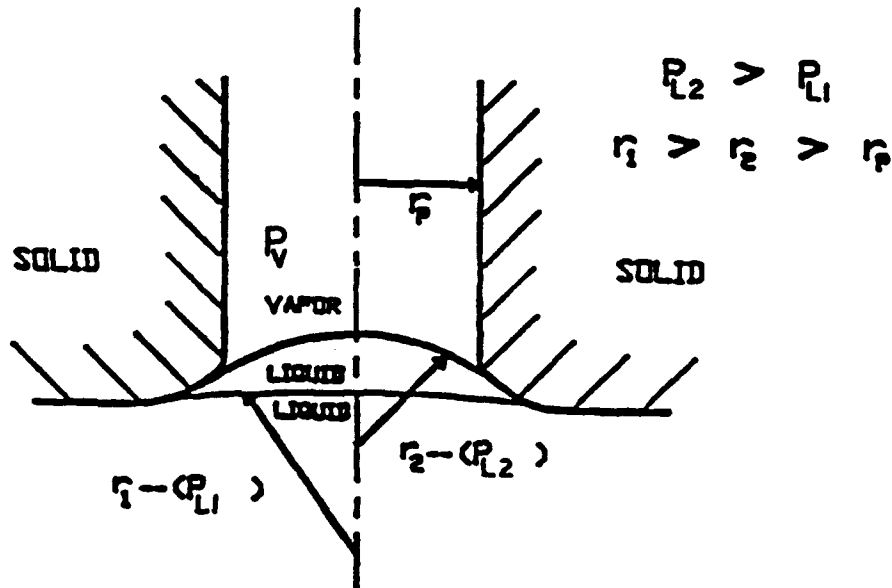


Figure 13. Schematic of primary ingress of liquid aluminum across the face of the SiC compact.

pore, in Figure 13. Thus, for an applied pressure greater than the threshold pressure (see section on infiltration studies) the radius of curvature progressively decreases, as a result of physicochemical changes at the liquid/solid interface, until it is of similar size to the pore radius. The liquid metal can then enter the pore and infiltration of the porous compact commences. The physicochemical changes at the interface include a decrease in the contact angle between the liquid aluminum and solid silicon carbide as a result of oxygen being scavenged from the silicon carbide surface by reaction with aluminum. Also, the mechanical stretching of the "interfacial membrane", which incorporates the aluminum oxide phase, can lead to thinning and, decrease in its stretching resistance; hence, a decrease in its radius of curvature. It is therefore plausible that increasing the applied pressure difference can promote a dual effect, in that it provides for increased oxygen scavenging due to improved contact between liquid aluminum/silicon carbide, as well as the thixotropic dilation of the interface.

Although, the mechanism proposed above can provide a rationale for the observed behavior of the incubation time, development of a rigorous fundamental model which can be used for quantification, is not a trivial task. The effort provided in this work represents an empirical approach to a highly complex process.

Finally, it is worth noting that a reaction mechanism in which aluminum vapor reacted with oxygen on the SiC particles, was also considered. The effect of curvature on the equilibrium vapor pressure above the aluminum was investigated. The enhancement of the vapor pressure above a convex surface of radius r , relative to a flat surface can be described by the Thompson equation:

$$\frac{p(r)}{p(\infty)} = \exp \left(\frac{V_{Al}^1}{RT} \cdot \frac{2\gamma_{LV}}{r} \right) \quad (3)$$

If the following property values (S.I. units) for pure aluminum at 660°C are used:

$$V_{Al}^1 = 1.124 \times 10^{-2} \text{ m}^3/\text{mol}; R = 8.314 \times 10^3 \text{ J}\cdot\text{mol}^{-1}\cdot\text{K}^{-1}$$

and $\gamma_{LV} = 0.915 \text{ kg/s}^2$, there is approximately a 30% increase in vapor pressure for $r = 10 \text{ nm}$ (100Å). The effect is even smaller (25%) at 800°C. This finding, in conjunction with the low vapor pressures of aluminum ($\sim 10^{-12}$ at 660°C and $\sim 10^{-9}$ at 800°C) led to the elimination of this mechanism from further consideration.

Infiltration Studies

The parabolic time dependence of infiltration distance has been addressed theoretically in the work of Martins, et al. [5], and has been verified experimentally, both by Maxwell [9] and by the work included in this paper. This relationship can be expressed as:

$$h = At^{1/2} \quad (4)$$

where h is the infiltration distance, A is the slope of the regressed line from the infiltration distance versus the square root of time plots (Figures 4-9), and t is time measured from the onset of infiltration.

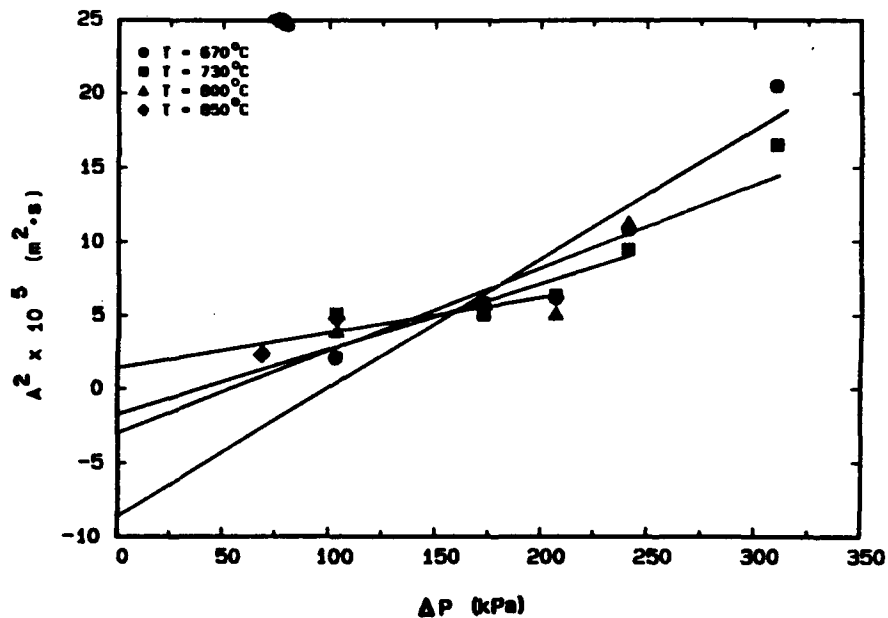


Figure 14. Plot to determine the threshold pressure -- A^2 versus applied pressure.

Theoretical analysis [5] shows that the parameter A in the above equation is given by:

$$A = \left(\frac{2}{K_1 \eta}\right)^{1/2} (\Delta P - P_{th})^{1/2} \quad (5)$$

where K_1 is a constant which can be related to the porosity of the compact and particle diameter [9], η is the viscosity of the liquid aluminum, ΔP is the applied pressure difference (gauge pressure), and P_{th} is the threshold pressure. The threshold pressure is defined here to be that dynamic value of applied pressure required to overcome the wetting resistance (surface tension force) and the fluid static head after infiltration has begun, and is not to be confused with the upper limit of pressure, above which, the incubation time is so small it cannot be discriminated (<100 milliseconds in this work). From a theoretical analysis it can be shown that:

$$P_{th} = \frac{2\gamma_{LV} \cos\theta}{r} \quad (6)$$

where γ_{LV} is the surface tension of the liquid metal, θ is the contact angle between the metal and the solid particles and r is the characteristic pore size of the compact.

Equation (4) can be used to estimate the threshold pressures for the tests conducted. The values of A taken from the slope of the lines in Figures 4-9 as described above, were squared and plotted against the

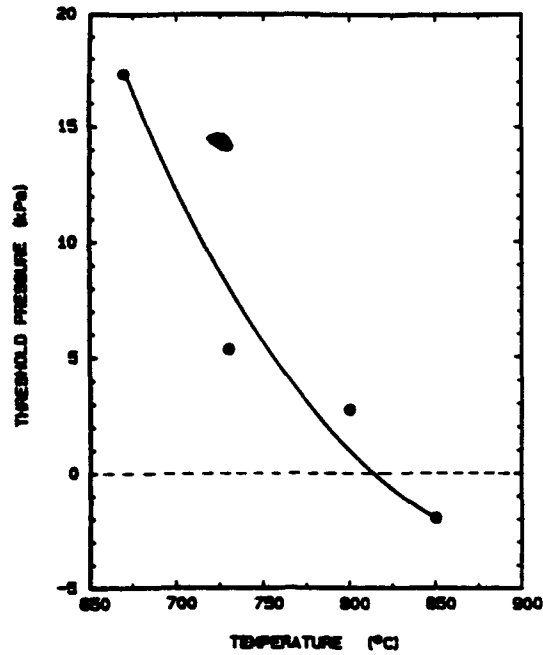


Figure 15. Threshold pressure versus temperature for the aluminum/silicon carbide system.

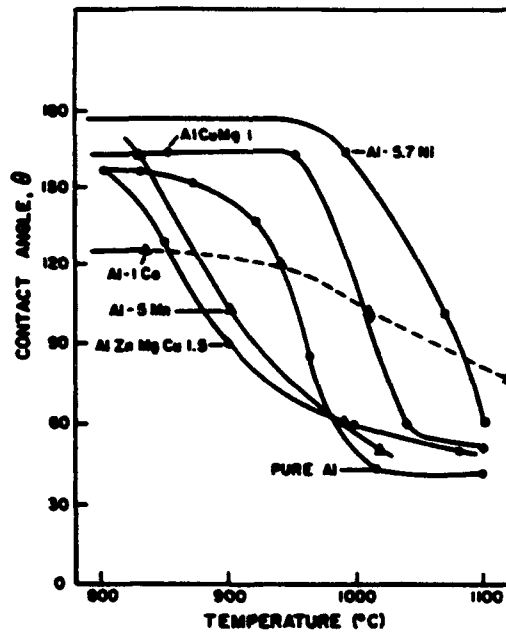


Figure 16. Contact angles for various aluminum alloys in contact with silicon carbide, as reported by Kohler (11). For pure aluminum, wetting occurs at approximately 960°C.

applied pressure as shown in Figure 14. It is noted that Oh, et al. [4] found that for a SiC compact consisting of 10 μm particles the threshold pressure (difference) required for infiltration with 2% magnesium-aluminum alloy at 800°C was 565 kPa, compared to 3 kPa obtained in this work where the particle size was 50 μm . If the relative size of the hydraulic-mean pore radius for the two cases is estimated [9], the pore radius for the smaller size particle is approximately 100 times smaller. Recognizing that the threshold pressure is inversely proportional to the pore radius, there is good agreement between these two pressures; notwithstanding that referenced work was for a 2% Mg-Al alloy. Using the slopes and intercepts from the lines in the plot, the threshold pressures for the temperatures shown were calculated, in accordance with equation (5). The temperature dependence of the threshold pressure is shown in Figure 15. The negative threshold pressure determined for the test temperature of 850°C implies that the system is wetting and infiltration should occur spontaneously. This observation is in contradiction with the data from Kohler [10] presented in Figure 16, which indicates that pure liquid aluminum does not wet (contact angle $<90^\circ$) SiC until the temperature is above approximately 960°C. The discrepancy points out the complexity of quantifying the wetting tendency of metal-ceramic couples, and indicates the sensitivity of wetting to the exact chemical nature of the liquid aluminum interface and the SiC substrate.

CONCLUSION

The results of this study can be summarized as follows:

1. The incubation process for infiltration of silicon carbide particles with aluminum obeys the phenomenological equation:

$$\text{Rate} = \alpha_0 \Delta P^n [\exp(-Q/RT)]$$

$$\text{where: } n = 2.9 \begin{cases} 69 \text{ kPa} \leq \Delta P \leq 207 \text{ kPa} \\ 10 \text{ psi} \leq \Delta P \leq 30 \text{ psi} \end{cases}$$

$$\alpha_0 = 5.43 \times 10^{-15} \text{ (when } \Delta P \text{ and Rate have units of kPa and } s^{-1} \text{ respectively)}$$

$$n = 7.2 \begin{cases} 207 \text{ kPa} \leq \Delta P \leq 310 \text{ kPa} \\ 30 \text{ psi} \leq \Delta P \leq 45 \text{ psi} \end{cases}$$

$$\alpha_0 = 4.79 \times 10^{-15} \text{ (when } \Delta P \text{ and Rate have units of kPa and } s^{-1} \text{ respectively)}$$

$$Q = 14.1 \text{ kcal/mole; } 943^\circ\text{K} \geq T \geq 1123^\circ\text{K}$$

2. The observations which characterize the incubation phenomenon can be rationalized on the basis of i) discontinuity of the void fraction/pore size properties at the face of the compact relative to its bulk, ii) improved oxygen scavenging of the silicon carbide surface by aluminum due to increased pressure in the liquid, and iii) thixotropic dilation of the "interfacial membrane".
3. The temperature dependency of the threshold pressure for infiltration of silicon carbide compacts (60 μm particles) with aluminum is such that it varies from 17.3 kPa at 670°C to less than zero (a wetting system) at 850°C.

ACKNOWLEDGEMENTS

This research was supported by the Strategic Defense Initiative Office/Innovative Science and Technology under ONR Contract Number N00014-88-K-0500. The encouragement of Dr. Steven Fishman is gratefully acknowledged.

REFERENCES

1. I.J. Toth, W.D. Brantnall, and G.D. Menke, "Fabricating Aluminum Matrix Composites", J. Metals, vol. 24, pp. 19 (1972).
2. K. Ohori, H. Watanabe, and Y. Takeuchi, "Silicon Carbide Whisker Reinforced Aluminum Composites -- Fabrication and Properties", Material Sci. and Tech., vol. 3, pp. 57 (1987).
3. S.K. Verma and J.L. Doraic, "Squeeze Casting Process for Metal-Ceramic Composites", SAE Technical Paper #870405 (1987).
4. S.Y. Oh, J.A. Cornie, and K.C. Russell, "Wetting of Ceramic Particulates with Liquid Aluminum Alloys: Part 1. Experimental Techniques", Met. Trans. A, vol. 20A, pp. 527 (1989).
5. G.P. Martins, D.L. Olson, and G.R. Edwards, "Modeling of Infiltration Kinetics for Liquid Metal Processing of Composites", Met. Trans. B, vol. 19B, pp. 95 (1988).
6. F.M. Hosking and A.A. Netz, "Liquid Metal Infiltration of an Aluminum Alloy into a Packed Column of B₄C Particles", Research Report, Sandia National Laboratory (1984).
7. T.W. Clyne, M.G. Bader, G.R. Cappleman, and P.A. Hubert, "The Use of δ -Alumina Fibre for Metal Matrix Composites", J. Material Sci., vol. 20, p. 85 (1985).
8. P.B. Maxwell, "The Infiltration Behavior of Aluminum into Silicon Carbide Compacts", CSM Thesis No. T-3396, Colorado School of Mines, April, 1987.
9. J.D. Seitz, "The Infiltration Kinetics of Silicon Carbide Reinforced Aluminum Matrix Composites", CSM Thesis No. T-3614, Colorado School of Mines, December, 1988.
10. W. Kohler, "Examination of the Bonding of Al₂O₃- and SiC-Crystals with Aluminum and Aluminum Alloys", Aluminium, 51, pp. 443-447 (1975).

REPRINT

**SYMPOSIUM ON
JOINING OF MATERIALS
FOR 2000 AD**

**TIRUCHIRAPALLI, INDIA
12 - 14 DECEMBER 1991**

**INDIAN INSTITUTE OF WELDING
TIRUCHIRAPALLI**



FUNDAMENTAL ASPECTS OF METAL-QUARTZ JOINING

PR. Chidambaram, G.R.Edwards and D.L.Olson.

Colorado School of Mines, Golden, CO 80401, USA.

ABSTRACT: Stable interface formation at the metal-ceramic interface requires the formation of irreversible chemical bonds. A surface thermodynamic model is used to predict wettability and stable interface formation between the metal and silicon dioxide surface. Model predictions are verified by experimental capillary rise measurements and chemical analysis.

1 INTRODUCTION

Silicon dioxide or quartz is a material of significant technological interest, especially for use in electronic devices. Also, silicon-containing structural ceramics are usually covered by a layer of silica. In most applications quartz is used in conjunction with a metal. Therefore, forming a stable interface between the metal and the ceramic is critical in developing a joining process. Wetting of the silicon dioxide surface by the metal is a prerequisite to joining.

It has been known that in metal-ceramic systems a chemical bond is essential for any stable interface formation. Using this principle in an earlier study resulted in a thermodynamic criterion to identify the metals that wet an aluminum oxide surface [1]. A similar approach is used here to predict wettability on silicon dioxide surfaces. Wetting is treated as a surface phenomenon, and a surface reaction monolayer is considered sufficient to cause wetting. The theoretical predictions are verified experimentally using a capillary rise apparatus. The wettability parameter, $\gamma^{lv}\cos\theta$ in the Young equation:

$$\gamma^{lv}\cos\theta = \gamma^{sv} - \gamma^{sl} \quad (1)$$

(where: γ^{lv} , γ^{sv} , and γ^{sl} are the liquid-vapor, solid-vapor, and liquid-solid interfacial energies respectively), is used as the verification parameter to compare the theory and the experiment. This approach is valid only for non-wetting systems. In wetting systems, the interfacial reaction results in an altogether new phase. A new interface is interposed between the metal and the ceramic, and therefore the Young equation is no longer valid.

THEORY

Sangiorgi et. al. [2] have attempted to model the wetting behavior of various liquid metals on a silicon dioxide surface. Their study resulted in an empirical correlation between the free energy of oxide formation and the non-wetting contact angles between noble metals and a quartz surface.

The uniqueness of the theory presented here is its ability to delineate the wetting and non-wetting systems. Wetting can be defined to occur between a solid and a liquid when the liquid atoms establish atomic contact with the atoms on the surface of the solid. A force of attraction is essential for the purpose; this force of adhesion can be physical or chemical in nature. In the case of a metal-ceramic interface, the physical force is very weak. All commercially known metal-ceramic components rely on a chemical bond for interface formation. A simple analytical approach to predict wetting, therefore, would be to use the free energy of a reaction, ΔG_r , between the metal and the ceramic as shown in Eqn. (2)



A negative ΔG_r implies a wetting system. It has been previously demonstrated that a bulk thermodynamic approach does not accurately identify the metals that can wet a given ceramic [1]. Therefore, a surface wetting model is used. The surface of quartz can be treated as a separate phase with unique thermodynamic quantities associated with it. A surface phase formation energy, ΔG^{surf} , that is very similar

to the bulk formation, ΔG° can be defined. The atoms on the surface are at a higher energy than the bulk; this energy can be represented in terms of Gibbs excess energy, G^{xs} . Therefore,

$$\Delta G_{SiO_2}^{surf} = \Delta G_{SiO_2}^\circ + G^{xs} \quad (3)$$

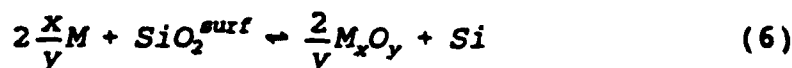
The procedure established to estimate G^{xs} involves the use of the experimentally estimated surface specific energy γ as indicated in Eqn. (4):

$$G^{xs} = \gamma A \quad (4)$$

where A is the area of a mole of surface atoms. Standard procedures are available to calculate this area [3]. Surface specific energy at the temperature of interest can be calculated using Eqn (5):

$$\gamma = \gamma^\circ - \Delta S^s \Delta T \quad (5)$$

There are no standardized procedures for estimating the surface energy; but a few published results are available. γ° , surface specific energy at 0° K; and S^s , surface specific entropy in the present study were estimated to be 830 mJ/M² and 0.26 mJ/M²K respectively from the data published by Kingery [4] and Bruce [5]. Once ΔG^{surf} is calculated, the standard thermodynamic procedure can be used to evaluate the driving force for wetting in terms of the Gibbs free energy of wetting, ΔG_w . A reaction between the metal M of interest and the surface phase of SiO_2 to form M_xO_y can be written as:



and the ΔG_w for this reaction is given by:

$$\Delta G_w \rightarrow \frac{2}{y} \Delta G_{M_xO_y} - \Delta G_{SiO_2}^{surf} = RT \ln \left[\frac{a_{Si}}{a_M^{2x/y}} \right] \quad (7)$$

The free energy of wetting is related to ΔG_w by Eqn (8):

$$\Delta G_w = \Delta G_r + G^{xs} \quad (8)$$

The activity of silicon in the metal a_{Si} is calculated by:

$$a_{Si} = \Gamma_{Si} X_{Si} \quad (9)$$

Activity coefficients, Γ , were obtained from the data book on thermodynamic properties of binary alloys [6]; if unavailable, an ideal behavior is assumed. The standard free energy of formation ΔG° is readily available in the literature [7]. Calculations were performed based on a 100 degree superheat over the melting temperature of the metal, and for one percent dissolution of silicon in the metal. The parameters used and the results obtained from the calculations are presented in Table 1.

EXPERIMENTAL PROCEDURE

The details of the experimental procedure are discussed in Reference 1. Briefly, the principle of capillary rise involves submerging a ceramic tube of appropriate inside diameter in a molten metal of interest and measuring the liquid levels inside and outside the tube. The difference in the two heights, h , is related to the wettability parameter, $\gamma^{lv} \cos\theta$ term by the Young-Laplace equation:

$$\gamma^{lv} \cos\theta = \frac{h\rho gr}{2} \quad (10)$$

Where, ρ is the density of the metal, g is the acceleration due to gravity, and r is the radius of the capillary tube. This approach and the Young-Laplace equation are valid only for non-wetting systems. Therefore, in wetting systems, only a qualitative verification is possible; the degree of wetting could not be ascertained. Strips of quartz were submerged in the metal/alloy and inspected for wetting under the optical and scanning electron microscopes. The energy dispersive X-ray attachment to the scanning microscope was used for chemical analysis.

RESULTS AND DISCUSSION

A positive ΔG_w was obtained for copper, iron, lead, nickel and lead, whereas, a negative free energy of wetting was obtained for copper-titanium, copper-manganese and chromium.

These observations are consistent with the experimental results obtained in the present study, and with previously published results [8]. Reproducible contact angles values were measured using the capillary rise apparatus. The wettability parameters measured for non-wetting systems (copper, tin and lead) as a function of temperature are shown in Figure 1. The wettability parameter was found to decrease with increasing temperature. Copper-titanium and copper-manganese alloys were found to wet quartz surface. The presence of titanium and manganese were confirmed by composition analysis using the energy dispersive X-ray analysis.

A wettability map (a plot of the predicted ΔG_w against the measured $\gamma^{lv}\cos\theta$) was drawn to verify the surface wetting model predictions (Figure 2). The results from this study are shown with error bars; also, the literature values are shown superimposed in the plot. The wetting and non-wetting regimes shown in the plot correspond to a negative and positive free energy of wetting respectively. Non-reactive metals such as copper, tin, nickel, iron and lead fall in the non-wetting regime (region 6). Manganese, chromium and titanium and their respective alloys fall in the wetting category. As mentioned before, $\gamma^{lv}\cos\theta$ term is meaningless for wetting systems. Therefore, the data points in the wetting regime are shown as vertical lines corresponding to the appropriate ΔG_w values. The Region 3 and region 4 are physically meaningless regimes, the absence of any data points in those regimes corroborates the model.

The uniqueness of this approach is its ability to accurately predict a wetting behavior for manganese and chromium (region 2). The wetting regime also encompasses a bulk reaction regime (region 1). A solid line is drawn where ΔG_w is zero. A chemical reaction can occur at any point to the left of this line. (Note that ΔG_w predicts that a reaction between manganese or chromium and quartz is unfavorable.) Titanium falls in the bulk reaction region. After wetting, a reaction between the bulk phase of quartz and titanium is

limited only by the kinetics of the interface formation. With sufficient mass transport, a large interfacial reaction zone will be formed. The interfacial reaction products are typically brittle, and have a deleterious effect on many applications of the metal ceramic component. The difference between ΔG_i and ΔG_v is the surface excess energy G^* (Eqn. 8) which is a function of temperature. Manganese and chromium fall within region 2, where the metal exhibits sufficient thermodynamic activity to reduce the surface of the ceramic but not the bulk. This situation, shown shadowed in Figure 2, results in a stable interface between the metal and the ceramic. The metal reduces the surface atoms of the ceramic; once the surface atoms are depleted, an equilibrium interface is formed. Such interfaces provide the required atomic contact without generating large interfacial reaction products.

CONCLUSIONS

The thermodynamic criterion; i.e., wetting occurs whenever ΔG_i is negative, was found to be true for quartz-metal interfaces. Also, the surface wetting model was found to predict accurately the metals or alloys that form stable interfaces with quartz. Copper-titanium alloys in contact with quartz form an unstable interface with a large interfacial zone, in contrast, copper-manganese alloys form a stable interface. The capillary rise technique can be successfully used to experimentally measure contact angles in non-wetting metal-ceramic systems.

REFERENCE

- 1) P. R. Chidambaram, G. R. Edwards, D. L. Olson, accepted for publication in Met. Trans. B.
- 2) R. Sangiorgi, M. L. Muolo, D. Chatain and N. Eustathopoulos, J. Am. Ceram. Soc., Vol 71 [9], (1988), p. 742
- 3) K. S. Yeum, R. Speiser, and D. R. Poirier, Met. Trans. B, vol. 20 (1989), p. 693
- 4) W. D. Kingery, H. K. Bowen, and D. R. Ulman, Introduction to Ceramics, second. ed., John Wiley, New York, (1976), p. 189

- 5) R. H. Bruce, in Science of Ceramics, vol. 2, G. H. Stewart, editor, Academic Press, London, (1965), pp. 359
- 6) R. Hultgren, P. D. Desai, D. T. Hawkins, M. Gleiser: Selected Values of Thermodynamic Properties of Binary Alloys, ASM, Metals Park, Oh. USA, (1973), pp. 125-804
- 7) JANAF Thermochemical Tables, 2nd edition, U. S. Dept. of Commerce, (1977), p. 20-257
- 8) G. V. Samsonov, The Oxide Handbook, transl. by R. K. Johnston, (1982), Plenum Press, New York, pp. 400-408

ACKNOWLEDGEMENTS : This research was supported both by the Strategic Defence Initiative/Innovative Science and Technology under ONR contract #N00014-88-K-0500 and by the Welding Research Council. The encouragement of Dr. Steven Fishman is gratefully acknowledged.

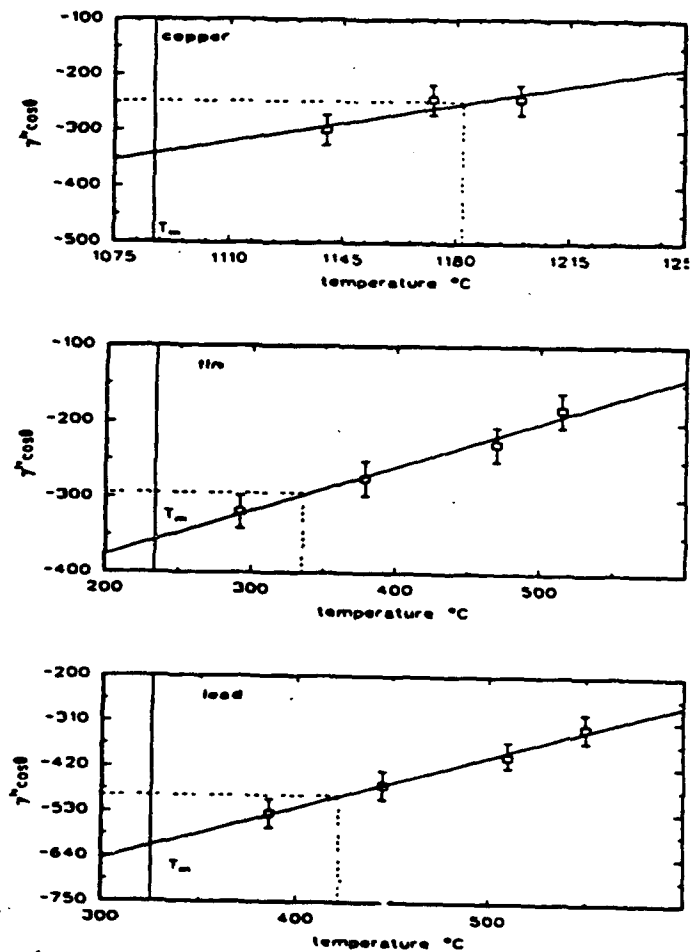


Figure 1. Experimental wettability parameters for copper, tin and lead in contact with α -quartz at various temperatures.

Table I. Model Parameters and Wettability Predictions for an α -quartz Surface'

Metal Alloy	T °K	ΔG° kj/mole	Γ_{sl}	γ^{lv} mj/m ²	ΔG_v kj/mole	$\gamma^{lv} \cos \theta$ mj/m ² (ref)
Cu	1450	-28.1	0.016	1300	370.08	-251 (*)
Ni	1826	-76.5	0.01	1660	267.08	-952.1 (8)
Fe	1909	-142.3	0.003	1840	67.74	-777.6 (8)
Sn	605	-227.5	1	542	141.60	-290 (*)
Pb	700	-148.7	0.15	442	286.80	-480 (*)
Cu-5%Ti	1450	-290	0.016	1300	-256.6	- (*)
Cr	2225	-630.1	1	1590	-51.37	-
Mn	1615	-268.3	1	1060	-108.2	- (*)

- calculations were performed for a 100 degree superheat over the melting temperature.

* - present experimental results

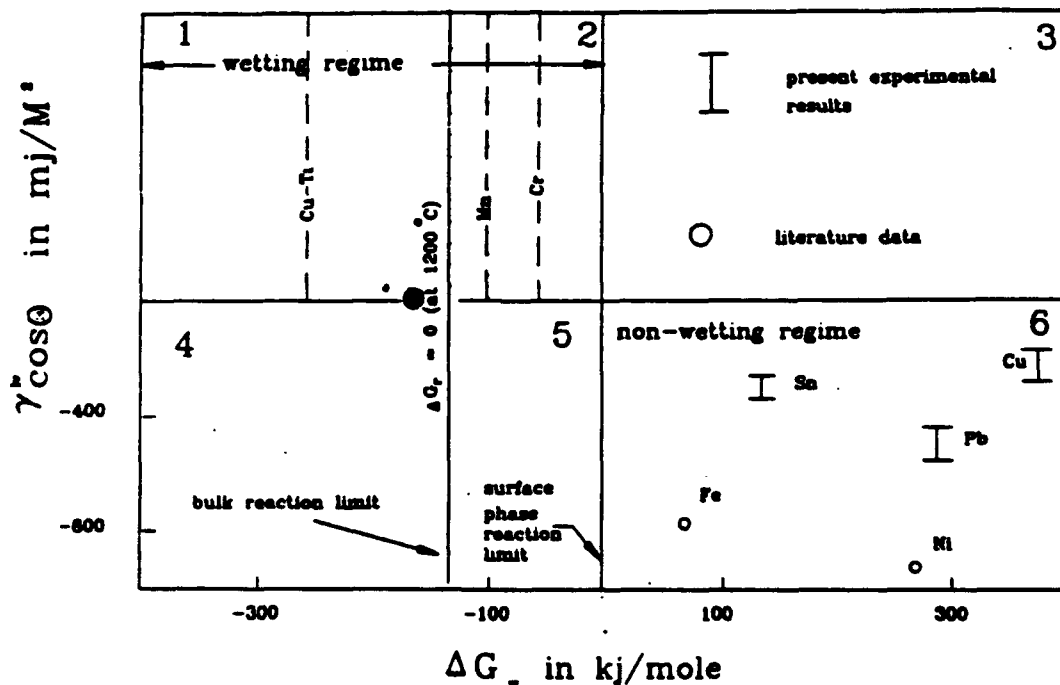


Figure 2. Wettability map for quartz. Temperature was chosen to be 100 degrees Kelvin above the melting temperature of the metal or alloy.